# Novel Synthesis of Heterogeneous Catalysts for the Complete Combustion of Dual-Fuel Vehicular Gases Carbon Monoxide and Methane

**Dave Shaw**

**PhD Thesis**

Supervisory Team: Dr Aidan Doyle, Dr Lubomira Tosheva, Prof Craig Banks

A transfer report submitted in partial fulfilment of the requirements
of the Manchester Metropolitan University for the degree of Doctor of Philosophy

School of Science and the Environment

Department of Natural Sciences

Manchester Metropolitan University

September 2019

# Contents

| Abbreviation | Explanation |
|---|---|
| **CNG** | Compressed natural gas |
| **LNG** | Liquid natural gas |
| **STP** | Standard temperature & pressure |
| **HC** | Hydrocarbon |
| **DPF** | Diesel particulate filter |
| **Fig** | Figure |
| **LH** | Langmuir Hinshelwood |
| **ER** | Eley-Rideal |
| **IE** | Ion exchange |
| **WI** | Wet impregnation |
| **IW** | Insipient wetness |
| **PGM** | Platinum group metals |
| **PVD** | Physical vapour deposition |
| **HAp** | Hydroxyapatite |
| **TEM** | Transmission electron microscopy |
| **SEM** | Scanning electron microscopy |
| **BET** | Brunauer-Emmett-Teller |
| **XRF** | X-ray fluorescence |
| **XRD** | X-ray diffraction |
| **TGA** | Thermal gravimetric analysis |
| **FTIR** | Fourier transform Infrared |
| **GHG** | Green house gases |
| **GWP** | Global warming potential |
| **OEM** | Original equipment manufacturer |
| **ECU** | Engine control unit |
| **EGR** | Exhaust gas recirculation |
| **SCR** | Selective catalytic reduction |
| **bcm** | Billion cubic meters |
| **HGV** | Heavy goods vehicle |
| **CC's** | Catalytic converters |
| **GPF** | Gasoline particulate filters |
| **TWC** | Three way catalyst |
| **cpsi** | Cells per square inch |
| **FAU** | Faujasite |
| **VDW** | Van der Waals |
| **FCC** | Face centred cubic |
| **BCC** | Body centred cubic |
| **Ea** | Activation energy |
| **UBMS** | Unbalanced magnetron sputtering |
| **CFUBM** | Close field unbalanced magnetron |
| **Geo** | Geothermal |
| **MFC** | Mass flow controller |
| **MAG** | Magnetron |
| **OSC** | Oxygen storage capacities |
| **MVK** | Mars-Van Krevelen |

# I. Abstract

The following research examines the synthesis of novel catalytic materials for the abatement of dual-fuel vehicle exhaust emissions using traditional wet impregnation (WI) approaches and the physical vapour deposition (PVD) technique unbalanced magnetron sputtering (UBMS). Characterisation of the materials was achieved *via* XRD, TEM, BET nitrogen adsorption, XRF, SEM, FTIR and TGA. Subsequent catalysts are tested on an in-house purpose built catalyst testing rig connected to a HP5890 MKII gas chromatograph. Low temperature CO and $CH_4$ catalysts prepared using a WI process produced full conversion of CO to $CO_2$ at room temperature and complete combustion of $CH_4$ below 300 °C. Magnetron sputtering at three different deposition rates produced 27 catalytic samples all converting CO below 200 °C and $CH_4$ for the majority of prepared catalysts below 400 °C. Zeolites were synthesised from a geothermal silica source and coated using both WI and PVD methodologies and demonstrated excellent activities for the oxidation of CO and $CH_4$, effectively oxidising $CH_4$ at a temperature 52% lower than currently being reported in literature. Hydroxyapatite was investigated as a potential substrate of interest and gave some promising results for CO combustion. Herein are the results for catalytic testing and characterisation of aforementioned materials.

# I. List of figures:

## III. List of Tables:

## IV. Acknowledgements

I would like to take this opportunity to thank my supervisory team, especially Dr Aidan Doyle who has given me the autonomy to run my project the way the results directed. The engineering department for making some of my stranger design ideas come to fruition. The coating lab especially Dr Justyna Kulczyk-Malecka and Prof Peter Kelly for their time and patience. The facilities plumbers Patrick, Paul and Phil who were always available for specialised advice. The technical staff in particular Dr Gary Miller and Dr Hayley Andrews, who were always keen to help, were forthcoming with ideas and let me jump the queue on more than one occasion.

## V. Author's Declaration

I declare that this thesis, has been composed solely by myself, and that it has not been submitted, in whole or in part, in any previous application for a degree. Except where it states otherwise by reference or acknowledgement, the work presented is entirely my own.

## 1. Introduction

### 1.1 The diesel engine – the workhorse of the industrial age

Rudolph Diesel invented the diesel compression engine in the 1890s in Paris, France.[1] With the invention of his engine, Rudolph Diesel had made a significant breakthrough in the power output of the engines at the time. The steam engine, which had been driving the industrial revolution since 1760 was only capable of 10% efficiency.[2] Rudolph Diesel's engine more than doubled the percentage efficiency to 26% and with improvements throughout history that figure is over 40% in today's modern diesel compression engines.[3] The compression engine provides power in a similar

way to a modern petrol injection engine. However, the key difference is the ignition of the selected fuel. The highly reactive qualities of petrol make spark-ignition a simple process. With a diesel engine, ignition is a little more complex. In order for the fuel to ignite the pressure of the fuel/air mix must be increased, hence the term 'diesel compression engine' only when the diesel is under increased pressure (230 psi) will there be enough heat in the system to ignite the fuel and drive the piston down.[4] The first part of this process is the intake or suction stroke. The piston as seen in figure 1 draws air in through the cylinder head, as the spring valve opens which is driven by the camshaft. Once the piston reaches the bottom position of its descent the spring valve closes. The piston then starts to move upwards increasing the air pressure in the cylinder, this part of the process is the compression stroke. Compression ratios vary, but are in the region of 12:1-22:1. At the end of the compression stroke, a metered amount of diesel is injected through an atomising nozzle into the cylinder. The injected fuel absorbs the increase in heat, from the compressed air and the molecules vaporize. The result is combustion and the generation of energy and the power stroke. The spring valves at the top of the cylinder head remain closed and the positive downward force generated by the combustion of the fuel drives the crankshaft in a rotary manner, thus turning the wheels. The combustion of the fuel leaves a residue of gases behind which are at high temperature and pressure. The camshaft now opens the exhaust valve and the emission gases, which are a composition of CO, $NO_x$, $CO_2$, hydrocarbon (HC) and $SO_x$ are expelled from the cylinder into the exhaust system for further treatment. The cycle then repeats itself and the vehicle continues its motion.

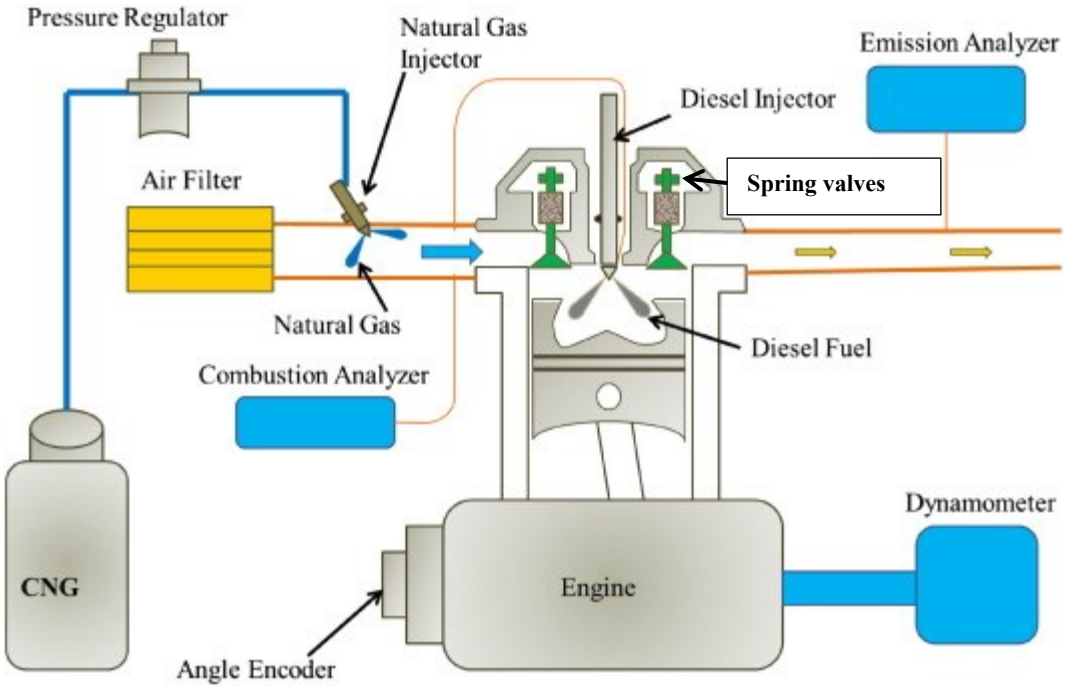


Figure 1 Simplified Diesel natural gas (dual fuel) engine[5]

**1.2 Dual fuel**

In a dual-fuel diesel / natural gas vehicle there is no need to change the fundamental requirements of the engine. An adjustment enabling $CH_4$ introduction in to the fuel feed is required, but not at the cost of an expensive engine upgrade.

The amount of $CH_4$ substituted into the fuel mix can be as much as 90% thus reducing the amount of diesel being combusted. It is estimated that per truck, this can save the owner £13,000 each year, based on 60% substitution of natural gas.[6] Other cost saving motivations include increased fuel economy, return on investment in 3 years and preservation of resale value of the unit, due to simplicity of conversion back to out-and-out diesel only.[7] Dual-fuel systems also have the capacity to run on diesel only when the liquid natural gas (LNG) or compressed natural gas (CNG) run out and there is little difference in torque and efficiency.[8]

Dual fuelled diesel/natural gas vehicles have reduced the amount of $NO_x$ and $CO_2$ entering the environment *via* the exhaust, however as a direct result the amount of CO and $CH_4$ (all potent greenhouse gases (GHG)) have dramatically escalated.[9] The amount of $CO_2$ equivalent ($CO_2^e$ ) has

also risen by as much as 50-127%.[10] $CO_2^e$ is a more accurate way of determining the amount of $CO_2$ entering the atmosphere and encompasses all GHG. $CO_2^e$ is calculated by multiplying the mass of combustible material by its global warming potential (GWP). Thus 1 kg of $CH_4$ can produce 25 kg of $CO_2^e$.[11] Despite the obvious cost benefits to the transport industry and the reduced emissions of certain gases dual fuelled vehicles are only addressing some of the issues related to the combustion of gasoline. By oxidising $CH_4$ and CO to $CO_2$, a greenhouse gas is still being emitted; however $CO_2$ does not remain in the atmosphere as long as $CH_4$ and does not exhibit as serious health risks compared to CO and $NO_x$.[12]

The technology for the use of a dual-fuel system was designed and is patented by G-volution and the basis of the optimiser is the emulation of the primary injector pulse signal.[13]

Emulating and interpreting the primary injector control signals enables the original fuel demand to be mapped into the individual demands for a number of fuels (primary, secondary or tertiary fuels.[14]

The optimiser is distinctive as it is the only patented system of this type. Operating in this mode offers a number of important benefits. The original equipment manufacturer (OEM) engine control unit (ECU) remains the master for the engine control loop. The optimiser acts as a slave, translating the primary fuel control signals and managing the alternative fuel system. The optimiser is effectively transparent to the OEM ECU and thus the OEM ECU continues to operate normally.[15]

The engine power and torque features are preserved because the engine is running on the maps under the control of the original OEM ECU at all times. The optimiser changes the ratio of diesel and natural gas. The optimiser and alternative fuel system is calibrated to ensure that there is effectively no difference in the performance or response of the engine.[16]

Because the optimiser functions on the primary fuel control signals, it is inside the control system feedback loop. Therefore, it works in sympathy with the control loop, rather than against it.

For example, as seen with other systems on the market, changing the throttle pedal demand or altering the fuel rail pressure to reduce the primary fuelling would perturb the control loop and potentially introduce instability or force it to a new operating point.[17]

The fact that the optimiser works in real time inside the control loop, means that it can operate effectively all of the time. Therefore, there are no conditions which prevent operation on multiple fuels (including during gear changes and high transient operation).

Because of the OEM ECU maintains control of the engine all of the emission control strategies remain unaffected. The start of injection (hence ignition timing), which is not affected by the optimiser, nor is the control of exhaust gas recirculation (EGR) or selective catalytic reduction (SCR) systems (if fitted).[18]

The optimiser does, however provide the capability to alter the ratio of the multiple fuels in real time, dependent on the operation conditions of the engine. This provides a new degree of freedom in fuelling the engine, enabling optimisation for power, economy or emissions dependent on the characteristics of the individual fuels used.[19] Linked to the capability to run two separate fuels in one system efficiently is the abundance of natural gas.

**1.3 Natural gas**

Natural gas can be located in oil fields, coal beds and gas fields. In its untainted form, natural gas is colourless and odourless. It is a flammable gas that when ignited emanates a substantial amount of energy $\Delta H$ = -882.0 kJ $mol^{-1}$.[20] Often mentioned as a clean fossil fuel, as it is not as detrimental to the environment as crude oil and coal. During the combustion of natural gas, emissions of sulphur dioxide ($SO_2$) are inconsequential and emissions of nitrogenous oxides ($NO_x$) and carbon dioxide ($CO_2$) are greatly reduced in comparison with diesel only combustion, which consequently helps in the reduction of complications linked with acid rain, the ozone layer and greenhouse gases. Concurring with the BP Statistical Review of World Energy (2015), the total worldwide proved reserves of natural gas were 187.1 trillion cubic meters.[21] In comparison it is estimated that

including OPEC and non-OPEC nations, there are 243 trillion litres of crude oil in reserve.[22] Consumption of crude oil in 2010 was 86.4 million barrels per day, it is estimated that current consumption is 99 million barrels each day (16 billion l) a massive 6 trillion every year.[23] In comparison the world consumed 96 billion cubic meters (bcm) of natural gas in 2017.[24] Natural gas originates from any one of three major processes: thermogenic, biogenic, and abiogenic processes.[25]

### 1.3.1 Thermogenic

A process which involves the comparatively slow decay of organic matter taking place in sedimentary basins under the impetus of great pressures and temperatures that can be associated with increased depth. Subsequently natural gas (also called thermogenic $CH_4$) and petroleum are formed.[26] Living organisms degrade debris from organisms in an anaerobic environment; this degradation is slow, thus incomplete. Residues then amass in the sediments forming intricate macromolecules, with structures known as kerogen.[27] The thermal decomposition of kerogen generates HCs as well as non-HC compounds such as; $CO_2$, $H_2S$, $H_2$, $H_2O$ and $N_2$ and a layer called pyro bitumen, which is high in carbon concentration.[28] Thus the processes breakdown into two unique kerogen fractions; labile and refractory. Labile kerogen is responsible for the formation of crude oil and gas, whereas refractory causes gas temperatures in the range 150- 220 ˚C. [29]

### 1.3.2 Biogenic

In this process, $CH_4$ is created by the activity of living organisms (methanogenic bacteria) on organic matter during the growth of the sediment layers and in the early part of their burial.[30] The methanogens are abundant in sites where electron acceptors such as $O_2$, $NO_3^-$, $Fe_3^{+,}$ and $SO_4^{2-}$ are limiting. Common sites of methanogens include anaerobic digesters, anoxic sediments, flooded soils, and gastrointestinal tracts.[31] The methanogenesis from oil or coal involves different process through the activity of a variety of groups of micro-organisms.[32]

1. Acidogenesis: heterotrophic bacteria hydrolyse large complex organic polymers to produce smaller simpler substrates, for example; sugars, volatile fatty acids, and alcohols.

2. Acetogenesis: fermentation of these simple substrates *via* syntrophic bacteria producing acetate, $H_2$, and $CO_2$.

3. Methanogenesis: formation of $CH_4$ from fermented products *via* methanogenic Archaea.

For the exploration of petroleum, the difference between thermal and bacterial gas is necessary. In a thermal gas basin, oil must firstly form, but, this is not the case in a bacterial gas basin. Therefore, exploratory techniques must be planned differently.[33]

### 1.3.3 Abiogenic

In this process, the initial materials are volcanic gases (not organic matter). $CH_4$ is produced by the reduction of $CO_2$ during the cooling of magma, this is often observed in hydrothermal systems during the interaction between water and rock.[34]

## 1.4 Hydraulic fracturing

A reservoir of gas is a naturally occurring storage area; it comprises permeable rocks that often have high porosity, such as; sandstone, these porous materials are enclosed by impermeable layers.[35] Natural gas gathers in pockets below the surface and migrates through sub-surface faults and fissures until arriving at a gas reservoir.[36,37,38] In order to access the gas stores a process called hydraulic fracturing (fracking) is used. There have been several implications that have mired the fracking industry with a bad reputation, including the contamination of surface and ground water and the release of $CH_4$ into the atmosphere.[39,40] However, natural gas is abundant and a cleaner fossil fuel than oil or coal, therefore it is essential that this fuel be used in conjunction with existing technologies.

### 1.5 Methane ($CH_4$)

The main constituent of natural gas is $CH_4$, it has a tetrahedral 3-dimensional shape, with bond angles of 109.5°. The heteronuclear diatomic promotes a 2s electron into a vacant P-orbital producing an $sp^3$ hybridised molecule. The carbon atom donates four electrons to bonding, the best way to picture this, is to envisage the c-electrons sitting at the outer most points of the $sp^3$ hybridised orbitals. It is important to note that the nodes sit on the carbon, reducing any potential issues with anti-bonding orbitals. $CH_4$ is in abundance on the planet and may just be the answer in reducing harmful diesel emissions, but full conversion to $CO_2$ in rich oxygen conditions is not so simple. The $CH_4$ molecule has the highest hydrogen to carbon ratio and is a stable at standard temperature and pressure (STP) making the removal of the hydrogen atoms from its central carbon a reaction that requires a great deal of energy. The typical activation energies required to remove the hydrogen atoms from the carbon are 80 – 100 kJ $mol^{-1}$.[41] These are energies that can certainly be replicated in the exhaust system of a vehicle; therefore, a method to catalyse this reaction is an achievable goal. Herein the use of transition metal oxides, redox cyclic promoters and precious metal activity to achieve 100% conversion of $CH_4$ to $CO_2$ at stoichiometric concentrations is examined. The activation methane by heterogeneous catalysts will have an important role to play in the provision of energy in the future. As the main component of natural gas BP in their annual statistical review reported that $CH_4$ concentrations in natural gas are between 70 and 90% and proven world reserves for the year 2013 were 187.3 x $10^{12}$ $m^3$.[42] The shale gas revolution with countries such as USA and China having huge reserves has triggered an increased interest in gas as a fuel source.[43] Despite being readily available $CH_4$ is underrepresented as a fuel stock.

The challenges that arise using $CH_4$ are due to the stability of the molecule and its lack of a dipole and thus also its susceptibility to nucleophilic attack. $CH_4$ is an exceptionally weak acid with a $pK_a$ ~40 and it has a poor affinity towards protons.[44] According to Schwarz *et al* the most simplistic way for the activation of $CH_4$ is *via* the homolytic cleavage of the C-H bond and the hydrogen atom transfer forming a radical species.[45]

Results herein demonstrate that high temperatures are required for the heterogeneous activation of $CH_4$. The partial catalytic oxidation of $CH_4$ to produce synthesis gas or syngas is well studied and is the first reaction step that is the basis for the results reported.

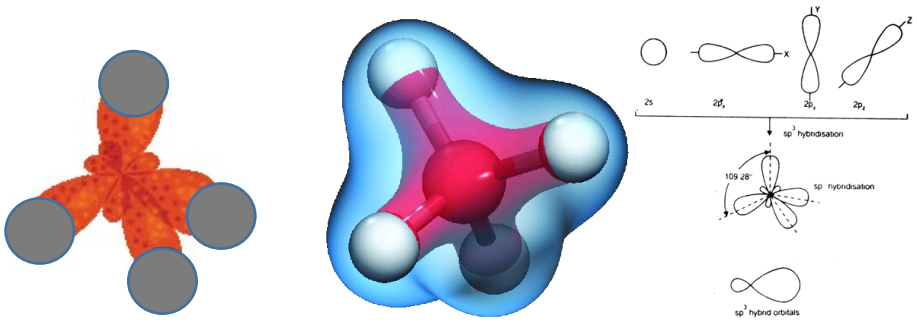


Figure 2, $CH_4$ molecule demonstrating electron density/probability and orbital geometry[46]

**1.6 Carbon monoxide (CO)**

The heteronuclear diatomic comprises a carbon atom triple bonded to oxygen leaving a lone pair on oxygen and carbon as seen in figure 3. Carbon atomic orbitals, which are at a slightly higher energy than there oxygen partner, donate 4 electrons to the molecular orbital.[47] The 2s electrons are donated to the σ bonding and anti-bonding orbitals and the 2p electrons fill the remaining σ and π bonding orbitals. Oxygen, which has 6 valence electrons, donates in the same manner, filling the remaining 2p orbitals, forming a stable molecule. CO is one of the most documented and publicly known vehicle exhaust gases, emitted from all combustion engines. If allowed to reach dangerous concentrations in an enclosed area, the binding affinity of CO over $O_2$ makes it fatal to humans. Known as 'the silent killer', CO is a colourless, odourless and non-irritating gas.[48] If the early signs of CO poisoning are ignored, a person can become unconscious quickly and be unable to escape the environment, lethal levels depend on time exposed but 4000 ppm or less is lethal in 1 hour.[49] The largest producers of CO in the atmosphere are vehicles. The room temperature complete oxidation of CO to the less harmful and non-polluting $CO_2$ has been well documented. The two key areas for any catalytic material are; catalytic activity and stability. A good catalyst needs

to convert all CO quickly and at low temperature and it needs to be able to do this for a sustained period of time.

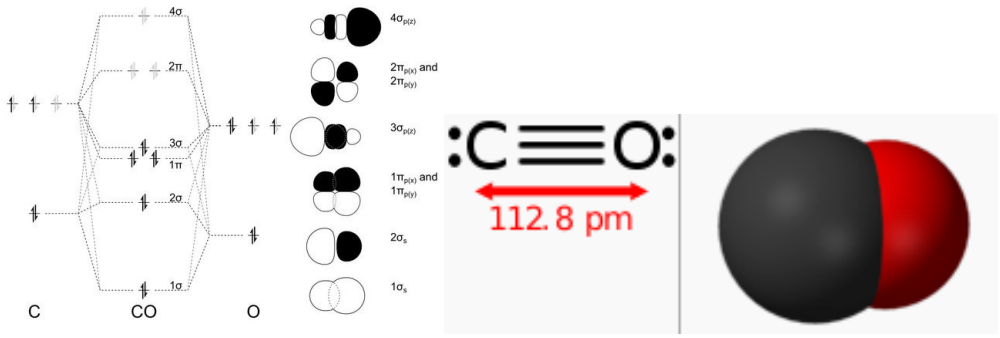


Figure 3 MO diagram and illustration of CO including electron probability density[27]

### 1.7 Pollutants

Diesel engines produce significant levels of black soot and other organic compounds, which are hazardous to health and the environment. This is in part, due to incomplete combustion, but also a direct effect of burning diesel in an internal combustion engine. The most detrimental to human health and the environment being nitrogenous oxides ($NO_x$), CO and $CH_4$.[50] Due to the increase in industrial processes, emissions of greenhouse gases such as the ones previously mentioned has become an international problem.[51] The reduction of greenhouse gases from the exhaust systems of combustion engines is a hot topic. Most catalytic convertors are poor at oxidising these gases at low temperatures, thus most of the pollutants released *via* the exhaust occurs in the first few minutes of starting the engine.[52]

### 1.8 Emission standards

**Table 1 European standards for heavy goods vehicles**

| Legislation Category | CO (g/kWh) | HC (g/kWh) | $NO_x$ (g/kWh) | PM (g/kWh) |
|---|---|---|---|---|
| Euro I | 4.5 | 1.1 | 8.0 | 0.61 |
| Euro II | 4 | 1.1 | 7.0 | 0.15 |

| | | | | |
|---|---|---|---|---|
| Euro III | 2.1 | 0.66 | 5.0 | 0.13 |
| Euro IV | 1.5 | 0.46 | 3.5 | 0.02 |
| Euro V | 1.5 | 0.46 | 2.0 | 0.02 |
| Euro VI | 1.5 | 0.13 | 0.4 | 0.01 |

The legislation on the amount of harmful vehicle emissions produced by motor vehicles was introduced in the 1970s. Since that time, the regulating body has tightened the control over the amount of harmful gaseous emissions being emitted *via* the exhaust system, but where did it all start? Euro I regulatory standards were implemented in 1992, with the simple mission to ensure all new vehicles being manufactured were fitted with a catalytic converter and to set a limit on the emission of $NO_x$, CO, HC and particulate matter (PM). The Euro I standards were designed to govern all vehicles registered from the 1st January 1993 and although, they were in their own right a revolutionary step in the right direction, they were just that, a single step.

In 1997, the EU took the second step and introduced Euro II standards on all vehicles registered from the 1st January that year. The new emission standards for petrol and diesel vehicles were considerably tighter than Euro I, the most significant cinching was observed in the levels of CO and PM, with decreases of 11.1 and 75% respectively.[53] Although not as pronounced as the PM and CO reduction, there was still a compelling reduction of $NO_x$ by 12.5%.

By the start of the millennium and valid for all cars registered from the 1st January that year the EU made the decision to separate the emission standards for the overall production of $NO_x$ and HC. This was a game changer for the monitoring and manufacture of all new vehicles and was the instigation of the loss in faith for the diesel engine. A further reduction in the amounts of CO and PM that was considered acceptable was governed necessary. This meant a further reduction of these harmful by-products of 47.5 and 40% respectively, was required by law, a massive 53.3%

decrease for CO from Euro I legislation. Euro III observes a slight relaxation in the reduction of PM, but it is just that, and in the following legislation there is a significant reduction.

All vehicles registered from the 1st January 2006 (Euro IV) are subsequently compelled to adhere to Euro IV legislation across Europe. The impact on the $NO_x$, PM and HC emissions in this latest EU legislation is tangible, with a reduction of 84.6% for PM, 30% for $NO_x$ and 30.3% for HC and CO by a further 28.6%. The significant reduction in the amount of diesel PM is achieved with the introduction of filters or diesel particulate filters (DPF's) that are capable of trapping 99% of this noxious emission.[54]

The use of DPF's negated the next round of legislation to be increasingly strict on the level of PM, the following Euro V emission standards were implemented for all vehicles registered after the 1st January 2011. The data clearly show no reduction in PM, for $NO_x$ 42.8%, HC remained the same, as did CO. As previously mentioned the real factor in the extensive cutback of PM is the legality that all diesel vehicles were fitted with DPF.

Historically heavy goods vehicles (HGV) $NO_x$ emissions have struggled to stay in the limits set by the legislating body. In 2013 the Euro VI emission standards for diesel vehicles were introduced; the new legislation is designed to globally synchronize vehicle emissions. The harmful effect of $NO_x$ to people who live and work near busy roads has had a great deal of publicity in the media. A report by 'Phys Org' on the 18th September this year suggested that at least 5000 deaths in Europe each year can be directly attributed to $NO_x$ emissions.[55] Therefore, personal diesel vehicles look set to become obsolete, unless an answer to the problem of harmful emissions can be found. With the battle against PM all but won, Euro VI legislation turned its attention on $NO_x$ and HC emissions. The increasing association of $NO_x$ and severe health problems and or death has all but obliterated European opinion on the diesel internal compression combustion engine. The latest round of cuts on emissions has stated that all vehicles need to further reduce the amount of $NO_x$ by a massive 80%. From the Euro I to the current legislation the EU has reduced vehicle gas emissions massively.

CO has dropped by 66.7%, PM by 98.4%, HC 88% and $NO_x$ by 95%, but is this enough? What are acceptable levels? The gases that are currently being churned out of combustion engines all over the globe are responsible for more than just the bad health on an ever increasing population. The impact on our planet is alarming, from the loss of species to the global threat of rising sea temperatures. Surely zero emissions are the only acceptable solution and or the move away from petroleum based products.

**1.9 Development of Catalytic Converters**

The development of catalytic converters (CC's) is an important evolution in the history of the automobile. The use of CC's in the 1970s demonstrated a totally new technology. The first used were oxidation catalysts designed to reduce CO and hydrocarbons and contained platinum and palladium.[56] The CC has to work under a variety of differing conditions, from cold start through acceleration, deceleration, braking, short and long distance journeys.[57] The CC is one of the most important scientific developments of the modern age. Since the introduction in the 1970s the use of precious metals to activate catalytic supports has seen vast amounts of Pt, Pd, Rh and Au mined from the earth. Despite the introduction of CC to all automotive vehicles, the rapid expansion of greenhouse gas emitting vehicles has increased dramatically in the UK alone. A report by Michael McCarthy in the Independent compared the number of people without access to a vehicle in the 1970s was 48% in comparison to 22% in 2008.[58] Coupled with a 10 million increase in the number of people living in the UK in this period, the levels of greenhouse gas emissions by vehicles looks set to increase in the near term.

### 1.9.1 Conventional catalytic converters

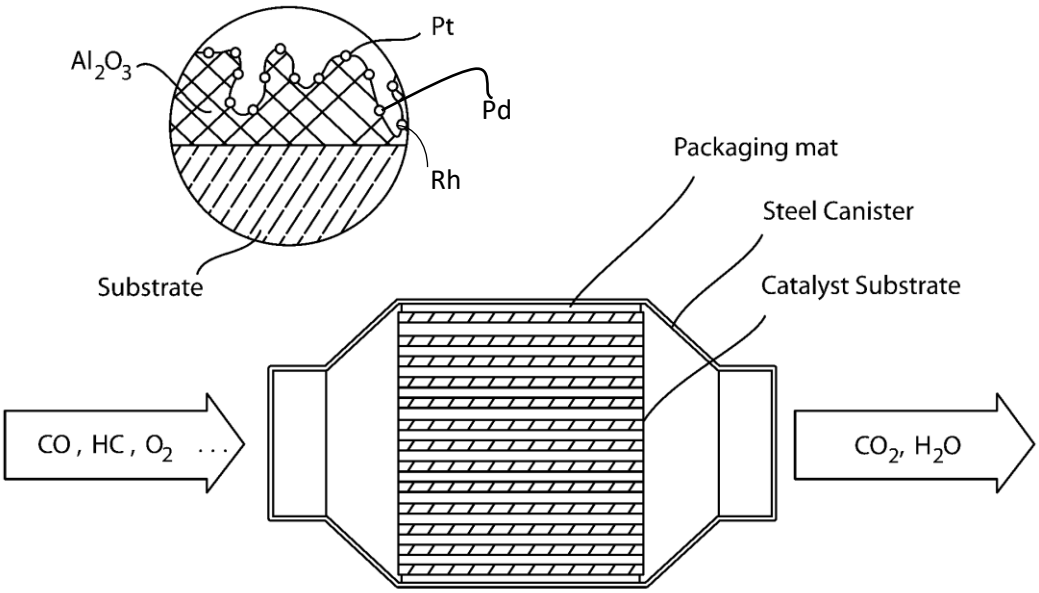


Figure 4 Conventional Catalytic Converter[59]

Conventional three-way catalysts consist of a honeycomb structure or an inert support with a porous wash-coat containing platinum, palladium or rhodium coated on the surface. Essentially, they work by oxidising CO and HC and reducing $NO_x$, thus reducing harmful emissions. However, the issue with current catalytic converters is the inability to reduce these emissions to an acceptable level and the lack of activity in the first few minutes of starting the engine.[60] The catalytic convertor is located in a metal box situated in between the tail pipe of the exhaust system and the engine block.

The filter is a ceramic substrate where the gas is forced to flow over the substrate material, this filters out PM with more than 99% efficiency for DPFs and up to 80% for Gasoline Particulate Filters (GPF). Inside the box, the ceramic material is protected from mechanical damage by a shock-absorbing mat. The filters have a catalytically active coating similar to that used on the CC, this increases the activity of the system and is sometimes coated with a material

to help regeneration and prevent loss in functionality over time. For example Selective Catalytic Reduction (SCR) coating on DPF or Three-Way Catalyst (TWC) on GPF.[61]

Substrate technology on which the active catalytic material is supported, has seen many advances over the years. The first ceramic substrates had a density of 200 cells per square inch (cpsi) and a wall thickness of ~0.3 mm. By the end of the 1970s, the cell density had increased to 400 cpsi with a wall thickness greatly reduced by 50% to 0.15 mm. Today 400, to 1200 cpsi substrates are available and wall thickness can be reduced almost 0.05 mm.[62]

The substrates on which the active catalytic materials are supported are ceramic or metallic, each offers its own advantages for particular applications and situation in the exhaust system. The development of robust ultra-thin wall support materials with cell densities of 1200 cpsi has been a determining factor in the increasing efficiency of catalysts. [63]

### 1.10 Catalytic Substrates

The design of catalysts for the oxidation and reduction of vehicle exhaust gases has a two stage requirement. Firstly the demand for materials that catalyse the gases of interest, but just as important are the substrates for which these reactive species are deposited. In the search for a catalyst to reduce the temperature at which $CH_4$ and CO are oxidised a number of considerations were investigated. These included; the mechanical and chemical stability of the support material, the surface area porous nature of the supports and cost.

#### 1.10.1 Zeolites

Naturally occurring zeolites have been known for almost 250 years. For the scientific community, specifically heterogeneous catalysis they are of great interest due the porous nature and massive surface areas. However, due to undesirable impurities and varying compositions in the natural forms they are of limited value commercially. It wasn't until the early 1950s that this class of porous material was prepared synthetically that it began to play an out reaching role in the field of catalysis. In 1962 an important laboratory breakthrough was the synthetic synthesis of faujasites (zeolites X and Y) and their application in fluid catalytic cracking of petroleum, one of the biggest

chemical processes worldwide. The new zeolites were considerably more active than the silica-$Al_2O_3$ materials that were being used, thus they were capable of yielding a notable increase in volume of gasoline. It is believed that the yield enhancement to the petroleum industry was worth billions in US dollars each year.[64] One of the most important uses for the newly synthesised zeolites is the hydrocracking of heavy petroleum distillates.[65] Their use in the production of fine chemicals is at present limited, however there is a considerable potential in this area.[66] The elemental structural compounds of zeolites are $SiO_4^{4-}$ and $AlO_4^{5-}$ tetrahedra. Adjacent tetrahedra bond at their corners *via* an oxygen atom, resulting in an inorganic macromolecule which has a structurally defined 3D framework. It has been observed that the net formulae of the tetrahedra are $SiO_2$ and $AlO_2^-$ thus, it is the $Al_2O_3$ centre that carries the negative charge at the centre. The zeolite framework contains channel mesh intersections with dimensions from ca. 0.2 to 1 nm. Residing in these pockets are water molecules and small cations which help to stabilise the negativity.

Hence the composition of zeolite can be expressed with the following formula:

$$A_{y/m}{}^{m+}[(SiO_2)_x \bullet (AlO_2^-)_y] \bullet zH_2O \qquad (18)$$

The (A) is a cation with the charge *m*, *(x + y)* is the number of tetrahedra per crystallographic unit cell and *x/y* is the so-called framework silicon/aluminium ratio $n_{Si}/n_{Al}$ (or simply Si/Al). These silicon and aluminium atoms in $Al_2O_3$-silicate zeolites are commonly referred to as T-atoms. The diagram in figure 5 reveals the structure of zeolite Y and the pocket system and pore diameter. In these commonly used schematics, the T-atoms are located at the vertices, and the lines connecting them represent T-O-T bonds. This particular catalyst is formed with a 12 $TO_4$ tetrahedra geometry with pore size diameters of 7.4 Å.

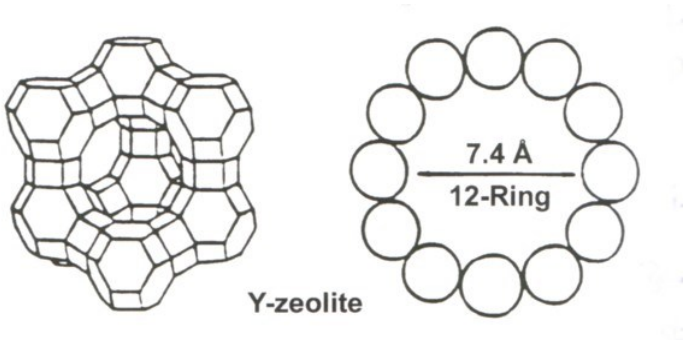


Figure 5 Schematic line drawings of zeolite Y, pore diameter and T-atoms structure[67]

Figure 6 reveals structures of four selected zeolites and their pocket systems and pore dimensions. The top line of figure 6, 24 tetrahedra bond to form a cubo-octahedron, referred to as a sodalite unit or β-cage. This structure is important as several zeolites contain this secondary formation. When sodalite units bond in this specific formation, as can be seen in figure 6 the resulting faujasite is created and importantly it is undistinguishable to the structures of the synthetic zeolites X ($1<n_{Si}/n_{Al}<1.5$) and Y ($n_{Si}/n_{Al}>1.5$).

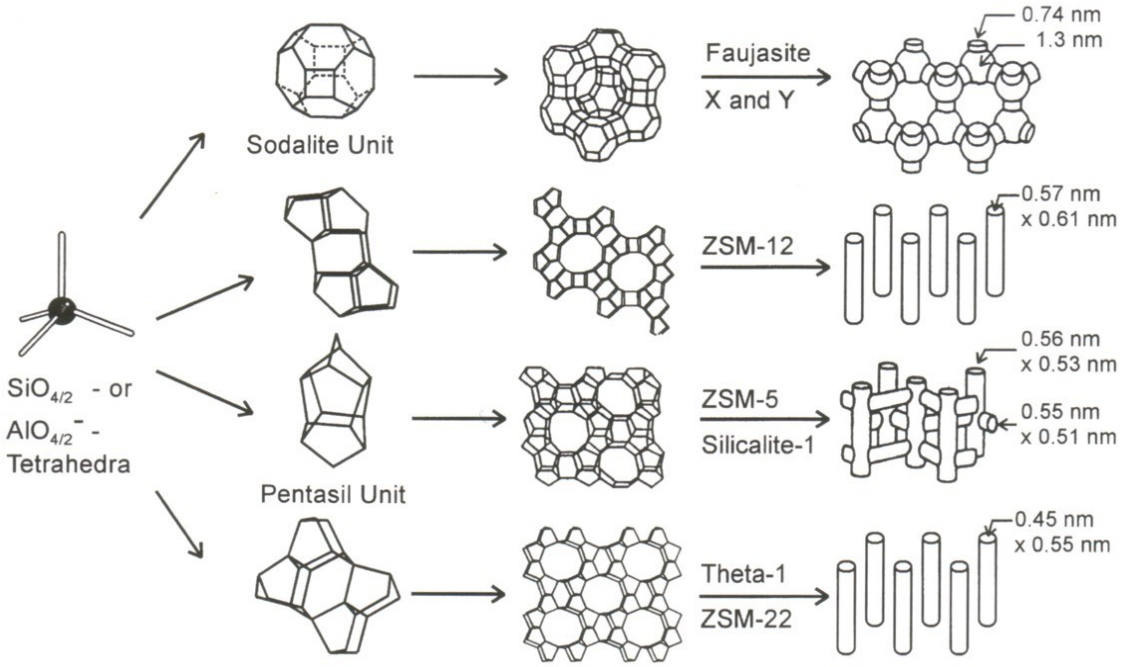


Figure 6 Structures of four selected zeolites (zeolites X and Y; ZSM-12; ZSM-5 and silicalite-1; Theta-1 and ZSM-22) including micropore systems and dimensions.[68]

Some of the unique features of zeolites when compared to conventional solid catalysts or catalyst supports are (a) pore diameter uniformity and (b) pore width in the order of molecular dimensions. According to the IUPAC definition, porous materials are divided into three classes, based on their pore diameter: microporous <2 nm, mesoporous 2-50 nm and macroporous >50 nm.[69] Thus, most zeolites are classed as typical microporous materials. However, their relatively small pore diameters limit their application, hence the branch of chemistry which explores modification of their structure, specifically their pore sizes. One such method for increasing the size of the pores to the mesoporous range is the removal of aluminium *via* steaming.[70] Figure 7 reveals the presence of two distinct mesopores with dimensions in the range 2 – 6 nm, these pores were formed following the steam removal of aluminium from zeolite Y.

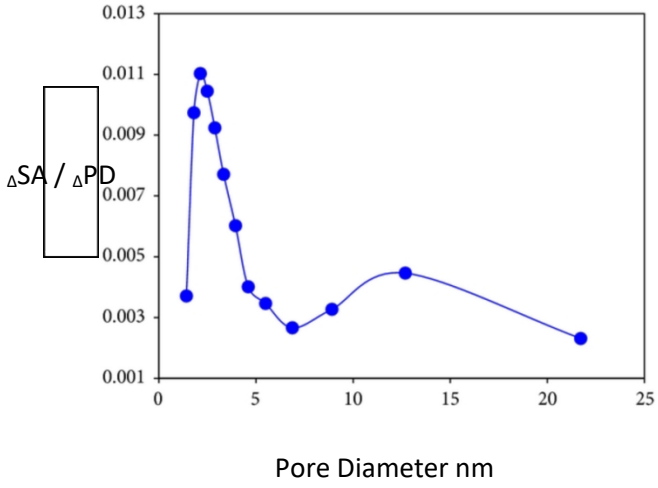


Figure 7 Pore size distribution of dealuminated Y zeolite using steam.[71]

### 1.10.2 Alumina

Aluminium oxide or alumina, $Al_2O_3$ is synthetically produced from the mineral bauxite.[72] It is used for predominantly smelting into raw aluminium metal and also in ceramics. Bauxite, contains $Al_2O_3$ filled hydrous pockets. Noteworthy precious gems such as ruby and sapphire are also $Al_2O_3$ and can be synthetically produced from bauxite, however, predominantly it is produced for the ceramics industry and the numerous products therein. $Al_2O_3$ is still melted in electric furnaces from bauxite, however, this process was developed for the abrasives industry in the early 20$^{th}$

century and has been in most parts replaced by the Bayer method.[73] Developed in the late 1800s the Bayer process crushes the bauxite and mixes with sodium hydroxide and seeding crystals to precipitate aluminium hydroxide. The hydroxide is then heated to drive off the water leaving varying grades of $Al_2O_3$; including activated- $Al_2O_3$, smelt grade $Al_2O_3$ and calcined $Al_2O_3$. Activated $Al_2O_3$ is used as a substrate for many catalytic materials and as a method for removing water from gases and liquids. The smelt grade $Al_2O_3$ is the main product of the Bayer process, comprising 90% of all the $Al_2O_3$ produced. This grade oxide is transported to aluminium plants where it is electrolysed to produce raw aluminium metal. Calcined $Al_2O_3$ is the most commonly known and therefore utilised product.[74]

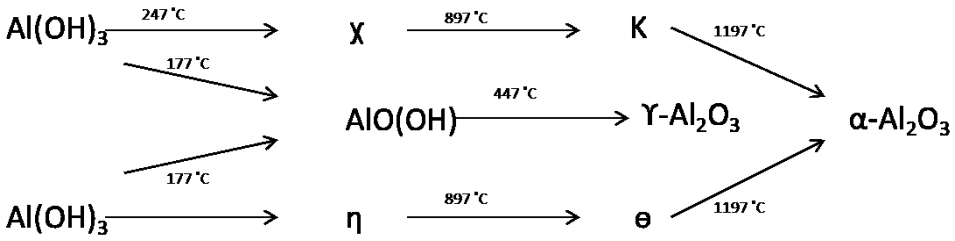


Figure 8 Demonstration of the dehydration process to form different species of $Al_2O_3$.[75]

It is used in the medical profession for dental and bone implants, it is used as a refractory coating in kilns due to its high melting point > 2000 °C. Due to its low conductivity it is used as an insulating product on spark plugs. Coupled with its low conductivity, resistance to chemical attack, high melting point and 9 Mohs hardness rating come together to make $Al_2O_3$ invaluable and versatile product. In fact these few examples do not really scratch the surface, $Al_2O_3$ is a multi-billion dollar business, just the ceramics and resistant coatings alone generate $500 billion per year.[76]

The chemical structure of alumina is $Al_2O_3$, it has an octahedral and tetrahedral geometries with differences caused by how the oxygen layers line up with each other. Therefore, the 2 Al atoms carry a +3 charge in order to balance the -6 shared over the 3 O atoms.

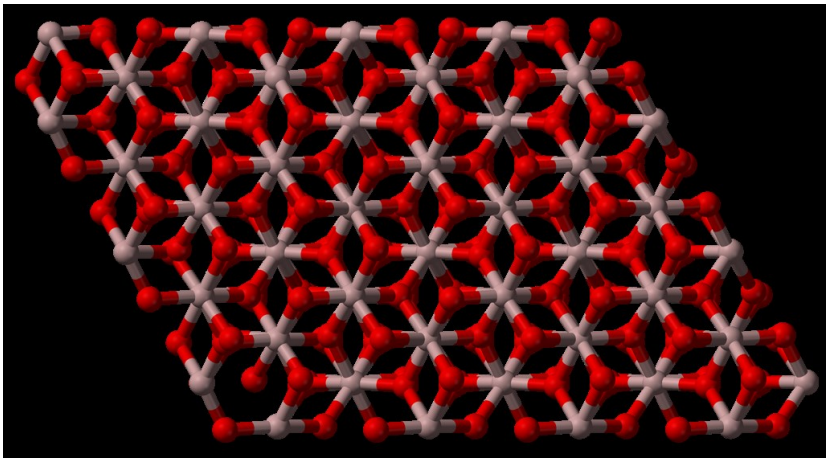

Figure 9 $Al_2O_3$ crystal structure[77]

### 1.10.3 Titania

Titania or titanium dioxide,$TiO_2$ is a polymorphic crystal that exists in several forms, the most common and important of which are; anatase and rutile. It is a colourless odourless substance used in a variety of industrial applications. Titanium dioxide is used as a bleaching agent in porcelain enamals it gives them the brightness, acid resistance and hardness they are noted for. In more recent times $TiO_2$ has been utilised in cosmetics, such as sunscreen lotions, as they claim that titanium dioxide protects the skin by absorbing the harmful ultra-violet light.

Under exposure to UV light, $TiO_2$ coatings exhibit self-cleaning and disinfecting properties. Alloys of $TiO_2$ are well documented as being lightweight and having excellent tensile strength, especially at high temperatures. The high resistance to corrosion and an ability to withstand extreme temperatures has made them a main component principally in aircraft, armored plating, power plant pipes, naval ships, missiles and even spacecraft.[78] However, $TiO_2$ has also come under scrutiny recently and has been given a class 2 carcinogen as breathing the dust can be harmful.[79] Despite this recent negative press, $TiO_2$ remains a useful chemical weapon in the fight against global pollution events.[80] The photocatalytic activity of the compound has led to a thorough understanding of the material and its properties and potential application. It is utilised extensively in many heterogeneous catalysis applications, including waste water treatment and the separation

of gases. One of the key features of $TiO_2$ that makes it useful for a variety of different applications is the ability to vary its surface properties.

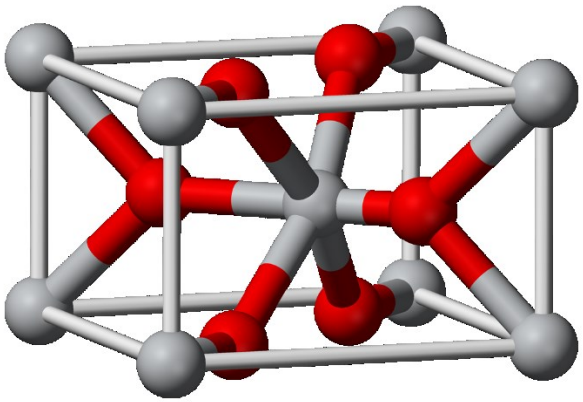

Figure 10 crystal structure of $TiO_2$[81]

### 1.10.4 Hydroxyapatite

Hydroxyapatite is the inorganic component of bone tissue.[82] The inorganic material constitutes 60-70% of all bone material and provides bone with its strong inflexible quality.[83] The biological characteristics of synthetic HAp have been extensively reported for use in medical applications. HAp has superb bioactivity, biocompatibility and non-inflammatory properties.[84] Due directly to these properties, HAp has been applied to dental applications and bone grafts, as it has the ability to bond with organic tissue after a medical procedure.[85, 86]

HAp has been utilised as a support for precious and transition metal doping for the oxidation of $CH_4$, CO and the reduction of $NO_x$.[87,88,89,90,91] HAp was chosen as a support for metal doping as it demonstrates a relatively high surface area, is stable under a wide temperature range and is durable.[92] HAp is not soluble in pH ranges near neutrality and is stable in basic solutions.[93,94,95,96]

## 1.11 Mechanisms of heterogeneously catalysed reactions

### 1.11.1 Langmuir-Hinshelwood and Eley-Rideal

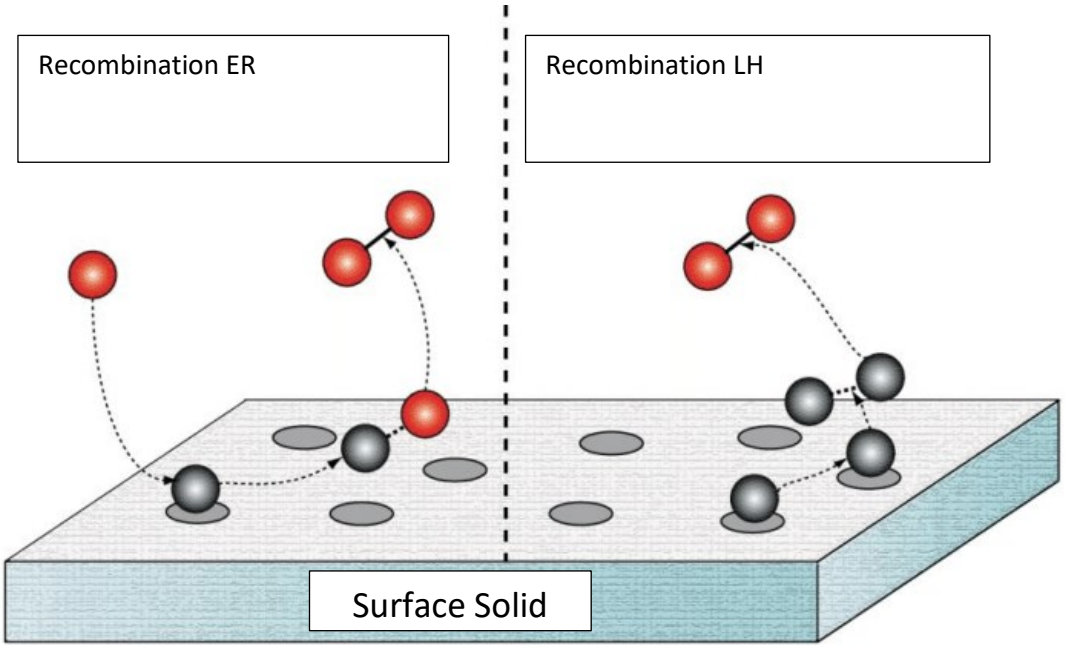


Figure 11 Eley-Rideal versus Langmuir-Hinshelwood reaction mechanism.[97]

Heterogeneous catalysis must always be preceded by adsorption. The two well documented pathways for this are Langmuir-Hinshelwood (LH) and Eley-Rideal (ER) mechanisms. However, it is important to note that even though the LH mechanism is more often observed, the distinction between the two can be blurred. LH is an atomic reorganisation of species on the surface of the catalyst. ER however, observes a bound species reacting with a gaseous species when it invades its space. There are three possible states of adsorption; physical adsorption, chemisorption and antecedent states.

### 1.11.2 Heats of adsorption

Physisorption, describes weaker interactions, such as dipole-dipole/ quadrupole or van der Waals (VDW) forces. Typically they have small enthalpy changes in the region of -10 to -40 kJ $mol^{-1}$ and heats of adsorption, ΔH between 10-40 kJ $mol^{-1}$. Chemisorption, however is the breaking and making of new bonds from the gaseous state onto the solid state, therefore ΔH range from 80-400 kJ $mol^{-1}$. It is exactly this process, that dictates the type of catalyst required for different reactions.[98]

### 1.11.3 Reactions on solid surfaces

Different gaseous species will react with different solid surfaces. This specificity for the reaction of chemicals is observed regularly for many metals, oxides and non-metals. Importantly at low coverage of physisorption there is definitely a level of specificity, albeit not as profound as with chemisorption. This specificity however, is lost as the layers accumulate and subsequently condense over the surface. With chemisorption, however other considerations need to be investigated. For example, not all gas molecules are going to adsorb as they approach the solid surface. Some molecules may potentially redistribute back into the gas phase with a zero loss of energy. There is a chance that a gaseous molecule will surrender significant translational energy toward the solid and be entrapped in the physically adsorbed state. Conversely, the opposite may also occur if a gas molecule with the correct energy strikes the surface in the correct orientation and required energies, it may bypass the physisorption state and become instantly chemically adsorbed. So, if this is true, then it must also be possible that a physisorbed molecule can pass to the chemisorbed state, be redistributed into the gaseous state, or even move to adjacent site, where the above is true on repeat. Therefore, it is also plausible that chemically absorbed molecules either stick firm on first impact, move around until they find an acceptable energy/orientation or continually move across the solid surface.

### 1.11.4 Potential energy

These different subtleties can easily be demonstrated experimentally using techniques such as XRD, XRF, BET N2 adsorption, NMR, XPS, Mossbauer spectroscopy, XANES, FTIR. To acknowledge these different mechanisms, potential energy diagrams such as the one in figure 12 are used to describe the energies of molecules as they approach the solid surface. The importance of the $E_{mp}$ and $E_{mc}$ are obvious when one considers surface non-uniformity. Pores may vary in size and abundance, previously adsorbed layers will affect the energies as will molecules desorbing and in the process of migration.

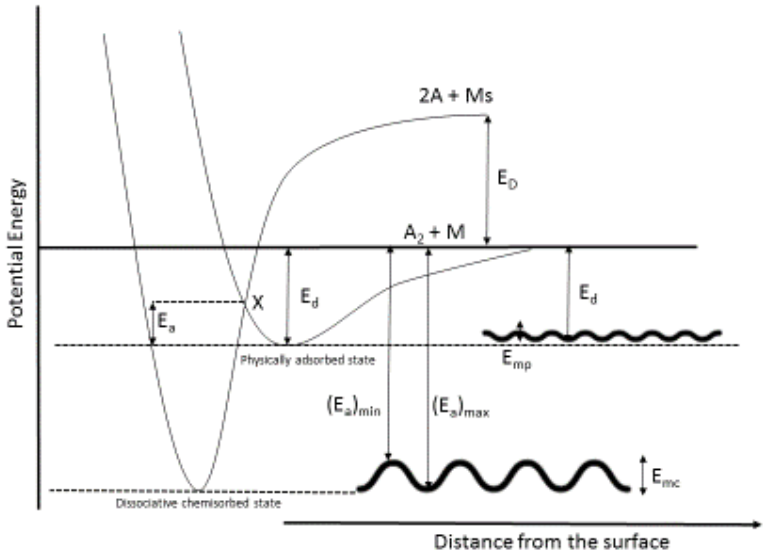


Figure 12 Potential energy diagram for the approach of a diatomic molecule $A_2$, surface M, $E_{mc}$ and $E_{mp}$ are activation energies for surface migration, $E_{mc}$ is the difference in maximum and minimum energies of adsorption, $E_D$ bond dissociation and $E_d$ desorption energy of $A_2$.[99]

### 1.11.5 Sticking probability (s)

In fact, it is safe to assume, that as molecules approach the surface, if met by a previously bound molecule they are more likely to remain in the gas phase. Molecules that do collide with the catalytic material on the other hand have a greater opportunity to stick. This sticking probability or sticking coefficient can be defined by the equation (1):

$$S = \frac{Rate\ of\ adsorption}{Rate\ of\ bombardment} \qquad (1)$$

One of the driving forces that governs the sticking probability is the crystal structure of the catalytic material. Certain crystallographic features demonstrate greater specificity than others. High symmetry planes such as face-centred cubic (fcc) and body-centred cubic (bcc) show increased affinity for binding. However, this rule is not set in stone and is very much dependant on external factors such as temperature and even previously adsorbed layers. Indeed, the more thermal energy that a system is subjected to causes greater mobility of atoms, thus the potential for miller indices to change.

### 1.11.6 Adsorptive energy

As previously discussed the attractive energies that drive physisorption and chemisorption are very different. But, as well as the ΔH of the reactions there are other energies that must be considered. These energies are vibrational, rotational, translational, kinetic energies and neighbouring species, they can be expressed in terms of heat loss as gas molecules adsorb on to the solid surface. These differential heats of adsorption ($q^{diff}$) are related to the interaction binding energies which vary as a function of adsorbed species with respect to the crystal. It also brings into consideration interactive energies with neighbouring pre-adsorbed molecules.

$$q^{diff} = \cup_0 - \left(aE^{vib} - aE_0^{vib}\right) - \Delta E^{tr} - \Delta E^{rot} + aP^{ia} \quad (eqn\ 2)$$

Where Uo is the interaction potential, ($aE^{vib} - aE_0^{vib}$) are vibrational energies $mol^{-1}$, $\Delta E^{tr}$ and $\Delta E^{rot}$ are the translational and rotational kinetic energy changes due to loss of degrees of freedom and finally $aP^{ia}$ is the neighbouring adsorbed species interactions and is dependent on the concentration of adsorbed species. This is an important equation as it communicates a number of varying concepts in relation to the differential heats of adsorption.

### 1.11.7 Binding energies

The energies play a crucial role in the structure of a bound species/molecule. Do smaller molecules, such as CO simply dissociate on contact with the catalytic surface and how do larger molecules bind? In what orientation? Consider Butane for example; does it orientate *via* either end or does it bond flat to the surface of the solid. The energy involved in binding is important as it enables an estimation of activation energy ($E_a$). In order to estimate binding energies consideration needs to be given to the sum of potential interactions.

$$\cup = \cup_d + \cup_r + \cup_p + \cup_{fd} + \cup_{fq} + \cup_{sp} \qquad (eqn\ 3)$$

$U_d$ is the potential attractive dispersion, $U_r$ close range repulsion term, $U_p$ is the energy necessary for polarisation. These first three terms are considered in every situation that impinges the fundamental law that drives all heterogeneous catalysis: Catalysis must always be preceded by

adsorption. The terms $U_{fd}$ and $U_{fq}$ are terms that express field dipole and gradient quadrupole interactions, as a result they are only considered when such surface interactions are occurring. The final term $U_{sp}$ relates to the self-potential for all adsorbate – adsorbate interactions and as such are not present at low level gas uptake by the catalytic material. For substrate materials, zeolites for example, all the terms must be considered. For simpler systems the Lennard-Jones equation is satisfactory.

$$U = \sum_i U(r_i) = \sum_i -\frac{A}{r_i^6} + \frac{B}{r_i^{12}} = 4\varepsilon \sum_i [(\frac{\sigma^{12}}{r_i}) - (\frac{\sigma^6}{r_i})] \qquad (eqn\ 4)$$

### 1.11.8 Lennard-Jones in relation to distance

When considering the Lennard-Jones equation in terms of distance, the constants A and B are polarizable ionisation potential energies, B is proportional to A as $4\varepsilon\ \sigma^6 = A$ and $4\varepsilon\ \sigma^{12} = B$ and ε is the interaction energy of the depth of the pore well, giving the equation:

$$U = [\sum_i -\frac{A}{r_i^6} + B\ exp^{(-\ Cr_i)}\ ] \qquad (eqn\ 5)$$

$r_i$ denotes the term that relates all interaction potential energies U to distance.

### 1.11.9 $CH_4$ activation and oxidation

$$CH_4 + O_{ads} \leftrightarrow CH_{3ads} + OH_{ads} \qquad (eqn\ 6)$$

$$CH_{3ads} + O_{ads} \leftrightarrow CH_{2ads} + OH_{ads} \qquad (eqn\ 7)$$

$$CH_{2ads} + O_{ads} \leftrightarrow CH_{ads} + H_{ads} \qquad (eqn\ 8)$$

$$CH_{ads} + O_{ads} \leftrightarrow C_{ads} + OH_{ads} \qquad (eqn\ 9)$$

$$OH_{ads} + M \rightarrow OH_{ads} + Sup \qquad (eqn\ 10)$$

$$C_{ads} + OH_{ads} \leftrightarrow CO_{ads} + H_{ads} \qquad (eqn\ 11)$$

$$CO_{ads} + O_{ads} \rightarrow CO_2 + M \qquad (eqn\ 12)$$

$$OH_{ads} + H_{ads} \rightarrow OH_2 + M \qquad (eqn\ 13)$$

### 1.11.10 CO oxidation

$$O_2(g) \leftrightarrow 2O_{ads} \qquad (eqn\ 14)$$

$$CO\ (g) \leftrightarrow\ CO_{ads} \qquad (eqn\ 15)$$

$$O_{ads} + CO_{ads} \leftrightarrow CO_{2ads} \qquad (eqn\ 16)$$

$$CO_{2ads} \leftrightarrow CO_2\ (g) \qquad (eqn\ 17)$$

## 1.12 Unbalanced magnetron sputtering (UBMS)

Magnetron sputtering is a method of coating that falls under the banner of physical vapour deposition (PVD). Over the last 30 years there have been a number of advances in this field and today it is the standard method for industrial coated substrates.[100] Sputter coated substrates in many cases out-perform other PVD processes, thus this process is now the standard for low friction coatings, wear-resistance, decorative and substrates that require specific optical or electrical properties.[101] There have been a number of important advances in the technique, in the 1970s the introduction of a balanced or conventional magnetron.[102] Then in the 1980s the unbalanced system and finally and possibly most significantly the addition of a closed field.[103] These systems are easier to explain with the use of diagrams, however the introduction of the close field unbalanced magnetron (CFUBM) has effectively increased the plasma volume, maintained a substrate bias and increased the substrate current. Consequently this has reduced the temperatures required, reduced the pressures needed and increased more control to the user, giving more scope and better quality coatings.[104]

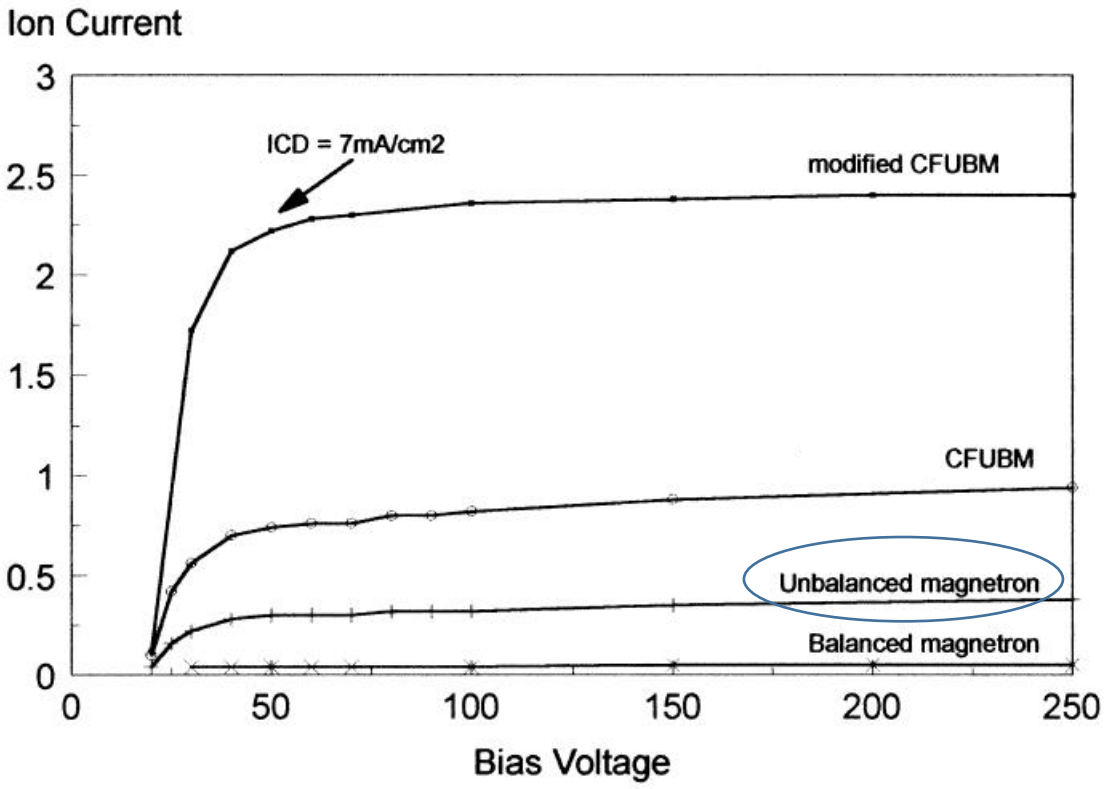


Figure 13 Chart showing substrate bias vs current for different systems[105]

Figure 13 demonstrates how the CFUBM increases the current at low bias voltage, therefore the rate of deposition is greatly improved. The basic principal behind this method of PVD is the use of a cathode or target plate which is bombarded by ions *via* the generation of a glow discharge plasma. The bombardment of ions removes atoms from the target surface and these atoms coat the substrate. A conventional or balanced magnetron is hindered by the short field plasma discharge from the target. This can cause poor deposition onto the substrate, increasing the substrate bias/voltage might improve this slightly, however, there may be problems with the uniformity of the coating. In an ideal system the plasma should reach the substrate and ion current density should be between 2-10 mA/cm$^2$ as depicted in figure 14.[106] This is achieved by making the outer magnet, the North ring magnet stronger than the central South-pole magnet, forcing the lines of force further toward the substrate, thus increasing plasma volume and ion density.

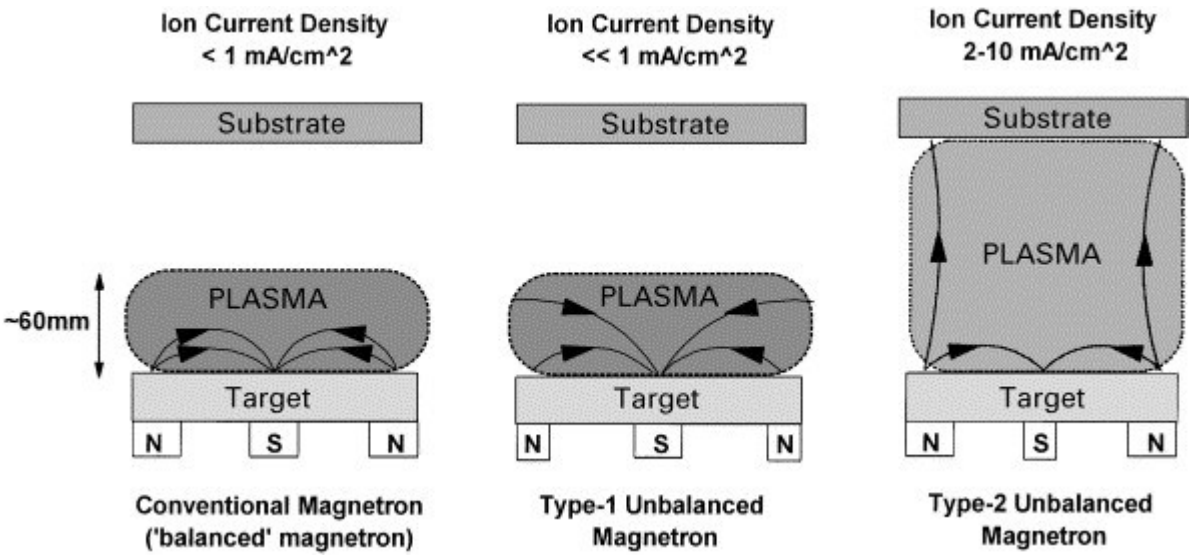


Figure 14 Plasma field observed in balanced and types I and II unbalanced systems[107]

# 2. Aims & Objectives

## 2.1 Aims

To design and develop catalysts to oxidise CO and $CH_4$ at low temperatures. To ensure that the catalysts prepared are stable at temperatures similar to those found in catalytic convertors and continue to give 100% conversion.

## 2.2 Objectives

- Develop a wet chemical synthetic method that fully disperses precious metal loading over substrates
- Reduce the temperature at which complete combustion of CO and $CH_4$ is achieved
- Characterise materials utilising XRD, BET, TEM and SEM
- Test all catalytic materials for activity
- Develop a magnetron coating regime and to validate *via* catalytic testing
- Prepare zeolites using colloidal silica extracted from geothermal fluid

## 3. Catalyst Preparation

**Table 2 List of Chemicals, Supplier and Purity**

| Reagent | Supplier | Purity % | Lot # |
|---|---|---|---|
| **$CaCl_2$** | Fischer Scientific | > 96.0% | 012775 |
| **$KH_2PO_4$** | Sigma Aldrich | > 99.5% | SLBN1039V |
| **$NH_4OH.2H_2O$** | Honeywell | ~ 30% | SZBG2180 |
| **$HAu(III)Cl_4.3H_2O$** | Sigma Aldrich | > 99.9% | MKGB6147V |
| **$Co(II)Cl_2$** | Sigma Aldrich | > 98.0% | BCBG0246V |
| **$Pd(NO_3)_2.2H_2O$** | Sigma Aldrich | ~ 40% | BCBL1372V |
| **$Rh_2(CH_3COO_4)$** | Sigma Aldrich | 99% | MKBX7404V |
| **$Pt(IV)Cl_4.H_2O$** | Alfa | 99.99% | K28Y042 |
| **FAU Zeolite Y** | ZEOLYST | - | 720044004218 |
| **$Al_2O_3$** | Sigma Aldrich | - | BCBT5742 |
| **$TiO_2$** | Millennium | - | 6293000234 |
| **$CeO_2$** | Sigma Aldrich | - | MKBQ7525V |

### 3.1 Methods

#### 3.1.1 HAp

$CaCl_2$ was placed into a beaker with 100 ml of deionised water and stirred for 1 hour using a magnetic stirrer and bar. $KH_2PO_4$ was placed into a separate beaker and stirred for one hour. The solutions were then pH adjusted with $NH_4OH$ to pH 10.00 ± 0.05 using a Metler Toledo pH meter. The $CaCl_2$ solution was then addded dropwise over one hour to the $KH_2PO_4$ solution whilst stirring, forming a white precipitate: 10 $CaCl_2$ + 6 $KH_2PO_4$ + 2 $H_2O$ → $Ca_{10}(PO_4)_6(OH)_2$ + 6 KCl + 14 HCl. The solution was then placed into a PTFE lined stainless steel autoclave and heated to 180 ˚C for 72 hours. Stirred for 18 hours at room temperature. Or 2 hours also at room temperature. The resulting slurries were filtered and washed 5 times with deionised water, dried in an oven at 65 ˚C before finally being calcined in air in the furnace at 550 ˚C for 5 hours.

**Table 3 HAp Designation Depending on Synthesis**

| Time (hours) | Carbon (Y/N) | Autoclaved (Y/N) | Designation |
|---|---|---|---|
| 72 | **Y** | **Y** | **HApC(Auto72)$^{(C\ mass\ g)}$** |
| 18 | **Y** | **N** | **HApC(18h)$^{(C\ mass\ g)}$** |
| 2 | **Y** | **N** | **HApC(2h)$^{(C\ mass\ g)}$** |

### 3.1.2 Zeolites prepared using geothermal silica

The FAU-type zeolites were prepared from a synthesis solution with the following molar composition: $8.6Na_2O : 1.0Al_2O_3 : 16.7SiO_2 : 435H_2O$. 4.90 g of NaOH were mixed with distilled (D.I) water in a beaker and stirred for 10 min followed by the addition of 1.20 g of $NaAlO_2$, and, after additional stirring for 5 min, 20 g of colloidal silica was added. The mixture was stirred for 1 h and transferred to a polypropylene reactor. The mixture was aged at 30 °C for 20 h and then hydrothermally treated at 90 °C for 24 h. After the synthesis, the zeolites were purified by three-times centrifugation and redispersion in D.I water and dried at 90 °C overnight. The zeolites prepared with the two colloidal silica sources were labelled as Na-FAU (Geo-12) and Na-FAU (Ludox), respectively. Samples were also prepared, in which the as-made zeolites were partially converted into an $H^+$ form. For these experiments, 1 g of corresponding Na-zeolites was mixed with 100 g of 0.05 M $NH_4Cl$ solution in a beaker and stirred for 24 h. The zeolites were then purified by four times centrifugation and redispersion in D.I water, dried at 90 °C overnight, ground in a mortar, and calcined at 550 °C for 4 h using a heating rate 10 $min^{-1}$. These samples were labelled as H-FAU (Geo-12) and H-FAU (Ludox), correspondingly.

Pd-loaded zeolite samples were prepared as follows: 0.02 M Pd solutions were prepared in 25 ml volumetric flasks; the pH of the solutions was adjusted with ammonium hydroxide to a pH range of 10-12. The Pd solutions were added to 0.8 g of zeolite samples in beakers, sonicated in an

ultrasonic bath for 45 min and then stirred overnight. The samples were recovered by filtration, washed with copious amounts of D.I water, dried and calcined at 550 °C for 4 h. Corresponding samples were labelled as Na-FAU-Pd (Geo-12), Na-FAU-Pd (Ludox), H-FAU-Pd (Geo-12) and H-FAU-Pd (Ludox).

### 3.2 Pd and Au catalysts

Solutions of 0.02-0.05 M $HAu(III)Cl_4.3H_2O$ were prepared in volumetric flasks filled to the bottom of the neck with deionised water, and sonicated in an ultrasonic bath (XUBA3 50-60 Hz) for 45 minutes, after which they were allowed to equilibrate, then made up to volume. Solutions of 5-6 mM $Pd(II)(NO_3)_2.2H_2O$ were pH adjusted with ammonium hydroxide to a pH range of 10-12 and otherwise prepared using an identical procedure to that for Au.

Catalysts containing Pd and Au were prepared by adding desired concentrations of precious metal salts to HAp, $Al_2O_3$, $TiO_2$, HY-Zeo and/or $CeO_2$ supports in a beaker and sonicated for 45 minutes. After sonication they were left to stir at room temperature overnight, then filtered, washed with copious amounts of deionised water, dried for 3 hours at 60 °C and calcined at 550 °C for 4 hours using a ramp rate of 5 °C/min.

### 3.3 Pd, Pt and Rh catalysts

0.008 M, 0.005 M and 0.005 M solutions of Pd, Pt and Rh were made by first weighing $Pd(NO_3)_2$, $PtCl_4$ and $Rh_2(CH_3COO)_4$ into separate 25 ml volumetric flasks. This was repeated 15 times. 2 ml of ammonia was added and the volumetric flasks were then filled to the neck with deionised water and. After the salts had been shaken vigorously they were sonicated for 30 minutes, then allowed to equilibrate before being made to volume.

A total of 2.0 g of $Al_2O_3$, $TiO_2$, or HY-Zeo support, or an equal mass mixture of supports, and for certain preparations an additional 0.2 g $CeO_2$, was placed into a beaker with a magnetic stirrer, and the three metal solutions were added in the order of Rh, Pd and Pt. The slurry was then stirred for 30 minutes, sonicated for 45 minutes, then stirred overnight. The following the

day, the slurry was sonicated for a further 15 minutes, before being filtered, washed with copious amounts of water, then dried and calcined at 550 °C for 4 hours using a ramp rate of 5 °C/min. Samples were labelled using the terminology *support-Pd/Pt/Rh* e.g. $TiO_2/Al_2O_3/CeO_2$-Pd/Pt/Rh comprised 1.0 g $TiO_2$, 1.0 g $Al_2O_3$ and 0.2 g $CeO_2$.

### 3.4 Magnetron sputtered catalysts

Magnetron sputtering was used to add Pd to Au catalysts that were prepared as follows.

#### 3.4.1 Au Catalysts

Solutions of 0.002 M $HAu(III)Cl_4.3H_2O$ were prepared in 25 ml volumetric flasks filled to the neck with deionised water, shaken vigorously and sonicated in an ultrasonic bath (XUBA3 50-60 Hz) for 30 minutes. After the solution was allowed to equilibrate it was then made to volume with water. The entire contents were added to 5.0 g of $Al_2O_3$, $TiO_2$, or HY-Zeo support, and for certain preparations an additional 0.05 g $CeO_2$, was placed into a beaker and stirred for 60 minutes, sonicated for 45 minutes, then stirred overnight. The solid was removed by filtration, washed with copious amounts of water, then dried and calcined at 550 °C for 4 hours using a ramp rate of 5 °C/min.

#### 3.4.2 Pd Deposition

2.0 g of $Al_2O_3$, $TiO_2$, or HY-Zeo support, or Au catalyst as prepared in section 3.4.1, was placed onto a SignalForce™ Data Physics shaker inside an in-house built magnetron sputtering vacuum chamber, in which a single 75 mm diameter unbalanced magnetron was installed in the chamber roof in the 'sputter down' configuration. The shaker, positioned directly underneath the magnetron at a separation of 8 cm, was adjusted in terms of oscillation frequency and amplitude to optimise the movement of the powder supports within a 10 cm dimeter dish attached to the shaker. The chamber was sealed and the pressure was reduced to a base pressure of $< 4.0 \times 10^{-3}$ Pa using a Leybold 250 turbo pump and Edwards 28 rotary pump. Once the desired base pressure was reached, the chamber was backfilled with argon at a flow rate of 10 ml $min^{-1}$ to maintain an operating pressure of 0.5 Pa. The target was sputtering in pulsed DC mode at 100 W and 100 kHz

pulse frequency (60% duty) using an Advanced Energy DC Pinnacle Plus™ power supply. The Data Physics shaker was then switched on and separate batches of support materials were then sputtered coated with Pd for durations of 10, 15 and 20 minutes. Following deposition, the target was allowed to cool for 15 minutes before venting and removal of the coated powder. Samples were labelled using the terminology *Pd/Au catalyst/support [MAG sputter time in mins]* e.g. Pd-Au-$TiO_2$ [15 MAG] is Pd sputtered on Au-$TiO_2$ for 15 minutes.

# 4. Characterisation Techniques

## 4.1 X-Ray diffraction

X-ray powder diffraction (XRD) data was collected on a PANalytical X'Pert powder diffractometer using a Cu anode (Cu $k\alpha_1$ $\lambda$= 1.540598Å) fitted with a PIXcel 1D detector operating in scanning line detector mode. Samples measured in reflection geometry in the range 5 - 100° 2θ with a step size of 0.01° 2θ, a sweep time of 0.033°/s and an overall scan time of 49 minutes.

### 4.1.1 XRD theory

In a crystalline structure, molecules position themselves to maximise the number of attractive intermolecular interactions and minimise the number of repulsive interactions. The crystal structure describes the type and arrangement of ions, atoms or molecules in a crystal. The crystal structure is therefore defined by its unit cell. The unit cell is the smallest "box" that the crystal can be broken down into that can rebuild the crystal through simple translation:

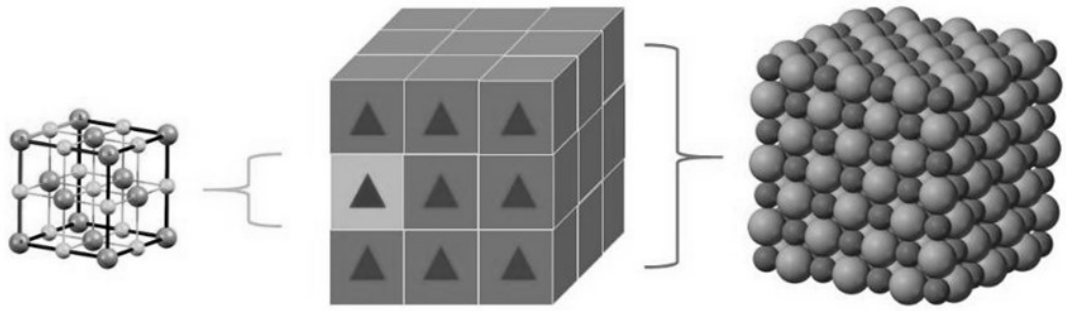

Figure 15 Crystal Structure[108]

The shape of the unit cell is described by three axis lengths (*a, b, c*) and three angles (α, β, γ) with the arrangement of the different atoms, ions or molecules inside described by one of 230 possible *space groups*. Theoretical planes called lattice planes are drawn through the unit cells. As all the atoms' positions on the lattice plane in one unit cell are identical to those in all the others the distances between these planes are used to describe repeat distances. Each lattice plane is labelled with a set of Miller Indices that describe where in the unit cell the plane is located. These are labelled (*h*, *k*, *l)* and are given numbers to show the point at which they intersect each axis (a/h, b/k, c/l). For example, a plane intersecting the *a* and *b* axes half way up the unit cell (so a/2, b/2) and not intersecting the *c* axis at all (c/0) is the (2,2,0) plane.

### 4.1.2 Diffraction

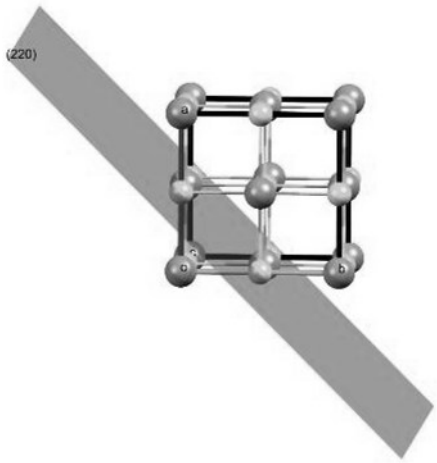


Figure 16 Plane Intersecting Crystal Structure[109]

The scattering of electromagnetic radiation by physical objects causes diffraction. To produce significant diffraction, the spacing between the objects and the wavelength of the electromagnetic wave should be similar in size. X-rays are used to produce the diffraction pattern for crystals, as their wavelength λ is typically the same order of magnitude (0.1–10 nanometres) as the spacing *d* between lattice planes in the crystal. X-rays are scattered by the atoms' electrons and the degree of scattering is proportionate to the number of electrons present, therefore the heavier the atom the more intense the diffraction. An X-ray striking an electron produces secondary spherical

waves emanating from the electron. As crystals are a regular array of objects, they produce a regular array of spherical waves. Although these waves cancel one another out in most directions through destructive interference, they add constructively in a few specific directions, determined by Bragg's law. Bragg's law treats the diffracted beams as if they are simple reflections: the X-rays bounce off the planes at the same angle as they hit it.

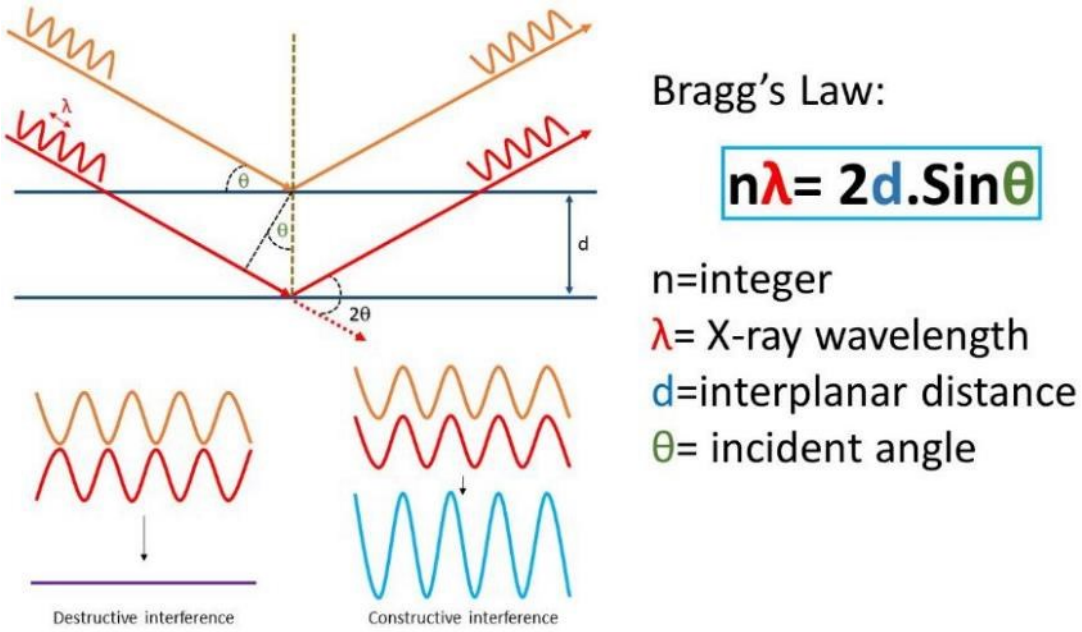


Figure 17 Bragg's Law[110]

In geometric terms, if the path difference (the difference in distance travelled) between an X-ray at angle θ reflecting off of a plane and the distance travelled by an X-rays hitting the planes "above" and "below" it are an integer number of wavelengths. The waves are in phase and interfere constructively (add together) to give a reflection.

The wavelength of the radiation and the angles at which reflections are seen can be used to calculate the distances for all the interplanar spacing in the crystal.

### 4.2 BET $N_2$ adsorption porosimetry

The $N_2$ adsorption analysis was conducted on a Micrometrics ASAP 2020 instrument at 77 K. Preparation of the samples for degassing was done at 300° C under vacuum ($p < 10^{-3}$) for 3 hours prior to analysis under nitrogen flow. The surface area and isotherms were analysed using standard BET procedure at a pressure range of 0.05-0.30. The surface properties of the samples were undertaken by $N_2$ adsorption - desorption analysis. This provided data on the surface area, pore size and type IV isotherms, proving that the materials prepared are mesoporous materials.

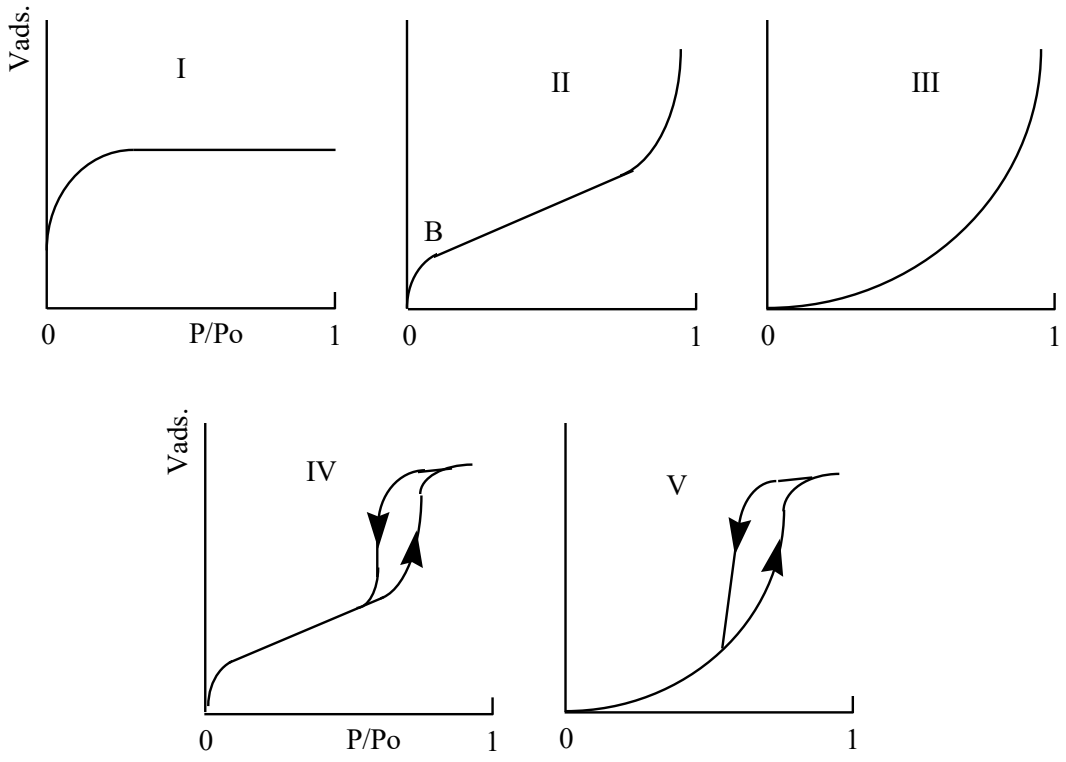


Figure 18 Nitrogen Adsorption Isotherms[111]

#### 4.2.1 BET theory

$N_2$ adsorption is measured by varying the pressure of $N_2$ at 77 K while keeping the system isothermal. Five types of isotherm describe the adsorption of gases on to a surface. Type I isotherms define a single or monolayer adsorption, Type II and III represent multi-layer physical adsorption. Type IV and V are analogous to type II and III isotherms and occur on adsorbents in the region of 2-

100 nm. As the pressure increases, graphical data shows an increase in adsorbate as the pores fill, once the pores are filled adsorption rate decreases.

### 4.2.2 Adsorption

Gaseous compounds adsorb on to the surface of a material *via* chemical or physical adsorption (chemisorption or physisorption) respectively. Chemisorption describes actual chemical bonds forming between the adsorbate and the material, where physisorption describes weak Van der Waals (VDW) interactions between the adsorbate and the surface of the material.

### 4.2.3 BET

To determine surface area of a material the Brunauer-Emmett-Teller (BET) theory is used to determine specific surface area of a material. The BET equation breaks down to give us a straight-line plot (equation 1)

$$\frac{1}{W\left(\left(\frac{P^\circ}{P}\right)-1\right)} = \frac{1}{W_m\, C} + \frac{C-1}{W_m\, C} - \left(\frac{P}{P^\circ}\right) \quad (19)$$

Where W = the weight of gas adsorbed, $\left(\frac{P}{P^\circ}\right)$ = relative pressure, $W_m$ = weight of monolayer adsorbed and C = BET constant. For a straight line plot: $1/W((P/P^\circ)-1)$ against $P/P^\circ$. Total surface area can then be determined from first calculating $W_m$ which is equal to 1/slope + intercept. From there $n_m$ (molar monolayer coverage) = $W_m/W_n$, where $W_n$ is a constant and equal to 0.0224, therefore, surface area = $N_A$ x 0.162 nm x $n_m$ where $N_A = 6.023 \times 10^{23}\ mol^{-1}$.

**4.3 SEM Theory**

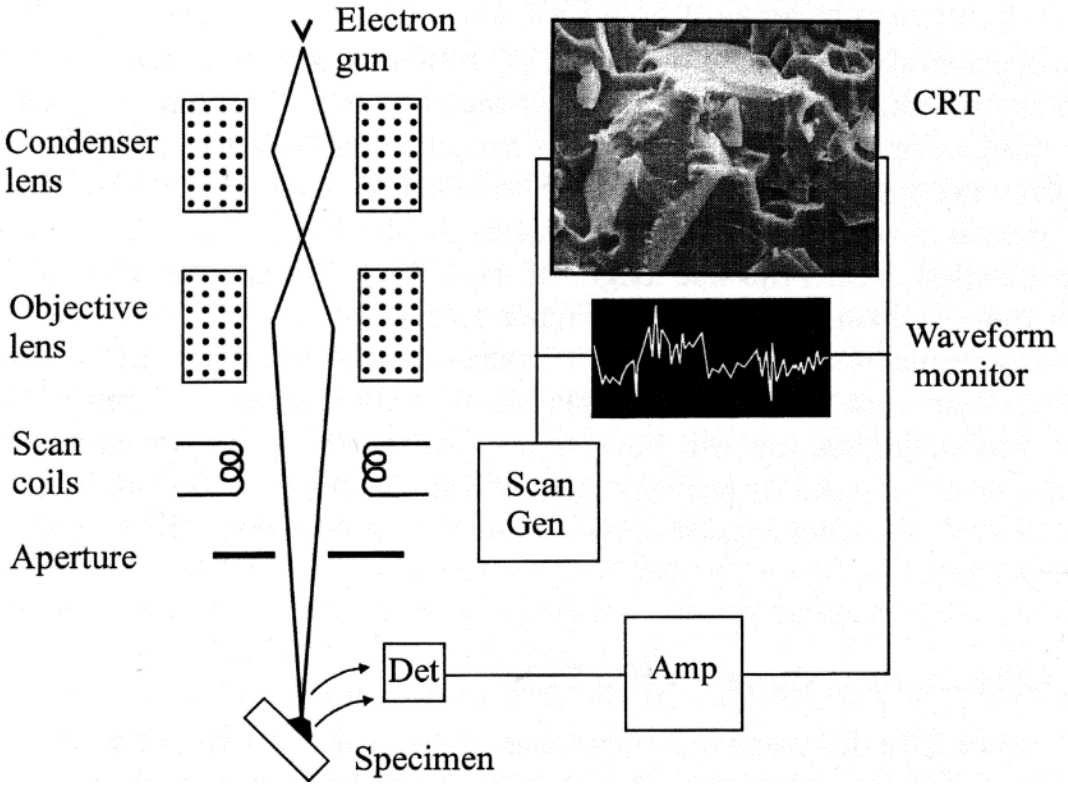


Figure 19 Illustration of the Basic Components of SEM[112]

SEM enables us to view images at the surface of a sample, this is accomplished by scanning a thin beam of electrons over the surface of the sample of interest and recording the signal that is emitted. The resolution of most modern SEM is in the order of 2 nm compared to the 1 µm for a standard optical microscope. Analysis has to attained under vacuum, as electrons do not pass through air. Figure 19 illustrates the fundamental parts of an SEM. Electrons emitted by the gun are accelerated by ~ 20 kV, the electrons then pass through a condenser and an objective lens and scan coils before passing through an aperture and hitting the sample. Simultaneously a scan is generated on a computer monitor. The electrons emitted by the sample are then amplified, detected, and an image is generated. When high-energy electrons strike the sample a number of signals are generated, backscattered and secondary electrons and X-rays. Back-scattered electrons originate from deeper in the sample, they offer data on the composition of the sample, however they generally give poorly resolved images. Secondary electrons originate from the surface of the materials of interest, therefore, give us topographical information about the sample. X-rays give us

the elemental composition of the sample. The secondary electron detector emits photons when struck by high-energy electrons; the emitted photons are collected by a light-guide and transported to the photomultiplier for detection.

### 4.3.1 Volume and surface interaction

To acquire an image in the SEM, there must be discrepancy in the signal from different parts of the sample. The yield of secondary electrons is at a minimum when the surface of the sample is at right angles to the electron beam. This is due to the shape of the contact volume and its relationship to the surface of the sample. In areas of the sample that are not perpendicular to the beam, electrons are more commonly scattered out of the sample, rather than further into the sample. This tends to make some areas of the image appear brighter.

### 4.3.2 Backscattered and secondary electrons

Backscattered electrons are detected using a negative potential to repel the secondary electrons, however, collection efficiency tends to be low. Backscattered electrons are strongly scattered back in the direction of the incident beam therefore, the detector for these electrons is positioned near the final lens. Backscattered electron detectors are usually solid-state devices. The electrons that strike the detector produce electron-hole pairs, which produce a current that is then amplified.

## 4.4 TEM Theory

Transmission electron microscopy is a prevailing tool, especially when executed in the materials and coatings industries. A high-energy beam of electrons is directed through a very thin sample, and the interactions between the electrons and the atoms can be used to observe features such as the crystal structure and features in the structure like dislocations and grain boundaries. It is also possible to use TEM for chemical analysis. TEM can be used to study the evolution of layers, their composition and defects. High resolution can be used to analyse the quality, shape, size and density of quantum wells, wires and dots.

The TEM operates on the same basic principles as the light microscope but uses electrons instead of light. Because the wavelength of electrons is much smaller than that of light, the optimal resolution attainable for TEM images is many orders of magnitude better than that from a light microscope. Thus, TEMs can reveal the finest details of internal structure - in some cases as small as individual atoms.

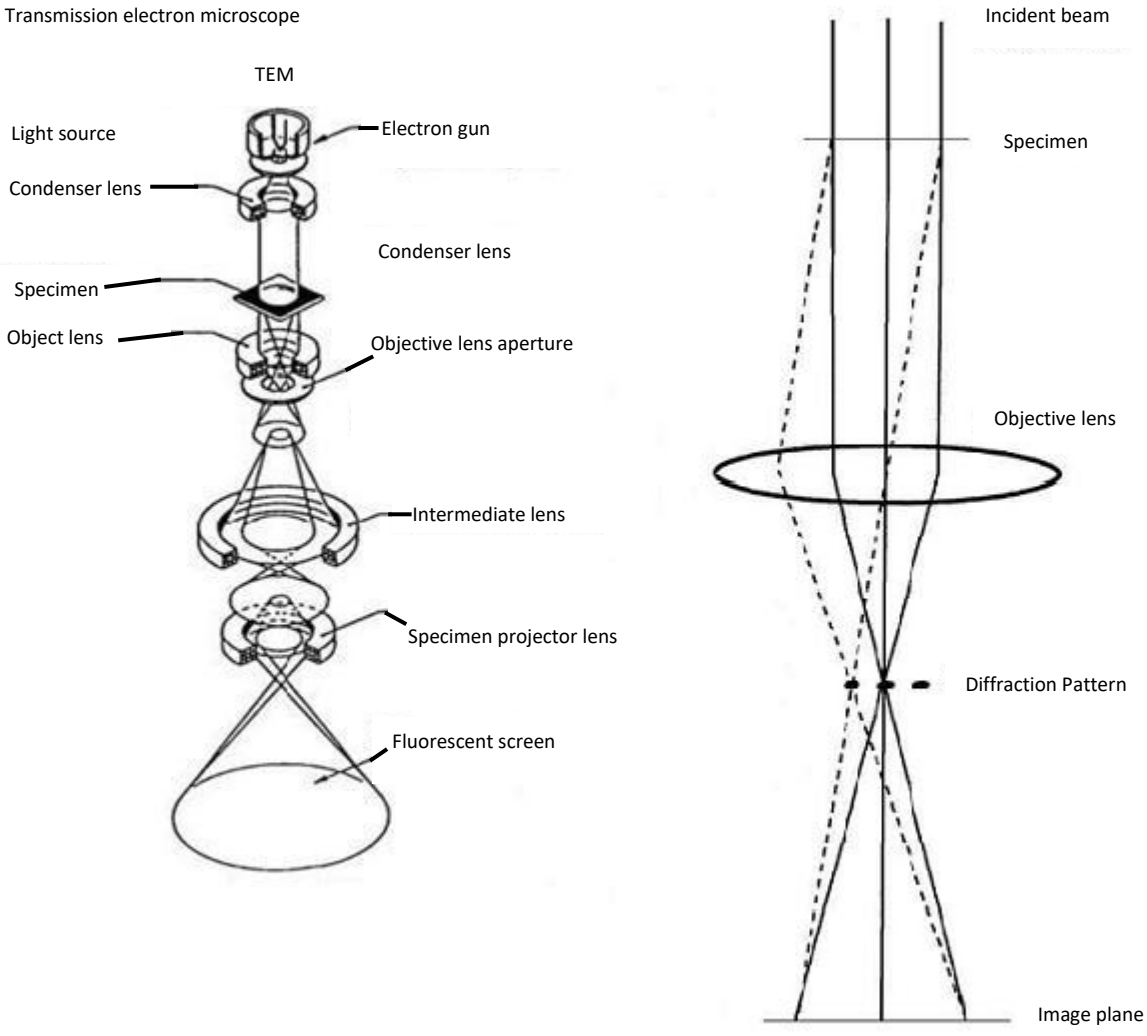


Figures 20 TEM Schematic and electron diffraction pattern[113]

### 4.4.1 Imaging

The beam of electrons from the electron gun is focused into a small, thin, coherent beam by the use of the condenser lens. This beam is restricted by the condenser aperture, which excludes high angle electrons. The beam then strikes the specimen and parts of it are transmitted

depending upon the thickness and electron transparency of the specimen. This transmitted portion is focused by the objective lens into an image on phosphor screen or charge coupled device (CCD) camera. Optional objective apertures can be used to enhance the contrast by blocking out high-angle diffracted electrons. The image then passed down the column through the intermediate and projector lenses, is enlarged all the way.

The image strikes the phosphor screen and light is generated, allowing the user to see the image. The darker areas of the image represent those areas of the sample that fewer electrons are transmitted through while the lighter areas of the image represent those areas of the sample where more electrons were transmitted.

### 4.4.2 Diffraction

Figure 20 shows a simple sketch of the path of a beam of electrons in a TEM from just above the specimen and down the column to the phosphor screen. As the electrons pass through the sample, they are scattered by the electrostatic potential set up by the constituent elements in the specimen. After passing through the specimen they pass through the electromagnetic objective lens which focuses all the electrons scattered from one point of the specimen into one point in the image plane. Also, shown in figure 20 is a dotted line where the electrons scattered in the same direction by the sample are collected into a single point. This is the back focal plane of the objective lens and is where the diffraction pattern is formed.

### 4.5 Catalytic testing

Total flow during analysis was kept at 50 mL/min, CO 10 mL/min, $O_2$ 10 mL/min and He 30 mL/min, $CH_4$ 5 mL/min, $O_2$ 10 mL/min and He 35 mL/min. Gas flow was controlled *via* Bronkhorst F-201DV and F-201CV mass flow controllers. The GC was tested for stability of analysis prior to each run through the bypass by injecting $O_2$, CO, $CH_4$ and $CO_2$ to ascertain where the peaks would elute in the chromatograph. Once stability was assured, He was flown through the rig and injections were

taken until no peaks were seen. The system was then switched to the reactor and CO or $CH_4$ and $O_2$ were passed through the reactor for 5 minutes before analysis was started.

### 4.5.1 Catalytic tests all samples

The catalyst activity of each sample was studied in a quartz fixed bed reactor, shown in Figure 21, placed inside a temperature controlled furnace (Carbolite type 3216, Tempatron, PID500/110/330). 0.2 g of catalyst was placed in a quartz tube (10 mm diameter, 1 mm thickness) between quartz wool plugs. A feed mixture of 50 ml $min^{-1}$ comprising $CH_4$:$O_2$:He equal to 5:10:35 was used in all catalytic tests. Gases were supplied from lecture bottles (CKGAS filled to 200 Bar at 15 °C) and regulated using single stage CONCOA 302 series gas regulators. The flow of each gas was maintained using Bronkhorst UK model F-201CV mass flow controllers.

The reaction products were monitored by a Hewlett Packard 5890 series II gas chromatograph equipped with a Carboxen 1010 plot fused silica capillary column (30 m x 0.53 mm) connected *via* a 6-way gas sampling valve to a thermal conductivity detector. Measurements were recorded at 25 °C intervals (after holding at that temperature for 5 mins) starting at 75 °C using a heating rate of 10 °C $min^{-1}$.

In order to progress the project and enable greater future work, having successfully built the catalyst testing rig for oxidation reactions, the decision was made to build a second more advanced version. The PFD figure 22 clearly demonstrates the advancements made and the capabilities that the new rig offers. With the arrival of the new GC fitted with an FID, TCD and MS, the use of more gases and actuator valves, not only can it perform characterisation, but also closer simulate conditions found in a compression combustion engine.

Design and engineering of the MKII fixed bed reactor commenced with a scale version of the rig being planned and mapped out in the laboratory. With an increase from 12 to 28 valves the complexity of the new rig was considerably more advanced. At a cost of over ¼ million GBP, this was by far the most extensive project undertaken during the doctoral studies.

A benchtop frame built to accommodate the mass flow controllers (MFC), the furnace and the GC. The frame was sealed with Perspex and extraction was added to ensure a safe working environment. 16 MFC were secured to a stainless steel sheet and gas supplied, either *via* piped in from a fixed external source or through a separate sealed box under the lab bench. The separate sealed box consisted of four different gases and regulators. The box was secured under the bench and pipe work was taken up through purpose drilled holes to the MFC. A second stainless steel sheet was drilled and cut to house 28 valves, a pressure meter and four digital thermometers. The MFC and the valves were then connected using ¼ inch stainless tubing. Gas supplied to all valves and MFC and the system was leak tested. The tubing was wrapped in heating tape controlled by the digital thermometers to remove the risk of gas condensing on route to the GC.

A purpose built catalyst housing was devised to house 3D printed support materials to be wash coated with catalyst. The catalyst housing was attached to a removable gas supply so that it could easily be placed inside the furnace and catalysts changed as required.

The furnace itself was fixed to a rotating turntable so that it could be accessed easily. ¼ inch tubing was fitted to bypass the furnace if required, this allowed gas to run straight to the GC for characterisation.

The ability to switch between lean and rich[114] fuel mixtures enables the catalyst testing rig to closer match the conditions in a combustion engine. With the added capability to run $CH_4$ and a substitute liquid fuel over the catalytic materials, a more real world solution to the problem associated with burning fossil fuels could potentially be discovered. This would substantially reduce the gap associated with lab testing and transferring to vehicle application. The GC was fitted with a TCD, FID and MS. The extra functionality would enable the new system to perform more complex testing, including temperature programmed reduction and the ability to extend research to looking at nitrogen oxides.

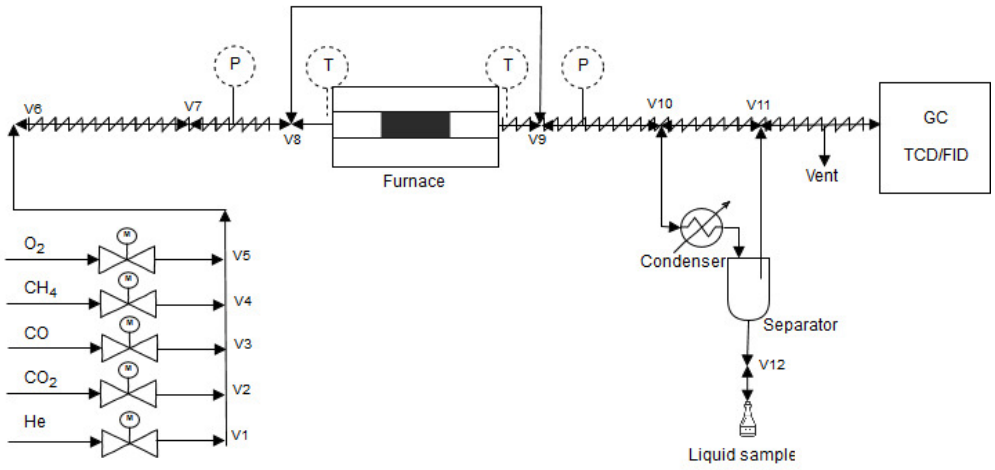


Figure 21 PFD of catalyst testing rig

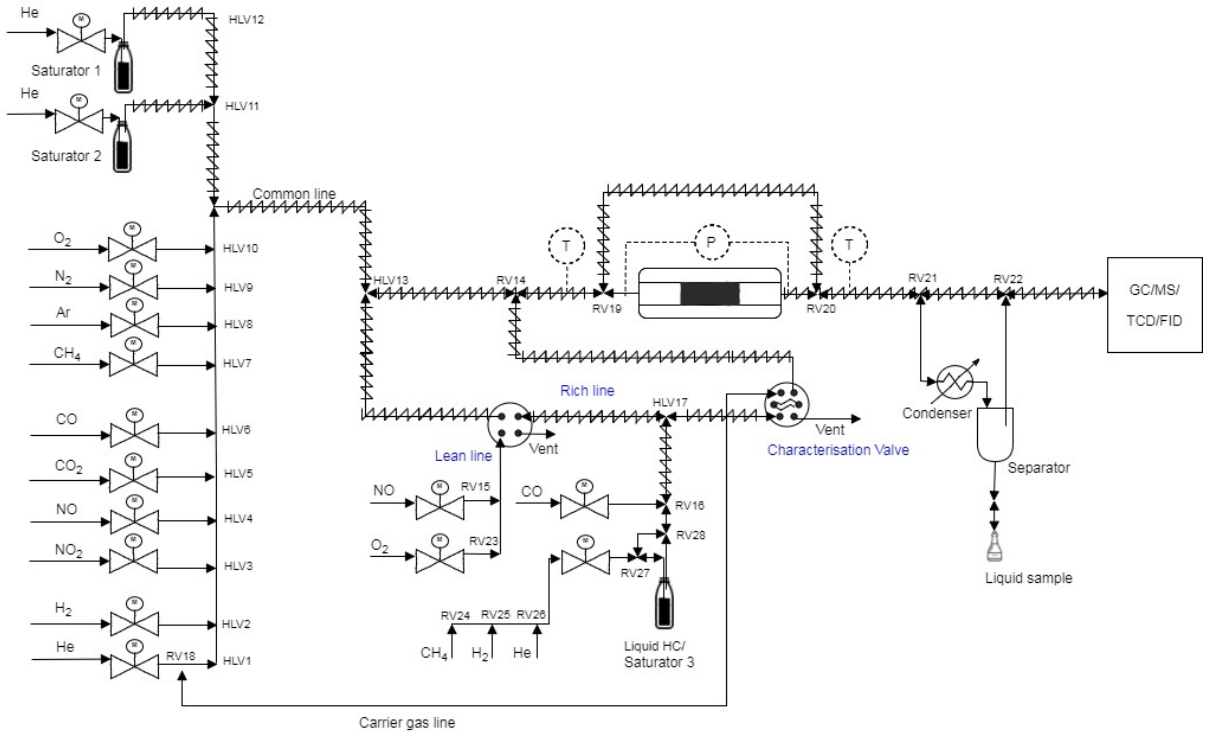


Figure 22 PFD of Catalyst Testing Rig MKII

### 4.6 Calibration

Tables 3-5 show the graphical representation for the amount % of gas flow sent to the GC and the corresponding response factor for CO, $CO_2$ and $CH_4$ respectively. The calibration curves were constructed by injecting known flow rates through the GC and measuring the response (peak area). The regression line was taken from the plotted points and a correlation coefficient $R^2$ gives an indication of how closely the points fit a straight line.

**Table 3 Calibration data for CO catalytic testing**

| % CO | Flow Rate CO ml/min | % | Flow Rate He ml/min | % | Total Flow ml/min | CO Area mV/s |
|---|---|---|---|---|---|---|
| **30** | 15 | 7.5 | 35 | 12.3 | 50 | 801324.9<br>795458.6 |
| **20** | 10 | 5.0 | 40 | 14.0 | 50 | 547995.3<br>549722.6 |
| **16** | 8 | 4.0 | 42 | 14.7 | 50 | 444255.4<br>445966.2 |
| **10** | 5 | 2.5 | 45 | 15.8 | 50 | 305267.5<br>305006.5 |

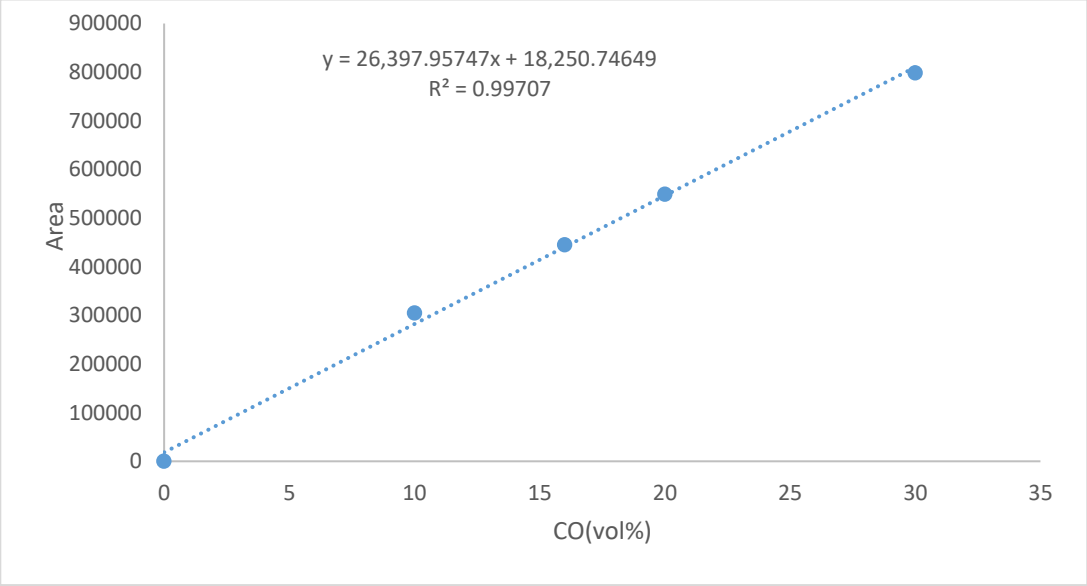


Figure 23 Calibration Graph for CO (response recorded at 15, 10, 8, 5 and 0 mL/min)

**Table 4 Calibration Data for $CO_2$ Catalytic Testing**

| % $CO_2$ | Flow Rate $CO_2$ mL/min | Flow Rate He mL/min | % | Total Flow mL/min | $CO_2$ Area mV/s |
|---|---|---|---|---|---|
| **30** | 15 | 35 | 12.3 | 50 | 807216.8 |
| **20** | 10 | 40 | 14.0 | 50 | 509924.6 |
| **16** | 8 | 42 | 14.7 | 50 | 405008.2 |
| **10** | 5 | 45 | 15.8 | 50 | 243645.0 |

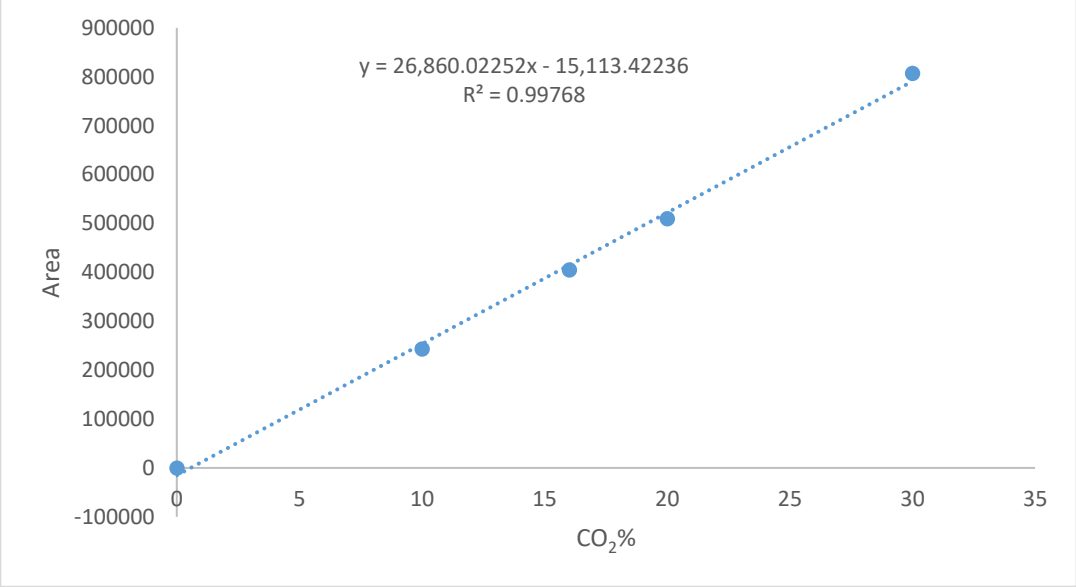


Figure 24 Calibration Graph for $CO_2$ (response recorded at 15, 10, 8, 5 and 0 mL/min)

**Table 5 Calibration Data for $CH_4$ Catalytic Testing**

| % $CH_4$ | Flow Rate $CH_4$ mL/min | % | Flow Rate He mL/min | % | Total Flow mL/min | $CH_4$ Area mV/s |
|---|---|---|---|---|---|---|
| **30** | 15 | 15 | 35 | 12.3 | 50 | 520367.6<br>528607.5 |
| **20** | 10 | 10 | 40 | 14.0 | 50 | 326657.8<br>318268.3 |
| **16** | 8 | 8 | 42 | 14.7 | 50 | 245164.0<br>245576.2 |
| **10** | 5 | 5 | 45 | 15.8 | 50 | 131177.9<br>130663.3 |

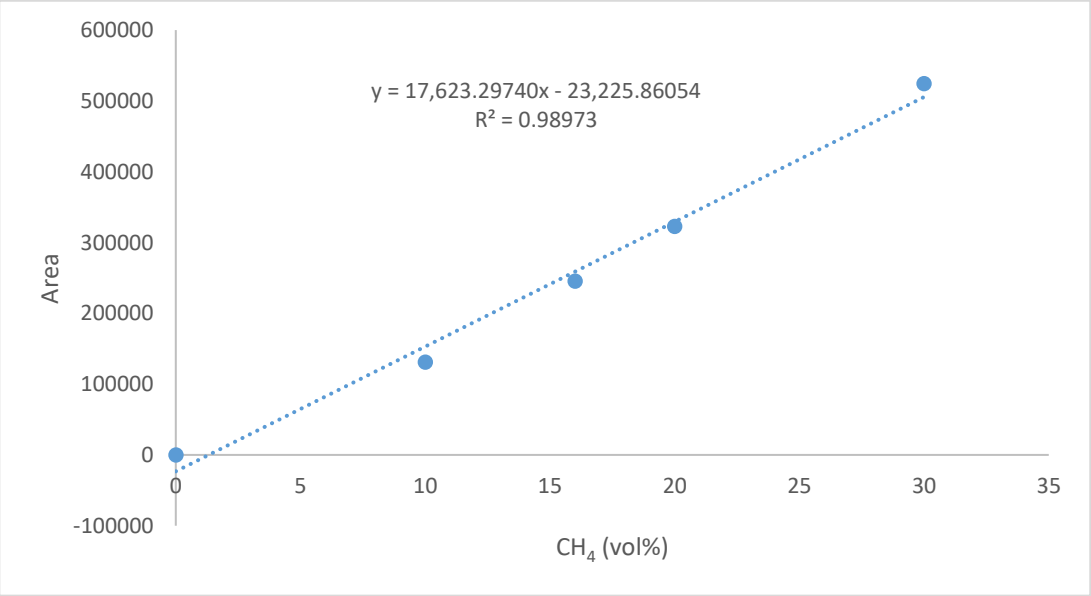


Figure 25 Calibration Graph for $CH_4$ (response recorded at 15, 10, 8, 5 and 0 mL/min)

# 5. Results and Discussion

## 5.1 HAp

### 5.1.1 XRD and XRF Analysis for HAp samples

The HAp samples were characterised using XRD in order to investigate the effects the of preparation time. Figure 26 shows there is a general increase of crystallinity with preparation time. The samples autoclaved, have the highest crystalline structure, followed by the samples which stirred for 18 hours and finally the samples which were only stirred for two hours, proving that time is an important factor as it influences the structural properties of HAp. Figure 26 shows the XRD patterns of all the samples, there is an observable increase in peak intensity for the materials prepared for 72 hours in the autoclave. From the comparison of these samples, it is clear that Hap-(Auto72) and HApC-(Auto72)$^{(0.5\ g)}$ have an increased crystalline structure. As the X-ray reflects off the surface of the sample the increased crystallinity is observed as a more intense peak. To confirm sample identity a Pawley fit of the diffraction pattern obtained for sample Hap-(Auto72) was carried out for data in the range 10-80° 2θ to the unit cell parameters of HAp ($P6_3/m$, refined axis lengths a= 9.533(1) Å, c= 6.873(1) Å, V= 540.85 Å$^3$) on 103 indexed lines. Figures-of-merit for the refinement were *R*p= 3.32%, *R*wp= 4.24%, GoF= 1.32. Shown in figure 28 are the calculated profile (blue) against the diffraction data (red) and the difference plot. When compared to the literature diffractogram of HAp (figure 27) there is an observable difference in the Miller indices assigned to the sample in figure 28, it is, however apparent that some of the peaks are equivalent. This is due in part to overlap of peaks and the instrument used to analyse the sample. Figure 28 also shows the Miller indices showing the diffraction planes, this is unique for each diffractogram and by overlaying them it is clear to see that even with a slight shift the patterns closely mirror one another. The residual profile Rp=3.32%, residual weighted profile Rwp=4.24% and the goodness of fit Gof=1.32 collaborate the preparation and characterisation of HAp.

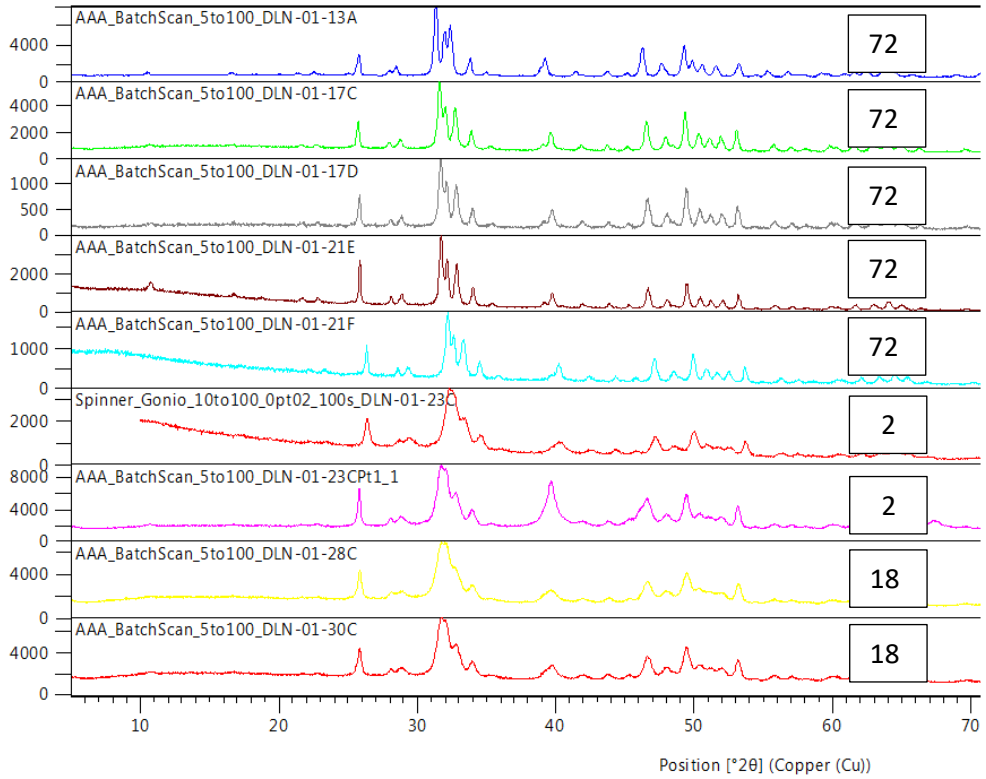


Figure 26 XRD powder patterns of HAp as a function of preparation time, time (h) is displayed on the right hand side of the figure

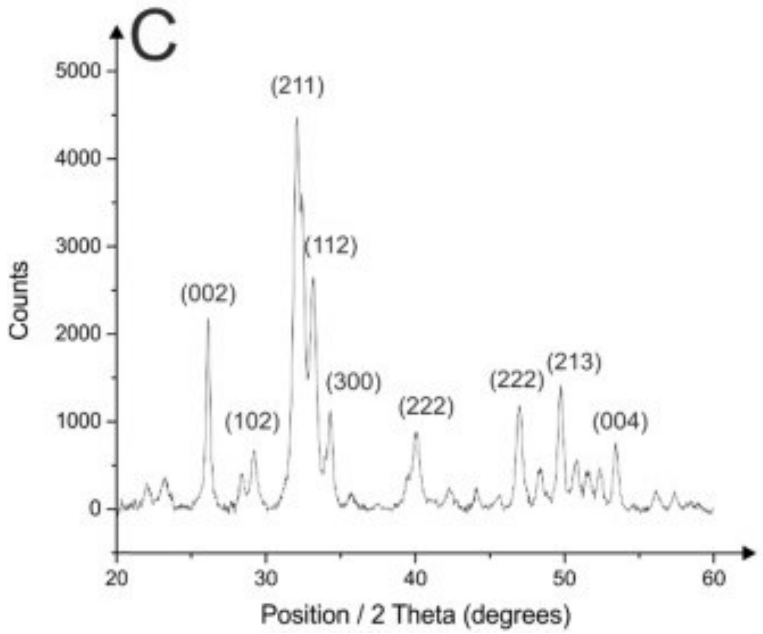


Figure 27 XRD powder pattern of HAp showing Miller indices planes[115]

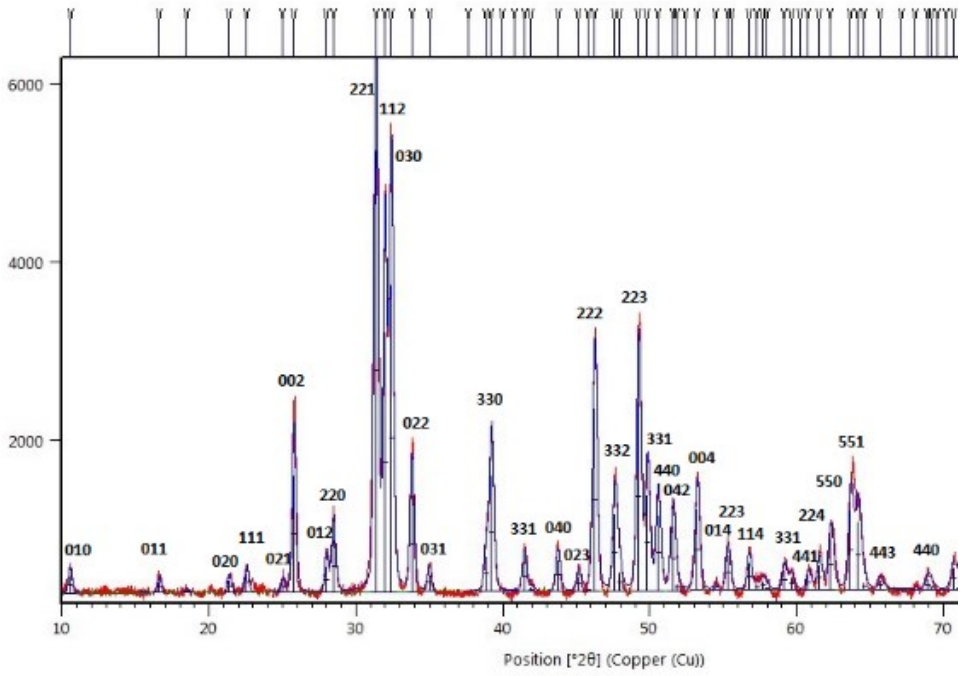


Figure 28 XRD powder pattern of Hap-(Auto72) showing Miller Indices and Pawley regression analysis (Diffraction data is shown in red, calculated profile in blue)

**Table 6 XRF Catalyst Data for Pt and Au Coated HAp**

| Elemental Mass % | HAp | Pt/Cu(MAG)-HAp(2h) | Au-HAp(Auto72) | Pt(MAG)Au-HAp(Auto72)-$TiO_2$ | Pt(MAG)-HApC(2h)$^{(0.1\,g)}$ |
|---|---|---|---|---|---|
| **Ca** | 32.2 | 37.4 | 32.2 | 19.8 | 37.1 |
| **P** | 13.0 | 15.4 | 13.0 | 6.60 | 15.9 |
| **Cu** | - | 0.23 | - | - | - |
| **Pt** | - | 1.13 | - | 0.60 | 4.72 |
| **Au** | - | - | 0.13 | 0.09 | - |
| **Ti** | - | - | - | 26.0 | - |

### 5.2 $N_2$ Adsorption Results for HAp

#### 5.2.1 Pore Size

The maximum pore diameter was 40.4 nm and the minimum 22.8 nm, with an average diameter of 29.5 nm, which is similar to the pore size reported by Boukha *et al.* who reported pore size of 32 nm.[116] The maximum and minimum pore volumes were 0.63 $cm^3\ g^{-1}$ and 0.41 $cm^3\ g^{-1}$ respectively, while the maximum surface area recorded was 82.2 $m^2\ g^{-1}$ and the minimum was 48.0 $m^2\ g^{-1}$ suggesting that as crystallinity increases the surface area decreases.

#### 5.2.2 Surface Area

With the exception of Au-HAp(Auto72) an increase in surface area is observed when the sample is coated either *via* ion exchange or sputtering. However, with this sample there is a slight reduction of 2.1 $m^2\ g^{-1}$, despite the decrease in surface area, there is an increase in pore diameter of 7.4 nm. The Au coated onto $TiO_2$ has a surface area and pore volume similar to the HAp samples, however a reduction in surface area from $TiO_2$ of 189.8 $m^2\ g^{-1}$. There is also a significant reduction in pore diameter of ~ 10 fold of the HAp sample coated in the same manner. Interestingly the surface area for Au-HAp(Auto72) is reduced in comparison to the other coated materials, this is due to the decrease seen in pore volume, and the increase in pore diameter, potentially caused by the filling of the pore during coating.

#### 5.2.3 Pore Diameter $TiO_2$

The pore diameter of 7.4 nm is confirmed by An-Cheng *et al.* who reported the pore size for Tungsten doped -$TiO_2$ as 7.3 nm.[117] As expected there are 4 different pore diameters for sample Pt(MAG0Au-HAp(Auto72)-$TiO_2$, this material was an amalgamation of two previously prepared catalysts which demonstrated excellent activity for CO oxidation and HAp and $TiO_2$, hence the 4 different pore diameters.

**Table 7 Nitrogen Adsorption Porosimetry Data of Hap**

| Sample name | Prep Time (h) | $S_{BET}$ $m^2$ $g^{-1}$ | Pore volume $cm^3$ $g^{-1}$ | BJH mean Pore Diameter nm | | | |
|---|---|---|---|---|---|---|---|
| HAp (Auto72) | 72 | 68.6 | 0.22 | 17.8 | 80.4 | | |
| HApC (Auto72)$^{(0.5\ g)}$ | 72 | 67.5 | 0.53 | 37.0 | | | |
| HApC (Auto72)$^{(0.15\ g)}$ | 72 | 56.3 | 0.41 | 31.8 | | | |
| HApC (18h)$^{(0.05\ g)}$ | 18 | 74.1 | 0.47 | 23.9 | | | |
| HApC (18h)$^{(0.1\ g)}$ | 18 | 79.9 | 0.48 | 22.8 | | | |
| HAp(2h)$^{(0.1\ g)}$ | 2 | 63.7 | 0.51 | 32.3 | | | |
| Pt-HApC(2h)$^{(0.1\ g)}$ | 2 | 82.2 | 0.63 | 22.9 | | | |
| Pt/Cu(MAG)-HAp(2h) | 2 | 62.9 | 0.67 | 32.8 | | | |
| Au-$TiO_2$ | NA | 74.7 | 0.30 | 7.4 | | | |
| Au-HAp(Auto72) | 18 | 28.6 | 0.19 | 72.0 | | | |
| Pt(MAG)Au-HAp(Auto72)-$TiO_2$ | 18 | 99.3 | 0.25 | 3.4 | 7.6 | 12.0 | 38.6 |
| $TiO_2$ | NA | 289.1 | - | - | - | - | - |

### 5.3 Thermal Gravimetric Analysis for HAp

#### 5.3.1 TGA Analysis Method

The samples were analysed using thermal gravimetric analysis to determine the levels of contamination they were adsorbing from the atmosphere. The porous HAp material is further coated for use as a catalyst, therefore it is important to have a clean material for coating, especially as adsorbed $CO_2$ on the starting material could give misleading conversion data in the oxidation reactions of $CH_4$ and CO. Figure 29 compares the main curve weight % loss over the temperature range 25-700 ˚C. From the main curve, it is apparent that all the samples lose a percentage mass of

2% up to 700 °C. This confirms the loss of water as seen in the derivative curve (figure 30). Although a very small percentage is lost after 300° C, this could be water adsorbed deeper in to the surface of the materials or potentially $CO_2$ after 600 °C as there is an apparent second dip seen at this temperature for Pt-HApC(2h)$^{(0.1\,g)}$. The result for Pt-HApC(2h)$^{(0.1\,g)}$, which shows a loss in mass % of 7% compared to the loss of 2% observed in the other samples, this is the sample which was coated with Pt, therefore it was probably subjected to the atmosphere for longer than the other samples and adsorbed more water and $CO_2$.

### 5.3.2 Loss of $H_2O$ and $CO_2$

Thermal gravimetric analysis of the samples, showed for each of the individual samples there was only a minor decrease in mass of between 0.012 to 0.151%/min as the temperature increased. The loss of approximately 0.4-1.0 mg across all samples was probably the loss of moisture or $CO_2$ at a temperature range of 25 °C to 200 °C; this is observed as a drop in the derivative curve at a temperature of ~ 70 °C. Figure 30 shows the TGA derivative curve for all the samples ran. When compared to literature values, Costescu *et al.* confirms the endothermic loss of adsorbed water in the temperature range of 25 to 300 °C.[118] Costescu *et al.* also reported the loss of $CO_2$ in the range of 600 to 800 °C, however of the samples analysed no second drop in mass is recorded outside the range shown in figure 30. As the TGA analysis only showed the expected loss of water, further analysis of samples was deemed unnecessary.

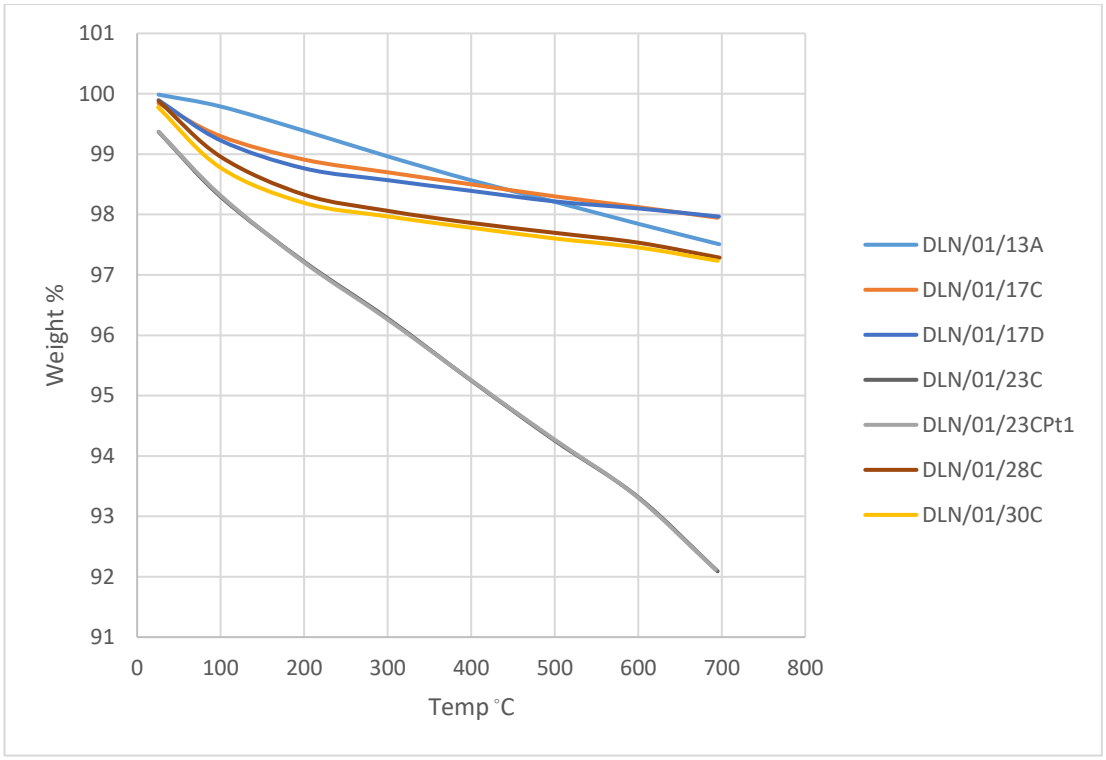


Figure 29 (Main Curve-Thermal Gravimetric Analysis) 3% Drop in mass recorded except Pt-HApC(2h)$^{(0.1\ g)}$ 7%

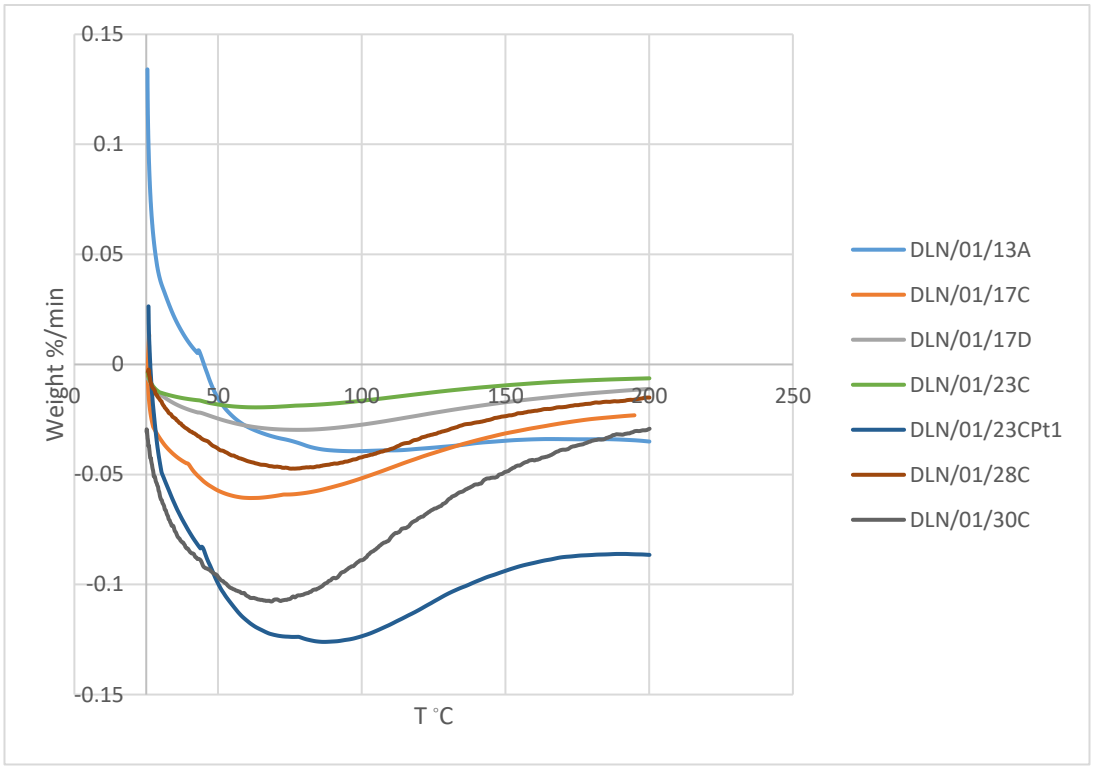


Figure 30 (Derivative Curve-Thermal Gravimetric Analysis) $H_2O$ and $CO_2$ desorbed between 25 – 200 ˚C

### 5.3.3 FTIR analysis for HAp

IR spectroscopy was used in order to determine peaks associated with HAp. Figure 31 shows peaks at 3570 $cm^{-1}$ OH, 3218 $cm^{-1}$ $H_2O$ absorbed, 2323 $cm^{-1}$ $CO_3^{2-}$ absorbed, 1644 $cm^{-1}$ $OH^-$ indicative of HAp, 1089 $cm^{-1}$ $PO_4^{3-}$, 1024 $cm^{-1}$ P-OR or P-H. In some, but not all the samples the $OH^-$ peak at 1644 $cm^{-1}$ is not observed and the carbonate peak is missing. This can be explained by the time the sample was in contact with the atmosphere. The samples were heated to 550 °C under helium before testing, therefore this should not influence the chemistry of the catalyst. Joscheck *et al.* published a paper on the FTIR spectroscopic peak signals associated with calcium phosphates.[119] The findings corroborate the peak signals as reported above.

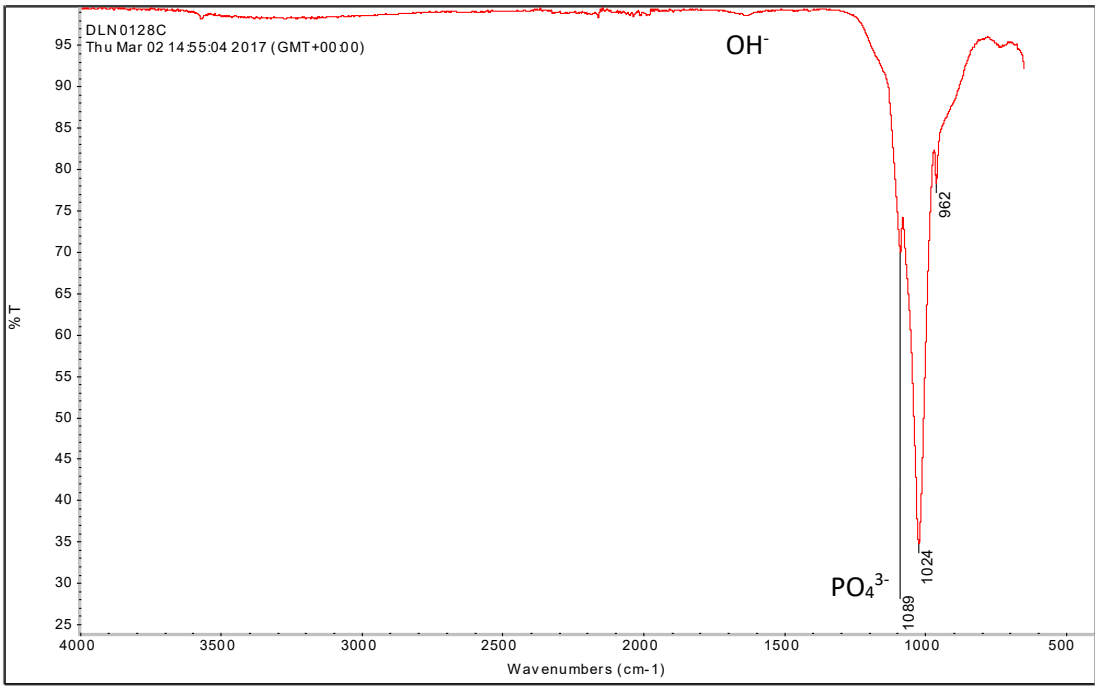


Figure 31 FTIR Spectrograph of HAp Showing Peaks indicative of HAp

### 5.4 Scanning Electron Microscope Analysis for HAp

#### 5.4.1 SEM Method

The SEM images for HAp(Auto72)clearly show two distinct structures; this matches with the BET surface area analysis, which displayed two different types of pore. The structures observed in the SEM images for HAp(Auto72) were predominantly the ones seen in the first two images

(straw structure), with only a minor part of the sample imaging the nodules. The images for all the other samples are similar across the range, images taken at three different areas across the sample to demonstrate their uniformity. Of all the prepared catalysts the effect of preparation time on the crystallinity of the sample is clearest to see in Au-HAp(Auto72).

### 5.4.2 SEM Images of HAp

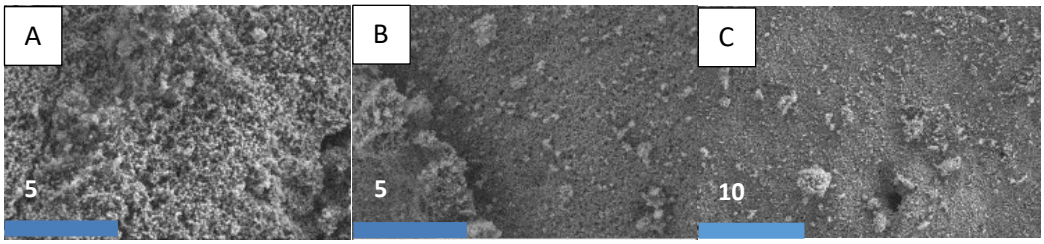


Figure 33 SEM images of HApC-(Auto72)$^{(0.5\ g)}$ (Magnification A: 5 µm, B: 5 µm, C: 10 µm)

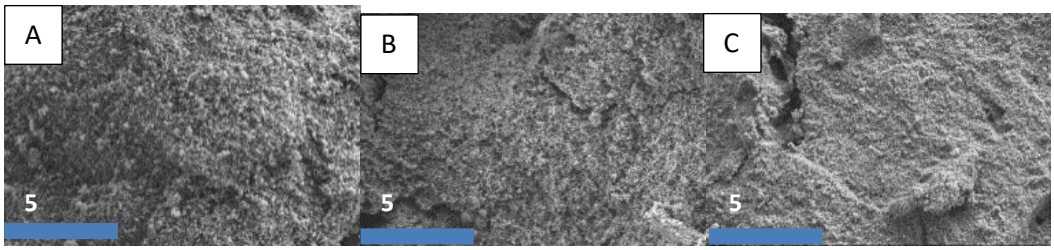


Figure 34 SEM images of HApC(Auto72)$^{(0.15\ g)}$ (Magnification A: 5 µm, B: 5 µm, C: 5 µm)

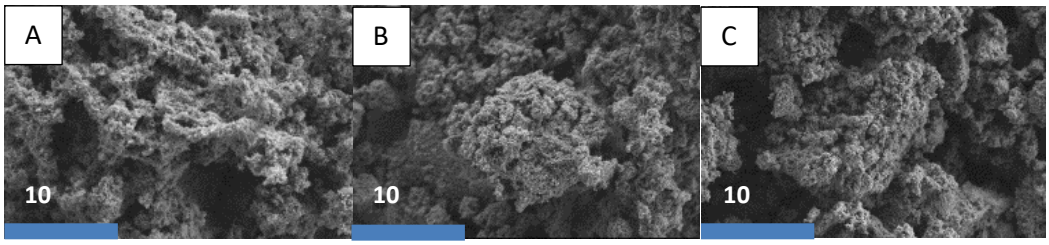


Figure 35 SEM images of HApC(2h)$^{(0.1\ g)}$ (Magnification A: 10 µm, B: 10 µm, C: 10 µm)

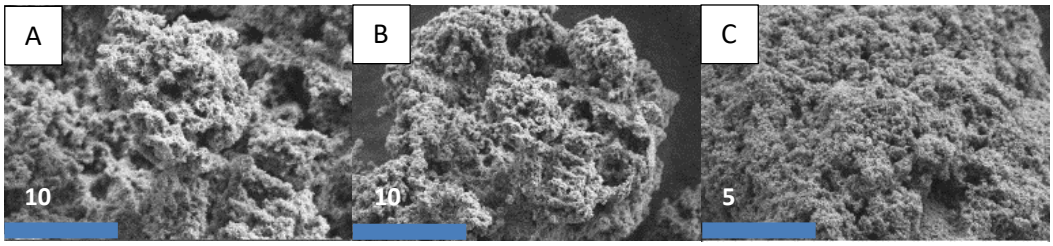


Figure 36 SEM images of Pt-HApC(2h)$^{(0.1\ g)}$ (Magnification A: 10 µm, B: 10 µm, C: 5 µm)

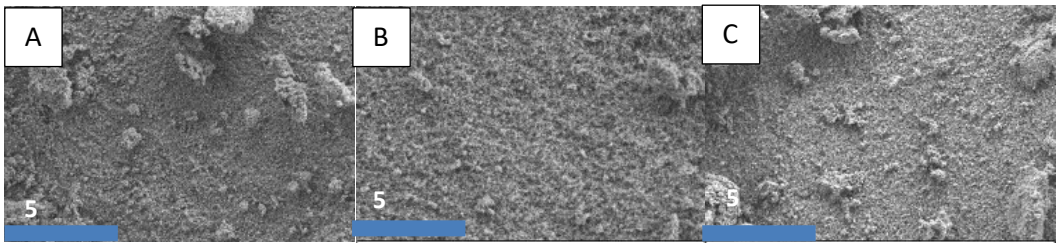


Figure 37 SEM images of HApC(18h)$^{(0.05\ g)}$ (Magnification A: 5 µm, B: 5 µm, C: 5 µm)

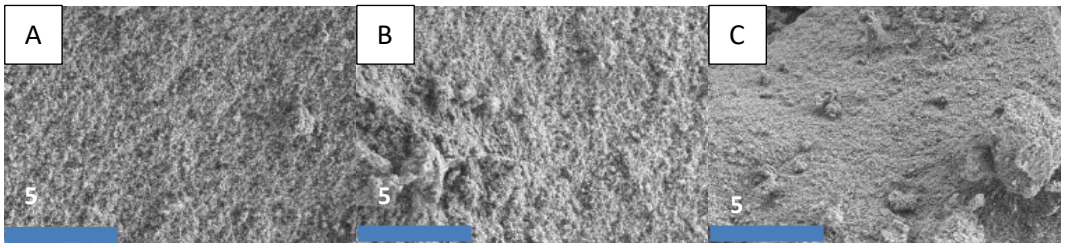


Figure 38 SEM images of HApC(18h)$^{(0.1\ g)}$ (Magnification A: 5 µm, B: 5 µm, C: 5 µm)

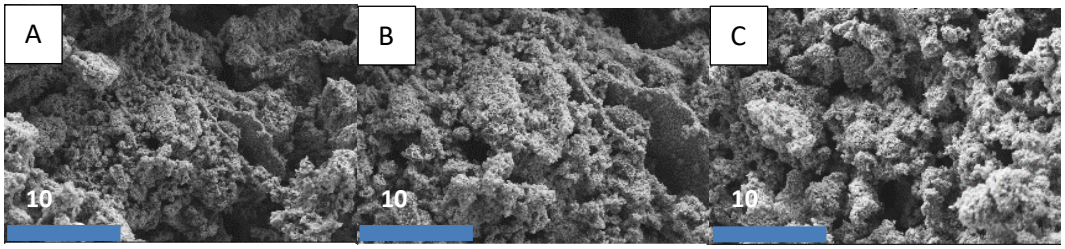


Figure 39 SEM images of Pt/Cu(MAG)-HAp(2h) (Magnification A: 10 µm, B: 10 µm, C: 10 µm)

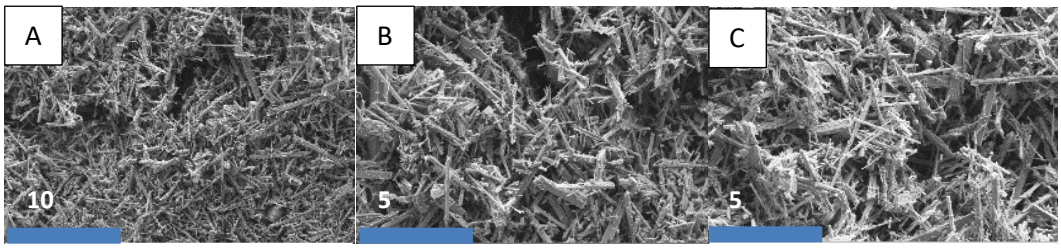


Figure 40 SEM images of Au-HAp(Auto72) (Magnification A: 10 µm, B: 5 µm, C: 5 µm)

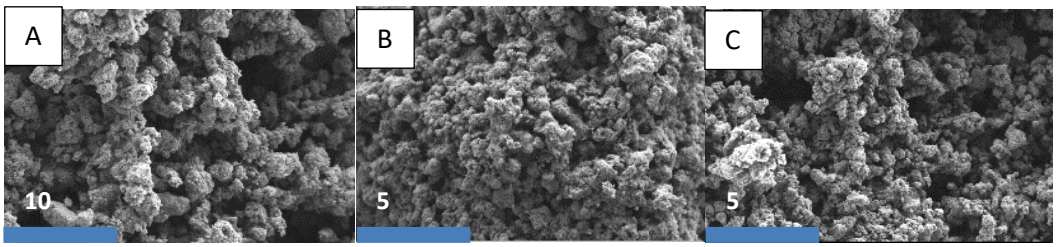


Figure 41 SEM images of Au-$TiO_2$ (Magnification A: 10 µm, B: 5 µm, C: 5 µm)

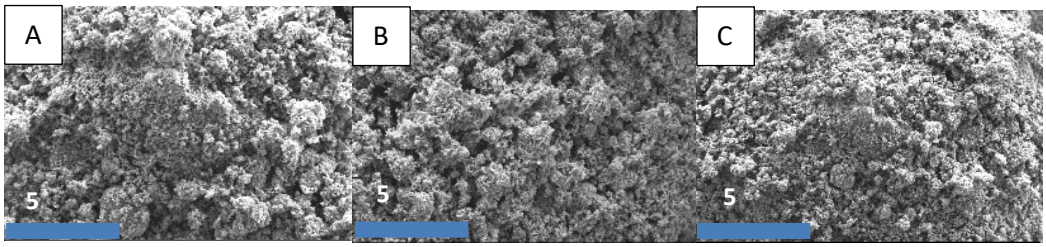


Figure 42 SEM images of Pt(MAG)Au-HAp(Auto72)-$TiO_2$ (Magnification A: 5 µm, B: 5 µm, C: 5 µm)

**Table 8 EDX Data for Prepared Catalysts**

| Element | HApC(2h)$^{(0.1\ g)}$ Wt% | Pt-HApC(2h)$^{(0.1\ g)}$ Wt% | $AuTiO_2$ Wt% | Pt(MAG)AuHAp(Auto72)$TiO_2$ Wt% |
|---|---|---|---|---|
| O | 33.19 | 33.45 | 31.32 | 43.70 |
| P | 20.11 | 20.07 | - | 9.12 |
| Ca | 41.15 | 39.81 | - | 17.05 |
| Pt | - | 2.59 | - | - |
| Ti | - | - | 66.96 | 24.09 |
| Au | - | - | 1.08 | - |

## 6. Catalysis

Figure 43 shows the difference in CO oxidation when using no catalyst compared to HAp. $CO + ½\ O_2 \rightarrow CO_2$, 100% conversion is achieved with no catalyst at 400 ˚C compared to HAp where a decrease of 50 ˚C is observed for 100% conversion. Of the 6 catalysts tested (figure 44) there is a shift to the left the lowest temperature recorded for 100% conversion is for the catalyst Au-HAp(Auto72). At 140 ˚C this catalyst achieves full conversion of CO to $CO_2$. Table 9 shows the catalysts tested and the lowest temperature where 100% conversion occurs. Of the catalysts tested, Au/$TiO_2$ demonstrates 83% conversion at the lowest temperature 50 ˚C. This is confirmed by Dominguez *et al.* who reported 100% conversion between 25 – 30 ˚C, however interestingly they

recorded a drop off, of conversion over 200 ˚C that is not seen with any of the catalysts prepared herein. Of all the catalysts synthesised once 100% conversion occurs at lowest programmed temperature the catalysts remain active up to 550 ˚C. The Pt coated *via* magnetron sputtering (Pt-HApC(2h)$^{(0.1\,g)}$), however showed 100% conversion on cooling, suggesting that once the surface of the material reaches 150 ˚C (full conversion) the catalyst remains active on temperature programmed cooling as low as 50 ˚C.

### 6.1 Stability Test

Due to the industrial application of the catalysts being prepared they were subjected to an initial stability test. The stability of the catalysts was tested under normal analysis conditions up to 6 hours. At time = 0 the reactor was dwelling at 50 ˚C for a period of 10 minutes. Figure 45 shows a programmed temperature ramp of 5 ˚C/min, dwelling at analysis temperature for 10 minutes before continuing to ramp up to the lowest temperature where 100% conversion occurs. The data in figure 45 shows that once 150 ˚C (lowest 100% conversion temperature) was reached the catalyst (Pt-HApC(2h)$^{(0.1\,g)}$) remained active for 380 minutes providing 100% conversion throughout. For the Au-$TiO_2$ sample 100% conversion was at 250 ˚C, this is a 60 ˚C increase in temperature from the first run with this sample, however, once it reached 100% it remained active for 5 hours under isothermal conditions. Catalyst Au-HAp(Auto72) reached 100% conversion at 180 ˚C, however a drop off from 100% was observed at 60 and 120 minutes. This reduction in percentage conversion was however only minimal at 0.1 and 0.2% respectively. The temperature was increased by 10 ˚C at 180 minutes, which gave a 100% conversion, however the fluctuation albeit minimal (0.2%) at 210 minutes was again observed. In the 5$^{th}$ hour of the stability test (total time on stream 6.5 hours) a drop in conversion of 0.8%. Followed by a further drop to 95.2% recorded on the 6$^{th}$ hour. Further stability testing will need to be carried out on all future catalysts and the length of the study increased.

## 6.2 CO Oxidation Conversion Data

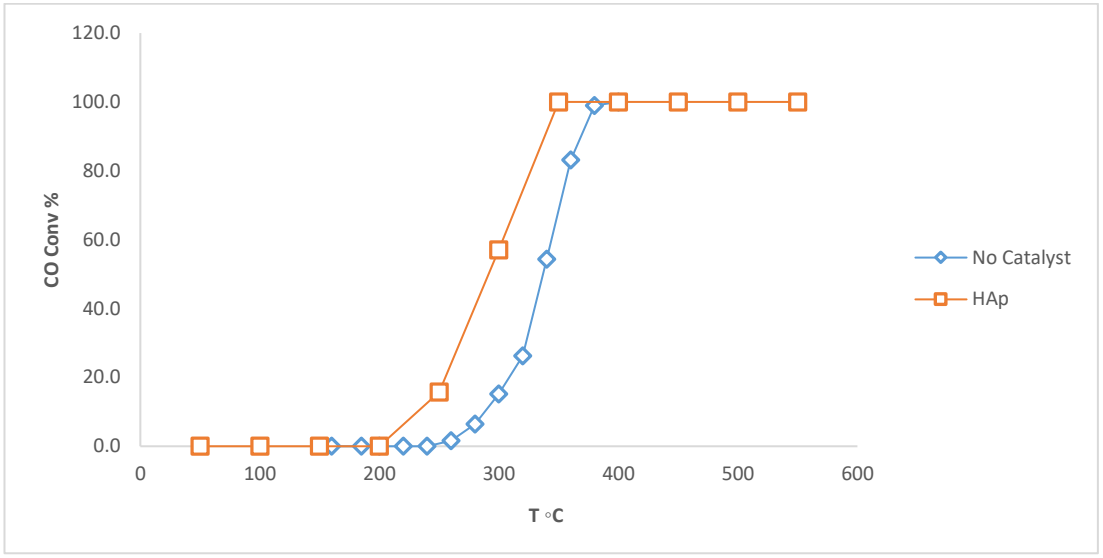


Figure 43 CO Conversion Data for No Catalyst vs HAp

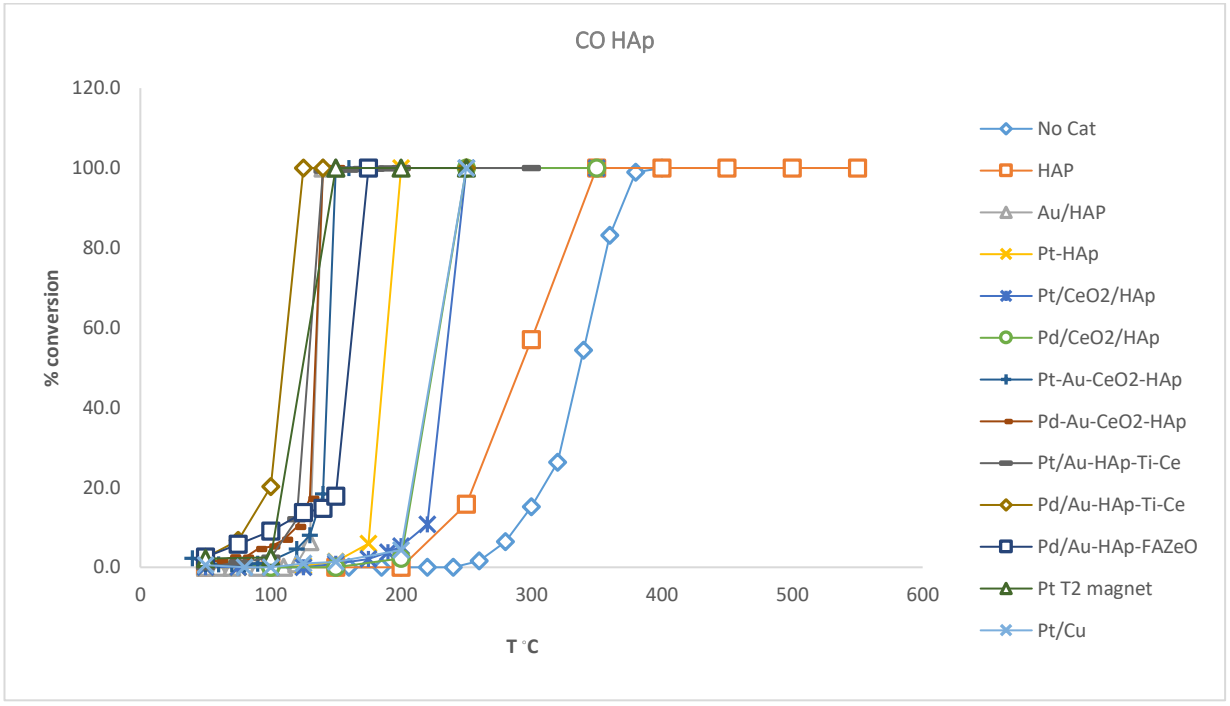


Figure 44 CO Conversion Data for Prepared HAp Catalysts

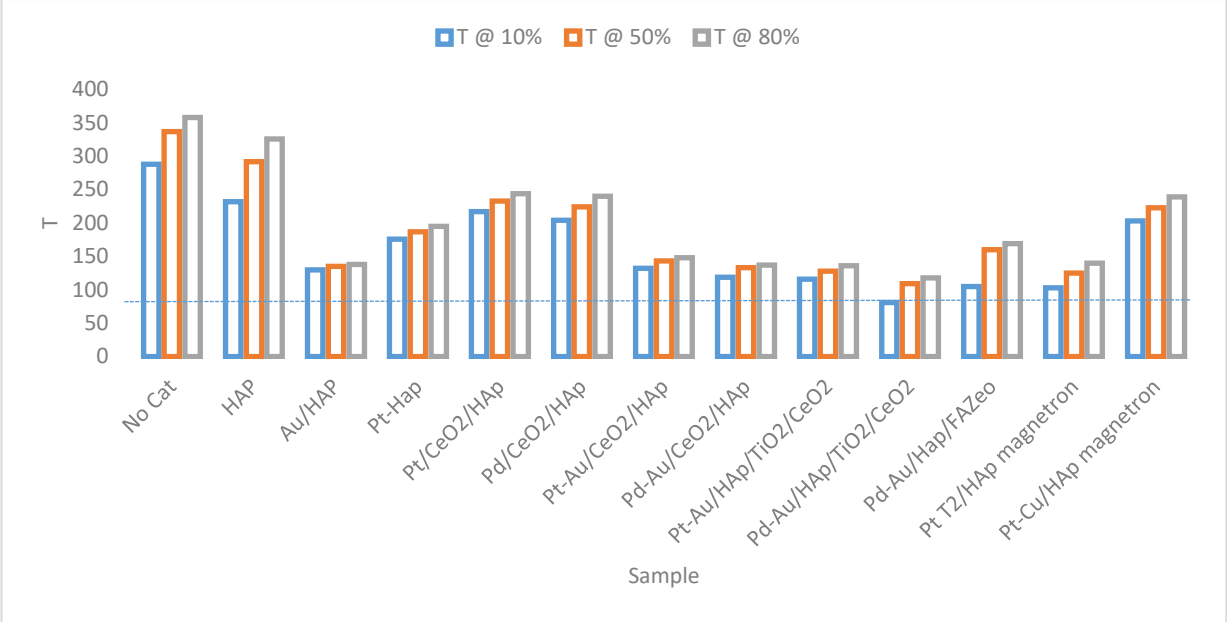


Figure 45 Temperature at which 10, 50 and 80% Conversion is achieved for CO combustion with HAp catalysts

**Table 9 Lowest Temperature of 100% Conversion Catalysts Tested**

| Sample Name | Temperature ˚C | % Conversion |
|---|---|---|
| **Pt-HApC(2h)$^{(0.1\ g)}$ T1** | 200 | 100 |
| **Pt-HApC(2h)$^{(0.1\ g)}$ T2** | 150 | 100 |
| **Au-HAp(Auto72) (DLN0186Au-HAp)** | 140 | 100 |
| **Pt/Cu(MAG)-HAp(2h)** | 250 | 100 |
| **Pt(MAG)Au-HAp(Auto72)-$TiO_2$ (DLN0123CPt1)** | 250 | 100 |
| **Au/$TiO_2$ (DLN0177BAu/$TiO_2$)** | 140 | 100 |

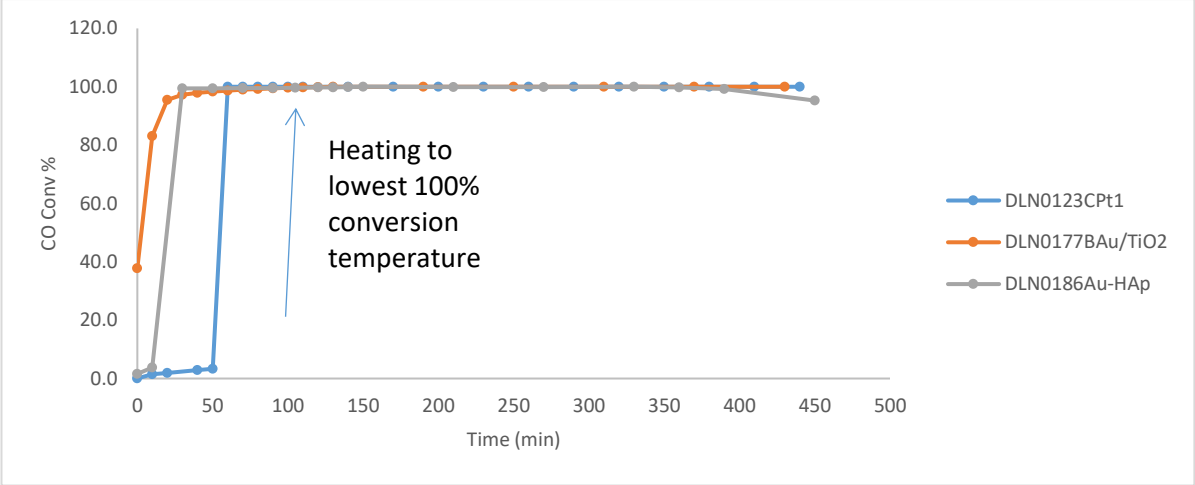


Figure 46 CO Oxidation Graph Stability 6 Hours

### 6.3 $CH_4$ Conversion for HAp

Figure 47 shows the $CH_4$ conversion rates; $CH_4 + 2O_2 \rightarrow CO_2 + 2H_2O$. The highest conversion to $CO_2$ (98%) is achieved by Pt-HApC(2h)$^{(0.1\ g)}$ which also demonstrated excellent activity for CO oxidation. However, this conversion was only achieved at 600 ˚C. M. Cargnello *et al.* have reported a Pd-$CeO_2$ catalyst protected in a core-shell that demonstrates 100% conversion at 400 ˚C.[120]

#### 6.3.1 $CH_4$ Oxidation Conversion Data

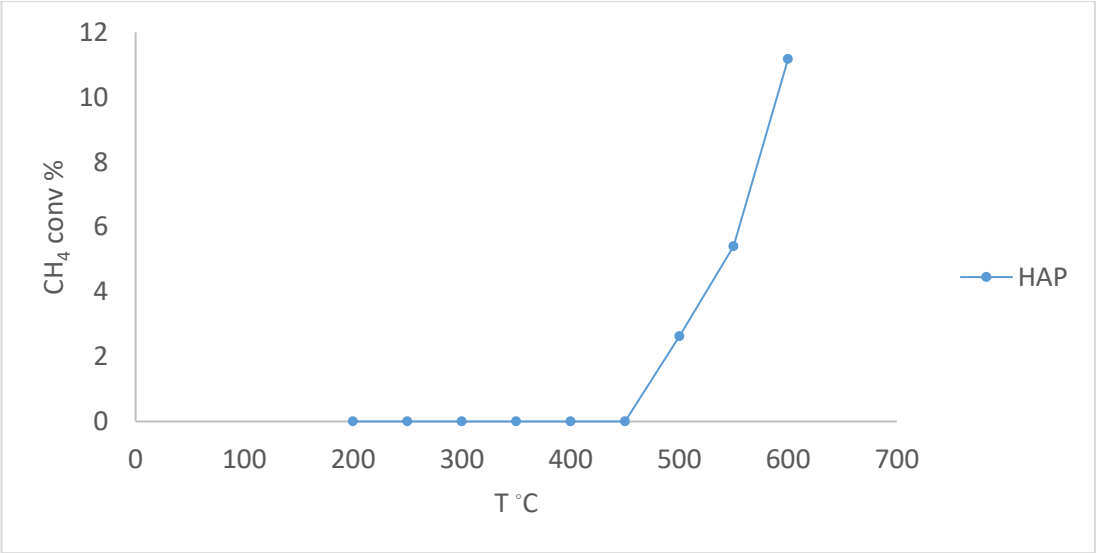


Figure 47 $CH_4$ Conversion HAp

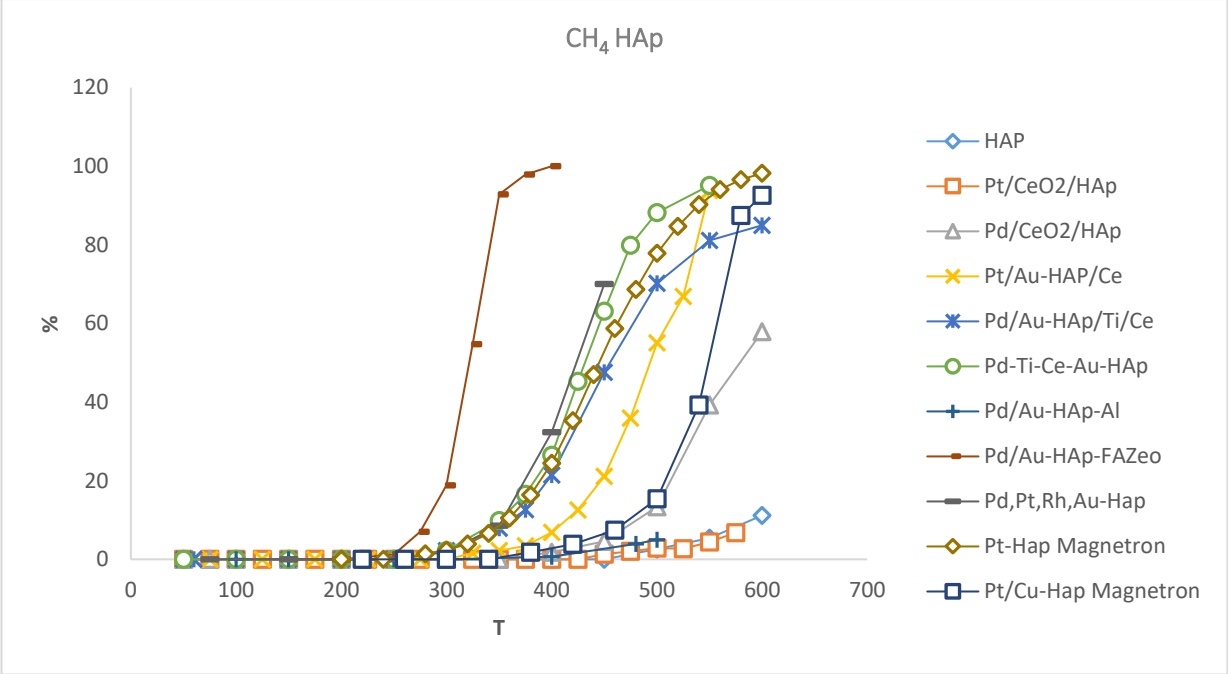


Figure 48 $CH_4$ Conversion HAp vs Catalysts

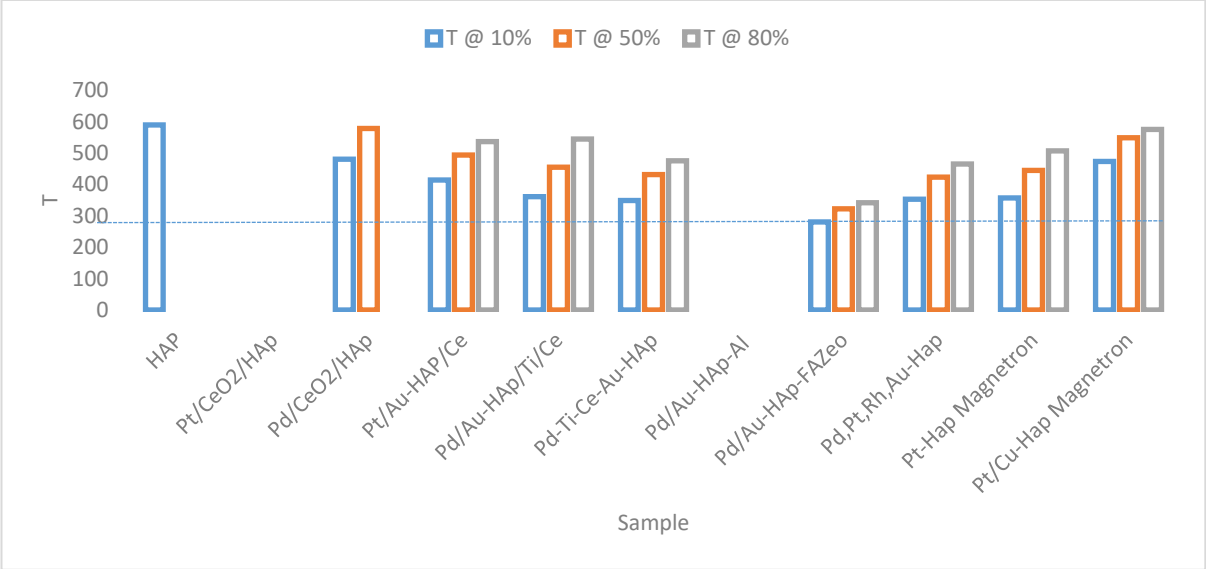


Figure 49 Temperature at which 10, 50 and 80% conversion is achieved for the combustion of $CH_4$ with HAp catalysts

## 6.4 Conclusion HAp

### 6.4.1 Crystallinity of HAp

The preparation time and method was altered to demonstrate how increasing the time HAp is synthesised increases the crystallinity of the structure. XRD and BET analysis showed as

crystallinity increased there was a notable decrease in surface area. Of the prepared catalysts the main influence in the crystallinity of the materials prepared is the effect time has on the structural properties.

### 6.4.2 CO Oxidation HAp

For the oxidation of CO to $CO_2$ all the catalysts tested achieved 100% conversion below 300 °C and remained active up to 550 °C. In the stability tests carried out over a 6 hour time frame and at the lowest temperature recorded for complete conversion, all the catalysts (figure 45) remained active for the duration of the study. However, a drop off of 4.8% to 95.2% conversion was observed for sample Au-HAp(Auto72). It is has been suggested that surface water on the metal catalyst plays a significant role in the oxidation process of CO to $CO_2$ when using gold on $TiO_2$. However, in the reaction chamber the catalyst was heated to a calcination temperature of 550 °C before the reaction gases were added, thus driving away any available water to assist in the oxidation process. It is, therefore, most likely the particle size and cluster shapes of the gold nanoparticles, coupled with the support, that are responsible for the oxidative reaction.

### 6.4.3 $CH_4$ Oxidation HAp

The catalysts that were active for the oxidation of $CH_4$ were the Pt catalysts, as none of the Au coated catalysts demonstrated activity. Pt-HApC(2h)$^{(0.1\ g)}$, which was the sample coated *via* the magnetron sputter method gave the best result with a 98% conversion rate at 600 °C. There is an apparent shift to the left as seen in figure 47, however, none of the catalysts tested give 100% conversion. The breaking of the C-H bond in $CH_4$ requires a lot more energy than a C-O bond in CO, as demonstrated by the increase in temperature for the reaction to occur. The steps involved, as shown in equations 1-8, when compared to equations 9-12 also demonstrate that the oxidation of $CH_4$ is a very different mechanism. In a number of different papers' the reported low temperature combustion of $CH_4$ to carbon dioxide has alluded to temperatures in the range of 500-600 °C.[121] The results demonstrate that complete conversion of $CH_4$ to carbon dioxide is attainable at

temperatures below 400 °C. In fact, complete conversion was achieved as low as 300 °C the Pd/Au-$TiO_2$ catalyst which was tested twice to confirm its activity. The catalyst with the lowest temperature, for overall conversion was the catalyst composed of a FAU zeolite coated with Pd and Au. The catalyst with the second lowest temperature for full conversion is the Pd/Au-ZeO-$TiO_2$-$CeO_2$ (393 °C). This demonstrates a link between the concentration of $AuCl_4$ solution and the overall amount of gold dispersed on the catalytic support. The worst three performing catalysts all have $AuCl_4$ solutions set at 0.005 M with the Pd salts either slightly increased to 0.006 M in the case of Pd/Au-ZeO-$TiO_2$-$CeO_2$ (2) or equivalent concentration. This is succinctly observed with the reduction to 0.004 M Au loading in Pd/Au-ZeO-$TiO_2$-$CeO_2$ (1) as a sharp drop in conversion temperature to 360 °C. All three catalysts had surface areas > 200 $m^2$ $g^{-1}$ and were synthesised in the same way. However, in direct contrast to the hypothesis that Au : Pd concentration when the same has an adverse effect on the overall temperature 100% conversion is achieved. The catalysts that were prepared with single supports and the same concentrations of precious metal salts show a reduction in conversion temperature. Pd/Au-Hy-ZeO and Pd/Au-$Al_2O_3$, both converted $CH_4$ to $CO_2$ at 350 °C. With the removal of the gold loading altogether a significant decrease to 325 °C was observed for the Pd-$Al_2O_3$ catalyst and 340 °C for the Pd-Hy-ZeO cat. However, when the Au salt was re-introduced at a decreased concentration 0.002 M, full conversion temperature of 300 °C is observed. Some 300 °C lower than reported in several papers as low temperature $CH_4$ conversion. There is no obvious correlation between the surface area of the catalysts and the activity shown. In-fact the two best catalysts had the biggest difference in surface area size, 262 and 140 $m^2$ $g^{-1}$ respectively. It is clear from the results that the addition of $CeO_2$ has a positive effect on the conversion rate of $CH_4$, however, this reduction in temperature can also be explained by the reduction in Au loaded on to the catalytic support. The option to remove gold altogether was considered, however, gold plays a crucial role in the oxidation of CO, thus it was decided to leave it in.

## 7.1 XRD Method

### 7.1.1 XRD

X-ray powder diffraction (XRD) data was collected on a PANalytical X'Pert powder diffractometer using a Cu anode (Cu $k\alpha_1$ $\lambda$= 1.540598Å) fitted with a PIXcel 1D detector operating in scanning line detector mode. Samples measured in reflection geometry in the range 5 - 100° 2θ with a step size of 0.01° 2θ, a sweep time of 0.033°/s and an overall scan time of 49 minutes. Initial XRD data was gathered for the substrates before they were modified with the catalytically active metals and any promoters that were used. The raw substrate diffractogram will enable the quick assignment of any extra peaks in the data, assuming the overall mass wt% increase is over 3%. Another contributing factor for peak assignment of the precious metals that have been coated on to the substrates in figures 50 - 53 is the dispersion of precious metal over the supportive catalytic materials. From the TEM analysis of several of the wet synthetic and magnetron coated catalysts it is clear to see that excellent dispersion has been accomplished. This will make the assignment of certain peaks utilising XRD impossible, as will the broad diffraction patterns of the substrates $TiO_2$, $Al_2O_3$ and the promoter $CeO_2$. From examining peak patterns on the PANalytical X'Pert powder diffractometer, the peaks from the database match the substrates closely for $CeO_2$ and $TiO_2$, however, there is a degree of error associated with $Al_2O_3$ due to the small size of the crystallites, seen as broad peaks in figure 52. Figure 53 shows the diffractogram for the materials which were magnetron sputtered for 15 minutes. Due to the small particle sizes confirmed with TEM it is not possible to assign peaks for Pd and or gold, however the addition of $CeO_2$ is observed as a peak at 28 °2θ for the three supports $TiO_2$, $Al_2O_3$ and zeolite. This is confirmed in figures 54 and 55 for the materials sputtered for 10 and 20 minutes respectively.[122]

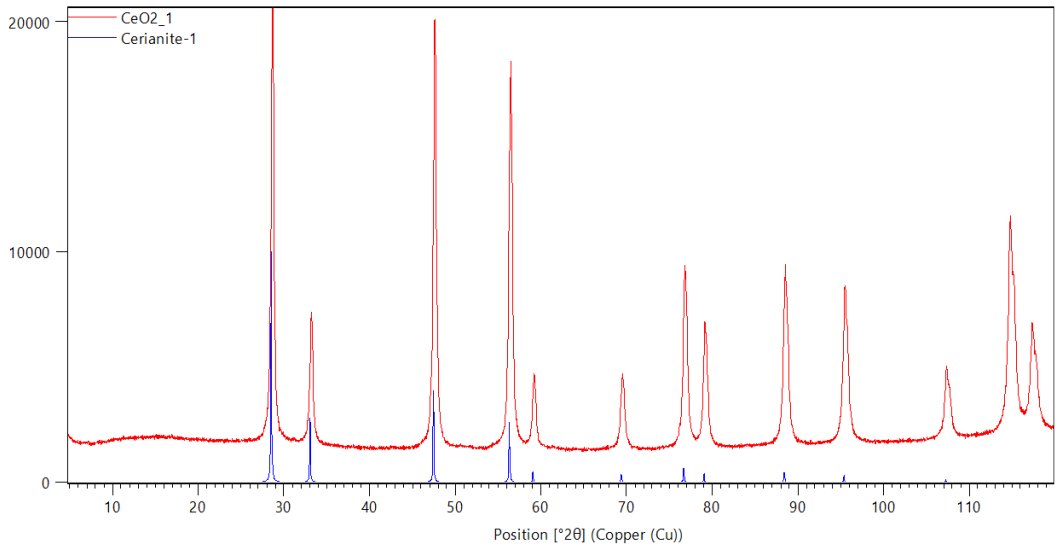


Figure 50 XRD diffractogram images for $CeO_2$ in red compared to database patterns in blue

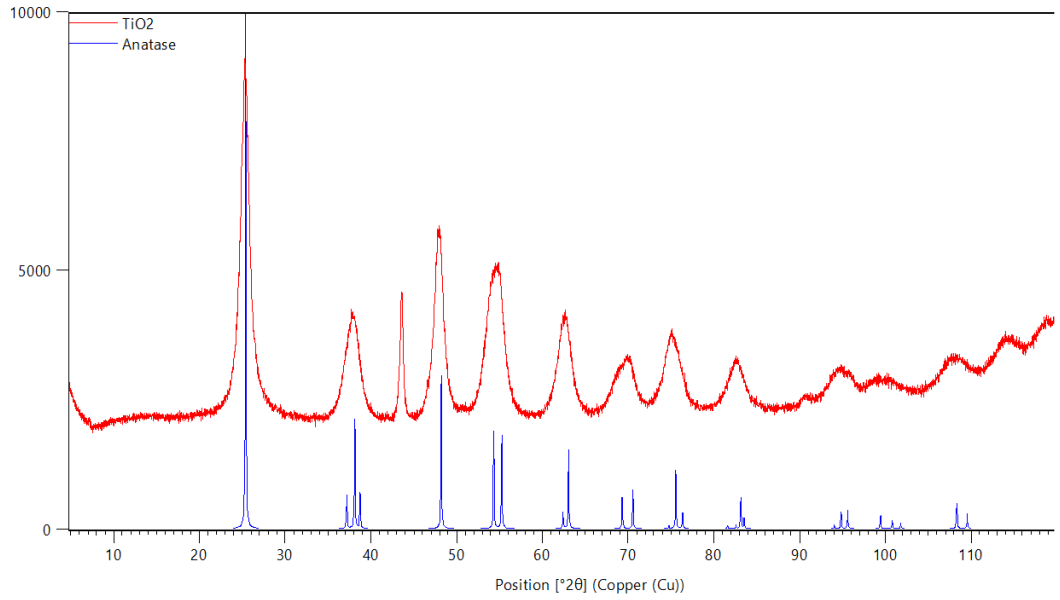


Figure 51 XRD diffractogram images for $TiO_2$ in red compared to database patterns in blue

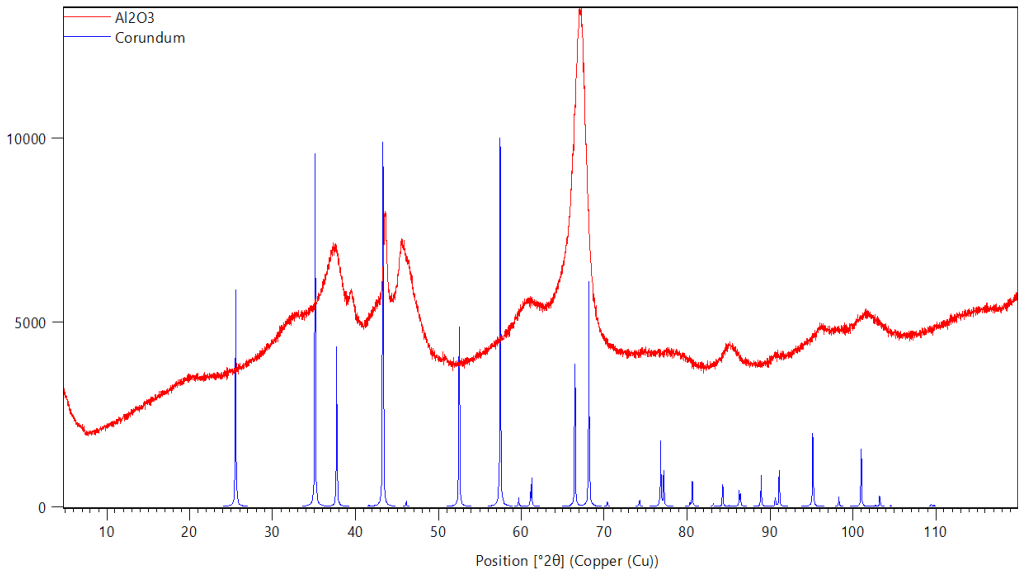


Figure 52 XRD diffractogram images for $Al_2O_3$ in red compared to database patterns in blue

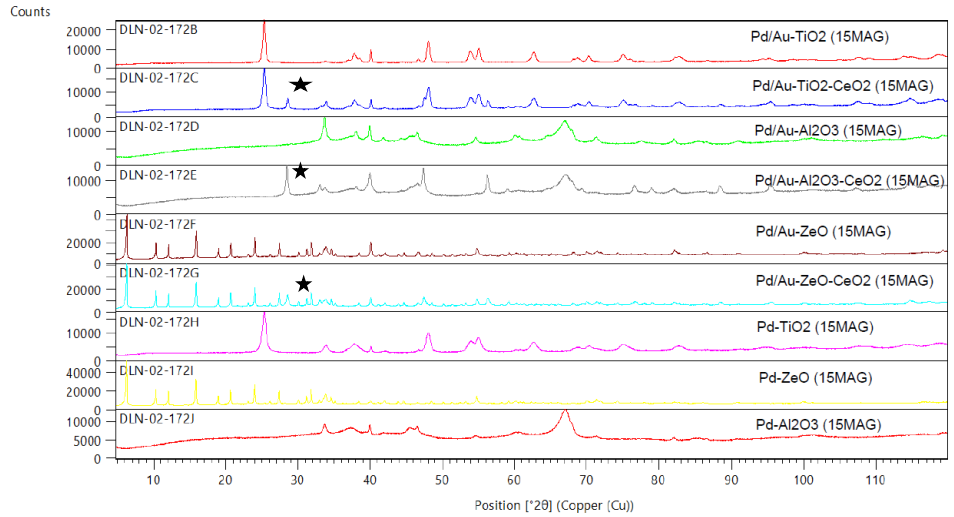


Figure 53 15 minute PVD magnetron sputtered samples XRD data black stars indicate $CeO_2$

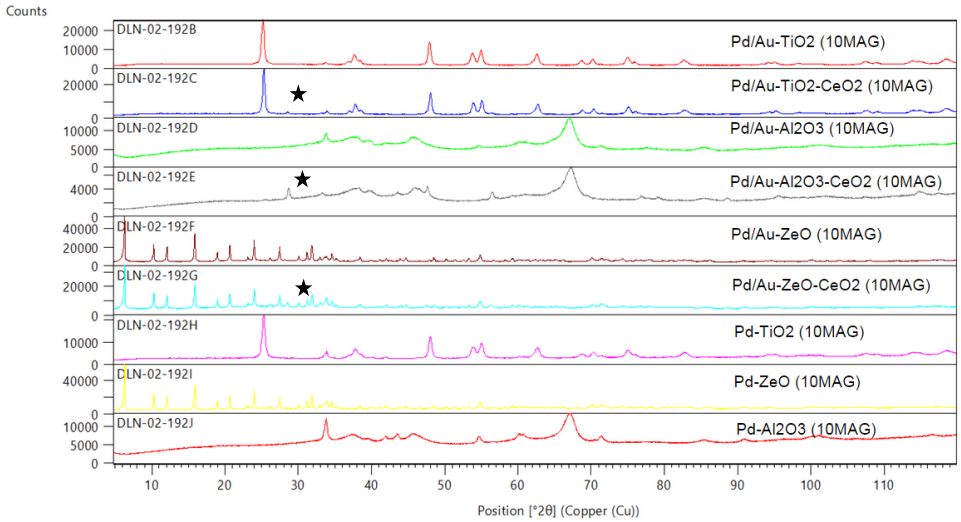

Figure 54 10 minute PVD magnetron sputtered XRD data black stars indicate $CeO_2$

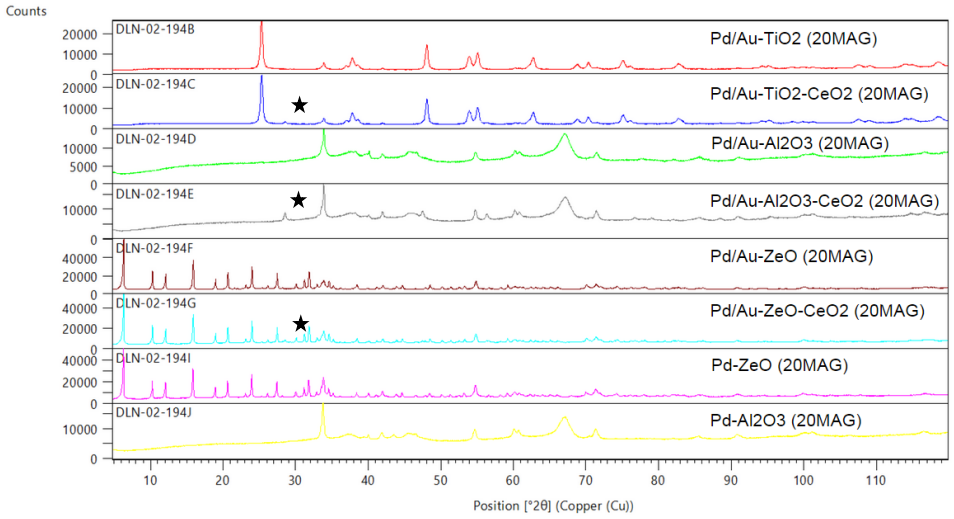


Figure 55 20 minute PVD magnetron sputtered XRD data black stars indicate $CeO_2$

## 7.2 TEM analysis for a select group of catalytic materials

Figures 56 to 59 show a series of TEM images for some of the catalytic materials in this report. Figure 56 displays the elemental maps for Ti, Pd and Au associated with the catalyst Pd/Au-$TiO_2$. This material demonstrated 100% conversion of CO to $CO_2$ at 85 °C, however, it was not as active for $CH_4$ combustion, only reaching 92% at 400 °C. It can clearly be seen that the Pd is well dispersed across the sample substrate $TiO_2$, therefore it must be the reduction in surface area of this sample, as it is only 91.4 $m^2\ g^{-1}$. The Pd loading wt% for the catalyst is 2.78 and for gold 0.78, which when compared to other materials in the series are relatively similar, thus pointing toward the lack of surface area for the inactivity observed in the $CH_4$ reaction. The Pd/Au-$TiO_2$-$CeO_2$-ZeO catalyst has a Pd and Au wt% of 5.9 and 3.5 respectively and a surface area of 262.3 $m^2\ g^{-1}$. The $CeO_2$, gold and especially palladium are well dispersed over the substrate. The increased surface area in comparison to the previous catalyst coupled with the increased precious metal loading and well dispersed nanoparticles over the support proved to be three decisive parameters for low temperature full oxidation of $CH_4$. Figures 35 and 36 show the elemental maps and particle sizes for the previously reported Na-FAU-Pd (Geo-12) and also the Na-FAU-PdMAG (Geo-12) catalysts.[123] Of all the catalytic materials herein, the two geothermal materials proved to

be the most active, Na-FAU-Pd (Geo-12) for the full oxidation of $CH_4$ and Na-FAU-PdMAG (Geo-12) for the complete oxidation of CO. It is clear that Pd has been well dispersed over the zeolite for both the WI and PVD materials. The characteristics of zeolites as a support has been reported here [124] by Petrov et al, they also reported that due to the increased porosity of zeolite materials, sintering and therefore loss of activity is greatly reduced. [125,126]The dark clusters around the edges of figure 59 (b) and the dark spots in figure 58 (b) are thought to be well dispersed Pd over the support and have particle sizes ranging from 2-50 nm.

### 7.2.1 Pd/Au-$TiO_2$ Elemental Mapping

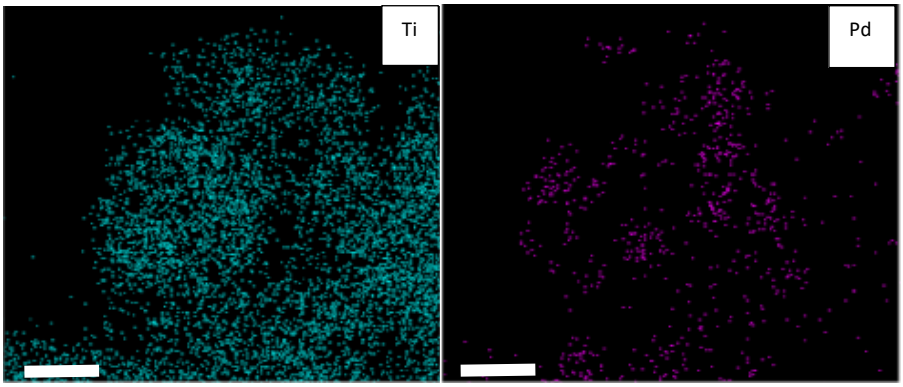


Figure 56 Tem Elemental mapping for Pd/Au-$TiO_2$ the white bars in the bottom left corner of each map indicate 25 nm

### 7.2.2 Pd/Au-$TiO_2$-$CeO_2$-ZeO1 Elemental Mapping

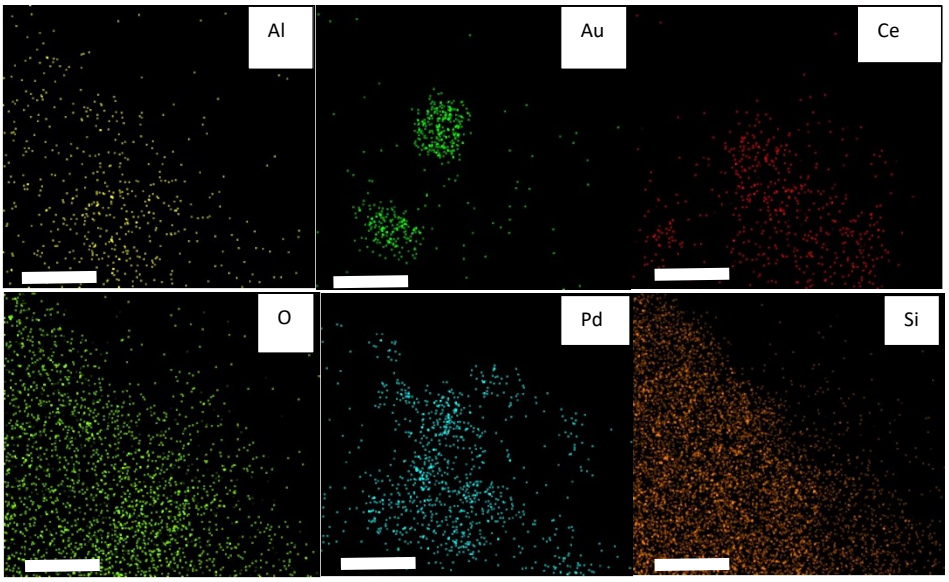

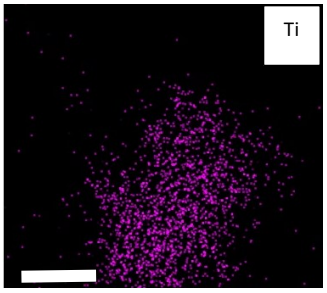


Figure 57 TEM elemental mapping for Pd/Au-$TiO_2$-$CeO_2$-ZeO1. The white bars in the bottom left corner of each map indicate 25 nm

### 7.2.3 Na-FAU-Pd (Geo-12) Elemental Mapping

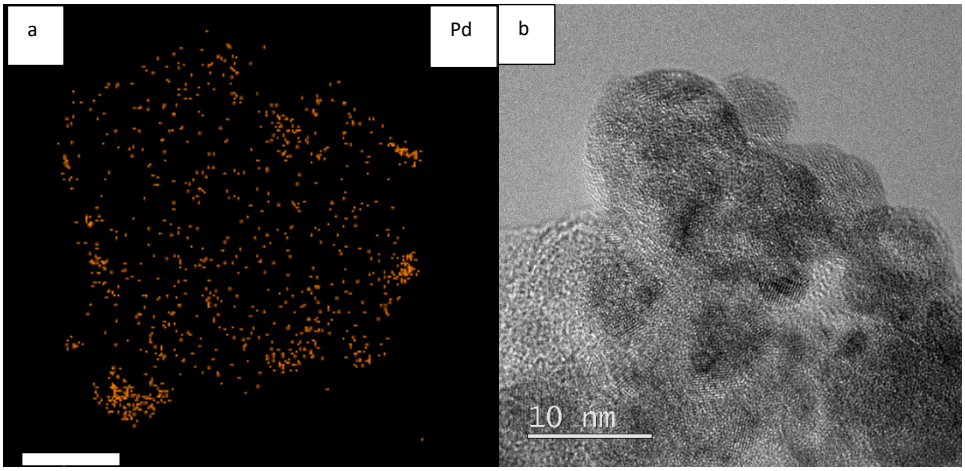


Figure 58 TEM elemental mapping (a) for Na-FAU-Pd (Geo-12) & 10 nm resolution image (b)

### 7.2.4 Na-FAU-PdMAG (Geo-12) Elemental Mapping

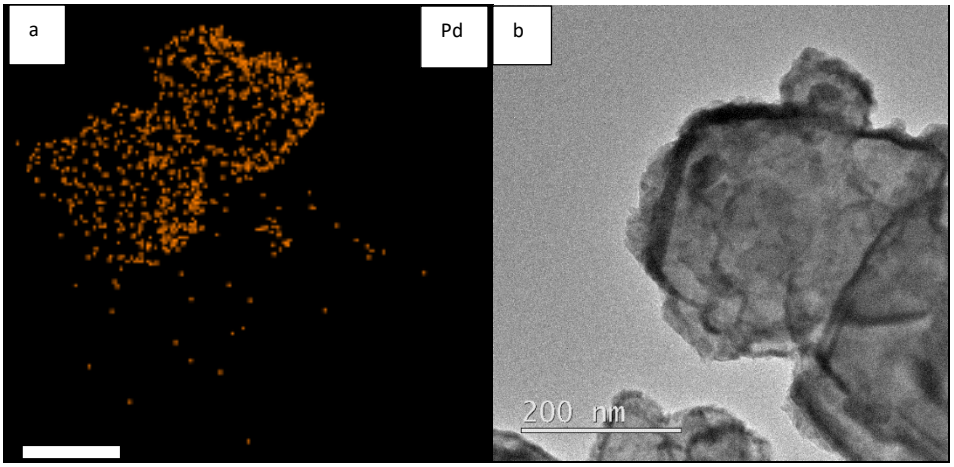


Figure 59 TEM Elemental mapping (a) for Na-FAU-PdMAG (Geo-12) & 200 nm resolution image (b)

## 7.3 Low temperature CO/$CH_4$ Catalysts

### 7.3.1 CO

Figure 60 shows a series of CO conversion curves for the complete combustion of CO when reacted with oxygen.

$$\frac{1}{2}O_2 + CO \rightarrow CO_2 \qquad (20)$$

all catalysts reached 100% conversion before 200 °C. The conversion data in figure 60 shows that the $Al_2O_3$ catalyst coated with Pd and Au is active at temperatures as low as 20 °C. The second best performing was Pt loaded on $TiO_2$, 24 °C, this catalyst was then tested again to determine if there was any degradation in performance and although there is a slight loss in activity light off activation temperature for the catalyst is still below 70 °C. Pd/Au on $TiO_2$ is the third best performing material which sees 100% conversion at 85 °C. Interestingly the $TiO_2$ substrate that was only coated with Au out performs many of the other Pd/Pt materials with an initial conversion of 83% recorded at 50 °C. The activity in relation to gold on metal oxide supports has been well documented with Au nano-particles working in the same way as more common PGM's Pd and Pt.[127,128,129,130] All materials, including HAp demonstrated excellent activity for the catalytic combustion of CO. Catalysts synthesised with the addition of $CeO_2$ were prepared to demonstrate the redox cyclic properties and oxygen storage capacities (OSC) that have been reported about $CeO_2$.[131,132]There are several factors that influence the OSC of $CeO_2$, for example; the gas being used to reduce, the surface properties of supportive substrates and temperatures introduced are just a few.[133]All the catalysts utilising $CeO_2$ had the PGM's Au and Pd. The relationship between $CeO_2$ and palladium has been demonstrated to work in both the Langmuir Hinshelwood (LH) and the Mars-Van Krevelen (MVK) mechanisms, depending on the crystal structure.[134] As gold and $TiO_2$ showed such excellent activity, $TiO_2$ was incorporated into these materials despite reports that Au-$TiO_2$ is less active than Lanthanide and Fe-gold oxide substrates.[135] $Al_2O_3$ and zeolites are among the most commonly used supports for heterogeneous catalysis, hence the comparison between the two materials.[136] The addition of zirconia was used as it has a stabilising influence when used in conjunction with $CeO_2$ and increases surface area.[137,138,139] Despite the reported improvements of $CeO_2$ and zirconia when used for heterogeneous catalysis, the results in figure 60 show a decrease in activity. This is due to the low temperature the conversion from CO to $CO_2$

is achieved and a reduction in surface area observed by incorporating $CeO_2$ in to the catalytic material. However, at higher temperatures and therefore different oxidative reactions $CeO_2$ plays a crucial role.

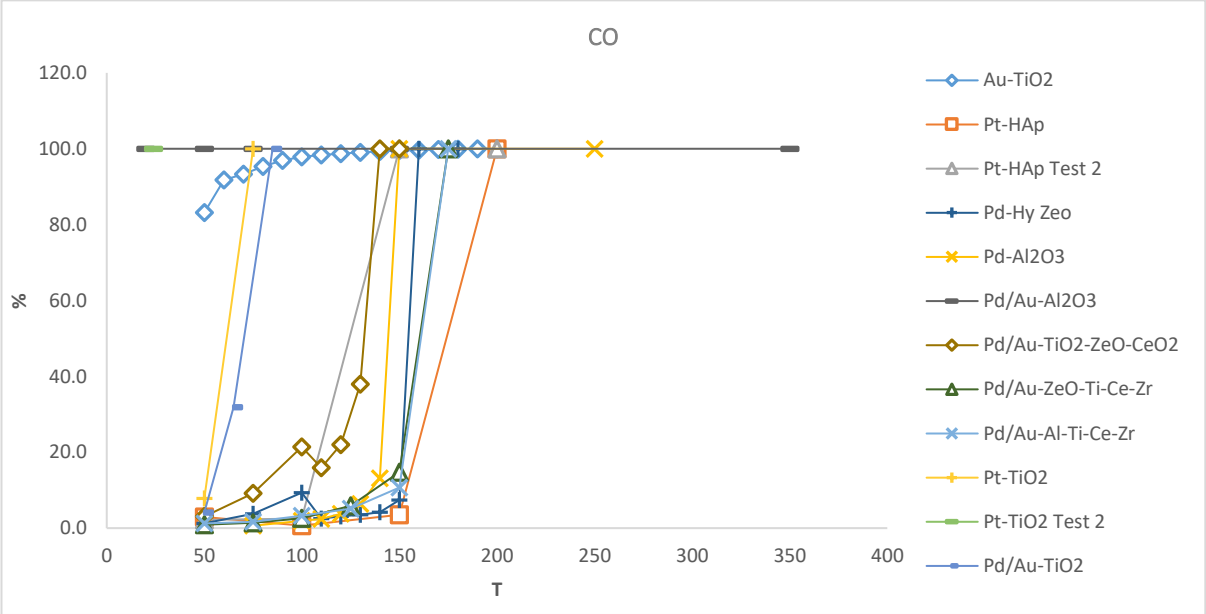


Figure 60 Temperature vs Conversion Catalyst Data for the Complete Combustion of CO

The chart below figure 61 shows the temperatures at which 10, 50 and 80% conversions were achieved by the catalysts shown in fig 40 above. There is no data for the catalysts that performed at temperatures below 50 °C, this is because they reached over 80% at the initial injection temperature. The chart clearly demonstrates that $TiO_2$ is the most active support for the catalytic oxidation of CO. The addition of gold to the Pd- $Al_2O_3$ catalyst has a striking effect on the activity of the catalyst as reported by Haruta et al.[140]

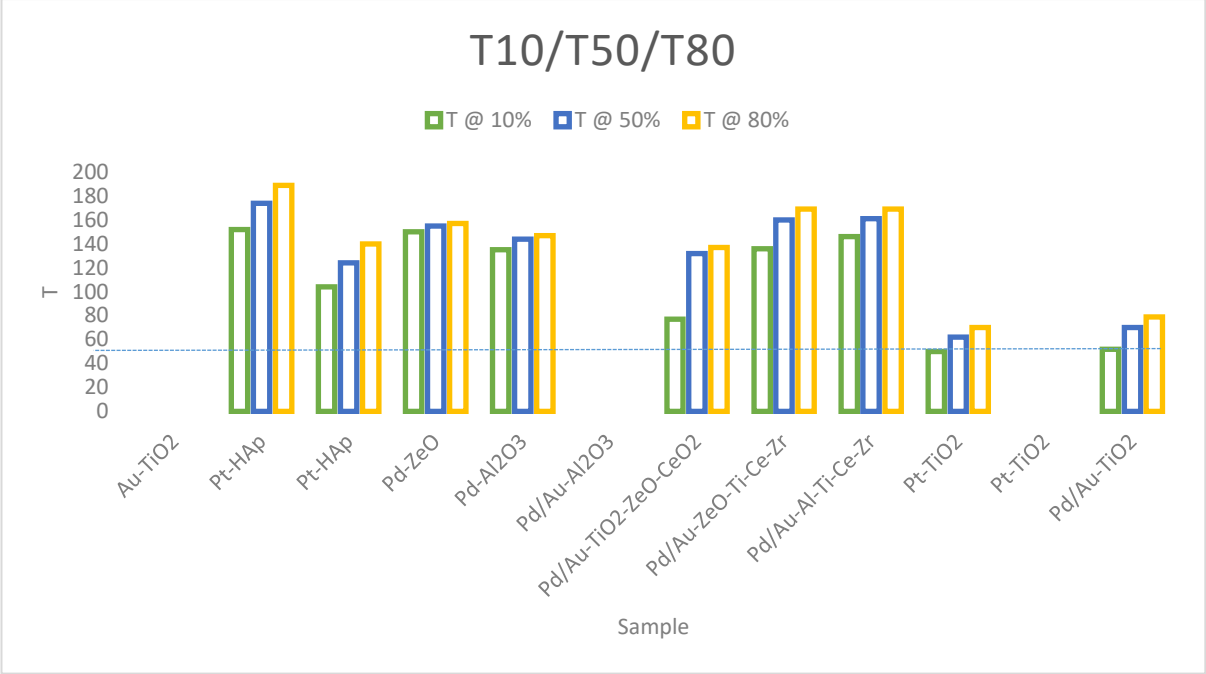


Figure 61 Temperature at which 10, 50 and 80% Conversion is achieved for CO combustion catalysts

### 7.3.2 $CH_4$

Figure 62 shows results for the catalytic complete combustion of $CH_4$, the best overall catalytic material was prepared in a traditional wet synthetic method. It clearly shows that the catalyst that is composed of Pd/Au-$TiO_2$-$CeO_2$-ZeO demonstrates excellent activity for the reaction: $CH_4 +$

$$2O_2 \rightarrow CO_2 + 2H_2O \qquad (21)$$

Literature values for the complete combustion of $CH_4$ are in the range of 600 – 800 °C. The importance of the materials in the figure is that all achieved 100% conversion below 400 °C, the best showing 95% conversion at 270 °C and 100% at 300 °C. A ~50% improvement on what has been achieved before, without the need for complicated core-shell synthesis and matches core-shell at conversion temperatures.[141,142] With the momentum from the CO results obtained and promising with regard to overall CO conversion and the use of chosen supports and precious metal loadings. Figure 62 shows the best of the WI materials prepared. All the catalysts reach 100% conversion between 300 – 400 °C. Single PGM and single support catalysts gave excellent conversions especially at T10% giving the best light off conversions, however, as Au has an important role in CO conversion it was decided to leave gold in moving forward. The combination

of $TiO_2$/ZeO/$CeO_2$ supporting Pd and Au was successful, the concentration of the metal salt solutions was varied to determine the most active. It was quickly discovered that a Pd salt concentration of 0.005 M giving a Pd loading between 2-8% proved to give the best results. By making Au salts at concentrations from 0.002 M to 0.006 M. The Pd-Au/$TiO_2$/$CeO_2$/Zeo1 (0.002 M) had the lowest concentration of gold, Pd-Au/$TiO_2$/$CeO_2$/Zeo* (0.004 M) and Pd-Au/$TiO_2$/$CeO_2$/Zeo** (0.006 M). The lower Au salt concentration, thus loading proved to be the best. The role of Pd over Pt and Rh is well documented for the abatement of $CH_4$.[143] Pd is oxidised to PdO during the process of $CH_4$ oxidation and it is important as the Pd oxide form is what drives the combustion of mehane.[144,145] The oxide support is also crucial in the process, this is why the Pd – zeolite and Pd – HAp/zeolite catalysts did not perform as well. The quick uptake of oxygen by $CeO_2$ also drives the combustion process.[146] By slowing down the oxidation of Pd catalytically active Pd adsorbs chemically stable $CH_4$ then $Ce^{+4}$ is reduced to $Ce^{+3}$ as it gives up oxygen to oxidise $CH_4$ to $CO_2$.[147,148,149]In conjunction with the OSC of $CeO_2$ the redox cyclic properties of $CeO_2$ and Pd the added surface area that is gained by using materials such as Y-zeolite, $Al_2O_3$ and $TiO_2$ all play a crucial role in heterogeneous catalysis.[150,151]

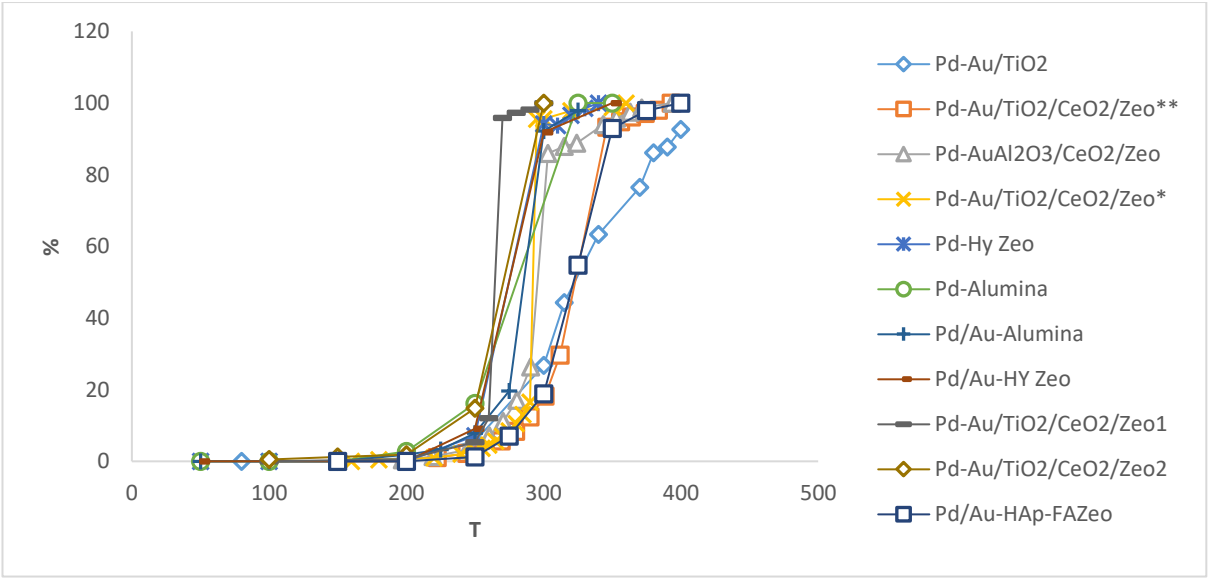


Figure 62 Low Temperature Complete Combustion of $CH_4$

The chart below shows the temperatures at which 10, 50 and 80% conversions were achieved. It is clear that $CeO_2$ plays an important role in the catalytic oxidation of $CH_4$, especially when used in conjunction with $TiO_2$ and zeolite Y. The chart figure 63 shows the light off or T10% it is clear that Pd-$Al_2O_3$ and Pd-Au/$TiO_2$/$CeO_2$/Zeo1 have the lowest recorded temperatures, however the T80% for the Pd-$Al_2O_3$ is higher than the T80% for Pd-Au/$TiO_2$/$CeO_2$/Zeo1 by 39 °C. Encouraging is the difference between the first and second test for the catalyst Pd-Au/$TiO_2$/$CeO_2$/Zeo1-2 as there is very little loss in activity and light off temperature.[152]

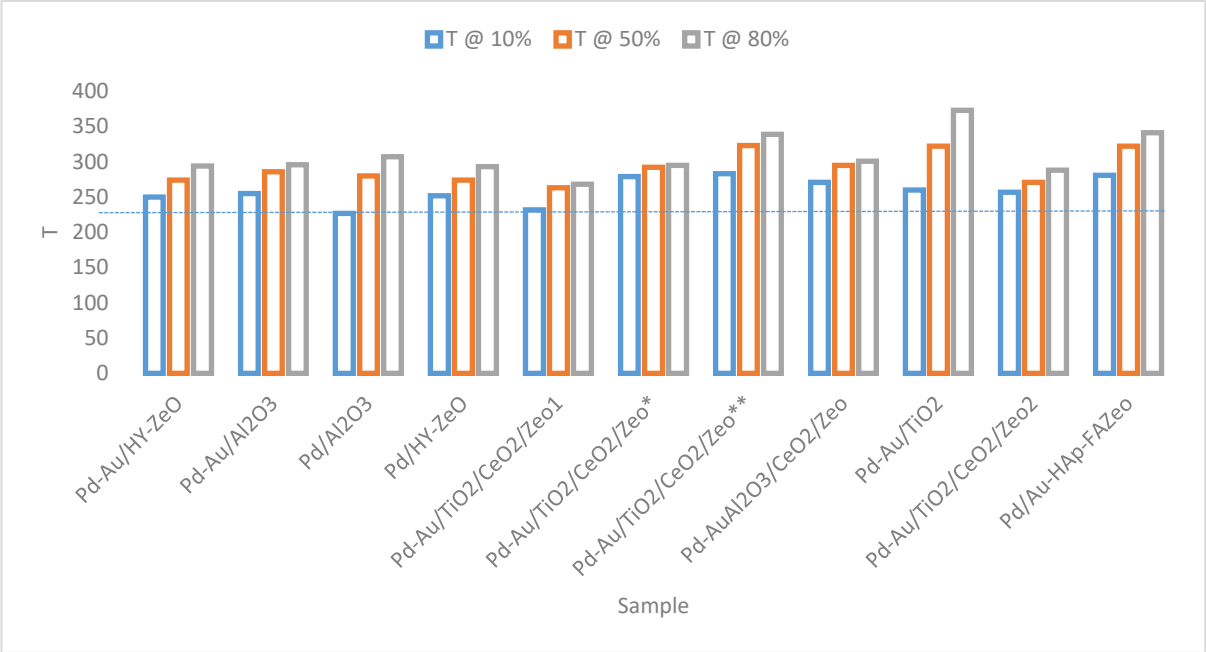


Figure 63 Low Temperature at which 10, 50 and 80% conversion is achieved for the combustion of $CH_4$

The activation energy plot below shows that the $E_a$ for the reaction of $CH_4$ with oxygen is well within the range that has been well recorded in literature.[153] The concentrations of reactants and products is roughly the same at low conversions. Consequently, the initial reaction rate is approximately proportional to the reactant conversion. This, coupled with no side reactions enables approximate activation energies to be calculated by plotting 1/T against ln conversion %.[154]

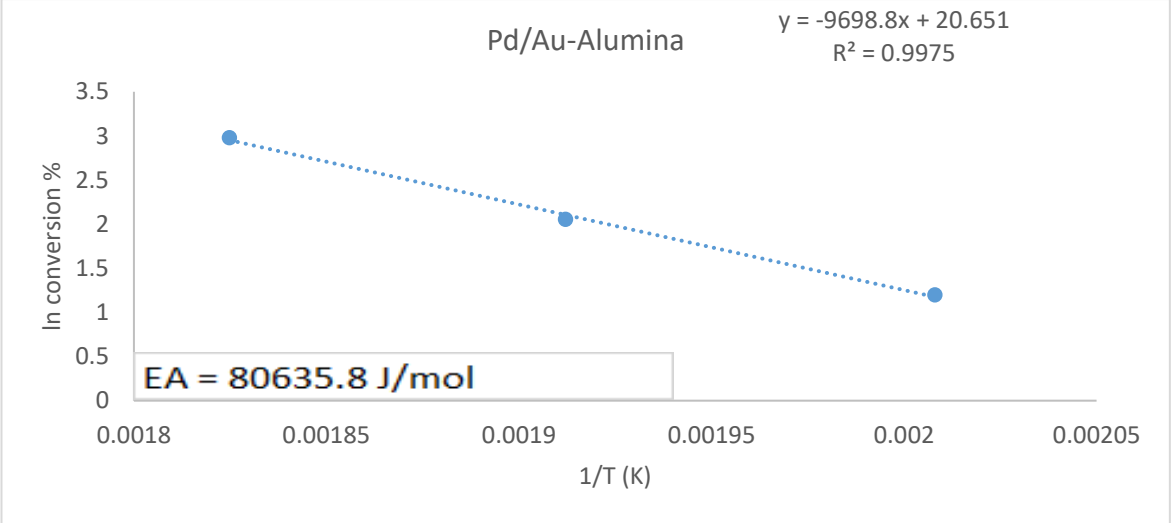


Figure 64 Activation Energy for the complete combustion of $CH_4$ with a Pd/Au- $Al_2O_3$ catalyst

### 7.3.3 Conclusions

A series of precious metal catalysts was prepared for the complete oxidation of CO and $CH_4$. In order to create well dispersed materials, thus increasing activity. PGM salts were sonicated to achieve smaller particle sizes and better coverage of substrate materials. All catalytic materials reported for the complete combustion of CO proved to be fully active below 200 °C, with Pd/Au-$Al_2O_3$ and Pt-$TiO_2$ recording 100% conversion at room temperature. Gold, as previously reported, proved to show high activity on its own as demonstrated with the Au-$TiO_2$ catalyst recording 80% conversion at 50 °C. PGM wt% data showed all prepared materials had a Pd/Pt wt% in the range of 1-12% and a gold wt% ranging from 0.3 – 6% for the materials tested. The successful low temperature full oxidation of $CH_4$ was achieved by utilising iterative catalyst synthesis based on catalytic tests. Catalyst Pd-Au/$TiO_2$/$CeO_2$/Zeo1 recorded 95% conversion at 270 °C and reached 100% by 300 °C. The low temperature conversion was achieved by using a combination of high surface area supports, well dispersed nanoparticles of precious PGM's and percentage loading of PGM's in the ranges of 1-12%.

## 7.4 Magnetron Sputtered Samples

**Table 10 Magnetron sputtered XRF and Surface area data**

| Sample name | Metal | Support | Pd % | Au % | Ce % | Ti % | Al % | Si % | $CeO_2$ % | Surface Area $m^2 g^{-1}$ |
|---|---|---|---|---|---|---|---|---|---|---|
| **Pd/Au-$TiO_2$ (15MAG)** | Pd/Au | $TiO_2$ | 7.18 | 0.06 | × | 75.0 | × | × | × | 61.37 |
| **Pd/Au-TiO2-$CeO_2$ (15MAG)** | Pd/Au | $TiO_2$ - $CeO_2$ | 6.4 | 0.01 | 3.19 | 58.0 | × | × | 3.1 | 73.14 |
| **Pd/Au-$Al_2O_3$ (15MAG)** | Pd/Au | $Al_2O_3$ | 1.66 | 0.02 | × | × | 48.1 | × | × | 131.24 |
| **Pd/Au-$Al_2O_3$-$CeO_2$ (15MAG)** | Pd/Au | $Al_2O_3$ - $CeO_2$ | 2.82 | 0.01 | 1.67 | × | 45.5 | × | 2.1 | 135.52 |
| **Pd/Au-ZeO (15MAG)** | Pd/Au | ZeO | 5.26 | 0.01 | × | × | 2.77 | 43.5 | × | 634.54 |
| **Pd/Au-ZeO-$CeO_2$ (15MAG)** | Pd/Au | ZeO - $CeO_2$ | 2.58 | 0.01 | 1.20 | × | 2.52 | 39.9 | 1.5 | 902.18 |
| **Pd-$TiO_2$ (15MAG)** | Pd | $TiO_2$ | 4.78 | × | × | 57.4 | × | × | × | 116.60 |
| **Pd-ZeO (15MAG)** | Pd | ZeO | 2.74 | × | × | × | 3.01 | 46.7 | × | 743.10 |
| **Pd-$Al_2O_3$ (15MAG)** | Pd | $Al_2O_3$ | 1.04 | × | × | × | 45.5 | × | × | 112.48 |
| **Pd/Au-$TiO_2$ (10MAG)** | Pd/Au | $TiO_2$ | 0.96 | 0.01 | × | 52.2 | × | × | × | 52.95 |
| **Pd/Au-TiO2-$CeO_2$ (10MAG)** | Pd/Au | $TiO_2$ - $CeO_2$ | 1.42 | 0.02 | 0.52 | 48.8 | × | × | 0.6 | 38.67 |
| **Pd/Au-$Al_2O_3$ (10MAG)** | Pd/Au | $Al_2O_3$ | 0.72 | 0.02 | × | × | 51.6 | × | × | 139.57 |
| **Pd/Au-$Al_2O_3$-$CeO_2$ (10MAG)** | Pd/Au | $Al_2O_3$ - $CeO_2$ | 0.57 | 0.01 | 0.31 | × | 48.9 | × | 0.4 | 131.70 |
| **Pd/Au-ZeO (10MAG)** | Pd/Au | ZeO | 1.02 | 0.02 | × | × | 2.77 | 43.4 | × | 130.44 |

| | | | | | | | | | | |
|---|---|---|---|---|---|---|---|---|---|---|
| **Pd/Au-ZeO-$CeO_2$ (10MAG)** | Pd/Au | ZeO - $CeO_2$ | 1.00 | 0.01 | 0.23 | × | 2.48 | 40.1 | 0.3 | 622.81 |
| **Pd-$TiO_2$ (10MAG)** | Pd | $TiO_2$ | 3.62 | × | × | 58.2 | × | × | × | 77.93 |
| **Pd-ZeO (10MAG)** | Pd | ZeO | 1.66 | × | × | × | 2.81 | 45.2 | × | 730.37 |
| **Pd-$Al_2O_3$ (10MAG)** | Pd | $Al_2O_3$ | 0.58 | × | × | × | 33.5 | × | × | 146.03 |
| **Pd/Au-$TiO_2$ (20MAG)** | Pd/Au | $TiO_2$ | 1.94 | 0.01 | × | 47.1 | × | × | × | 60.42 |
| **Pd/Au-TiO2-$CeO_2$ (20MAG)** | Pd/Au | $TiO_2$ - $CeO_2$ | 2.12 | 0.02 | 0.60 | 50.5 | × | × | 0.7 | 58.58 |
| **Pd/Au-$Al_2O_3$ (20MAG)** | Pd/Au | $Al_2O_3$ | 2.14 | 0.02 | × | × | 50.8 | × | × | 139.36 |
| **Pd/Au-$Al_2O_3$-$CeO_2$ (20MAG)** | Pd/Au | $Al_2O_3$ - $CeO_2$ | 2.43 | 0.02 | 0.46 | × | 45.2 | × | 0.6 | 137.16 |
| **Pd/Au-ZeO (20MAG)** | Pd/Au | ZeO | 1.29 | 0.02 | × | × | 2.76 | 44.2 | × | 734.64 |
| **Pd/Au-ZeO-$CeO_2$ (20MAG)** | Pd/Au | ZeO - $CeO_2$ | 2.73 | 0.02 | 0.32 | × | 2.63 | 42.3 | 0.4 | 702.97 |
| **Pd-$TiO_2$ (20MAG)** | Pd | $TiO_2$ | 7.36 | × | × | 57.6 | × | × | × | 80.44 |
| **Pd-ZeO (20MAG)** | Pd | ZeO | 3.04 | × | × | × | 2.86 | 45.9 | × | 734.93 |
| **Pd-$Al_2O_3$ (20MAG)** | Pd | $Al_2O_3$ | 1.48 | × | × | × | 38.9 | × | × | 143.38 |

The data in the table shows the type of support and the precious metal it has been coated with and the time the samples were under the Pd target.The samples ending (10MAG), were under the Pd-sputter target for 10 minutes, (15MAG), 15 minutes and (20MAG), 20 minutes. All Au loading was done *via* wet chemical process explained in the experimental chapter. The samples that are composed of $TiO_2$ have been more susceptible to accepting atoms from the Pd target than the samples composed of $Al_2O_3$, this is not surprising when you consider the electrical properties of

the two materials. $Al_2O_3$ is used for its resistive electronic properties to insulate superconductive materials; $TiO_2$ however, has excellent conductive properties. The anatase form is considerably more thermally stable and as such is used in organic light emitting diodes as it facilitates in charge transfers and electrical injection. Recently Marinel et al[155] reported dielectric properties of $TiO_2$ ceramics conventionally and microwave sintered at the temperatures above 1000–1300°C.[156] The dielectric constant values were high and equal about $k$ ~ 100 for measurement performed at RT and at the frequency of 100 Hz.[157] These high values were achieved by preparation of high-density ceramic sinters; however, the morphology of the sinters precludes their use as fine-grained fillers in hybrid dielectrics. It is however, these qualities that have driven the increased accumulation of sputtered species to adsorb onto the $TiO_2$ substrate. As dielectrics albeit act as insulators, they allow the flow of charge when an external electric field is applied.[158] In the samples that were subjected to 10 and 20 minutes under the Pd target, there is a definite contrast in comparison to the 15 minute samples, with regard to the $TiO_2$-Pd and the $TiO_2$-Pd/Au. For the 10 and 20 minute coated samples there is a definite increase in Pd wt% for the $TiO_2$-Pd/Au catalysts over the $TiO_2$-Pd materials that is not observed in the 15 minute deposition rate.

### 7.4.1 Conversion Data for Magnetron Sputtered Samples for the Complete Oxidation of CO and $CH_4$

### 7.4.2 $TiO_2$

The curves below demonstrate the catalytic activity for $TiO_2$ samples that were under physical vapour deposition for 15, 10 and 20 minutes respectively. The sample names are explained in the table 10 above. The best overall catalyst is the $TiO_2$ only substrate that was under deposition for 20 minutes. The potential reason for this was described above as this is the sample with the highest Pd wt%. The key take home with all the $TiO_2$ samples, whether they are just $TiO_2$ or also composed of Au and or $CeO_2$ and Au is that they all demonstrated 100% conversion below 200 °C, several below 100 °C. This is important for the use as automotive catalysts as exhaust running temperatures range between 100 – 400 °C depending on vehicle load and speed. A prolific search

for papers that have used the PVD process of magnetron sputtering on varying supports for the oxidation reactions of CO and $CH_4$ turned up no direct matches. However, the use of $TiO_2$ as a support with promoters including $CeO_2$ is well documented. Huaqing Zhu *et al.* reported $TiO_2$ and $TiO_2$- $CeO_2$ materials with complete CO conversion temperatures, but not at temperatures as low as <200 °C.[159] Conversely when prepared *via* a sol gel and WI method Huaqing Zhu *et al.* aslo reported conversion temperatures in the same ranges as demonstrated in figure 65.[160]

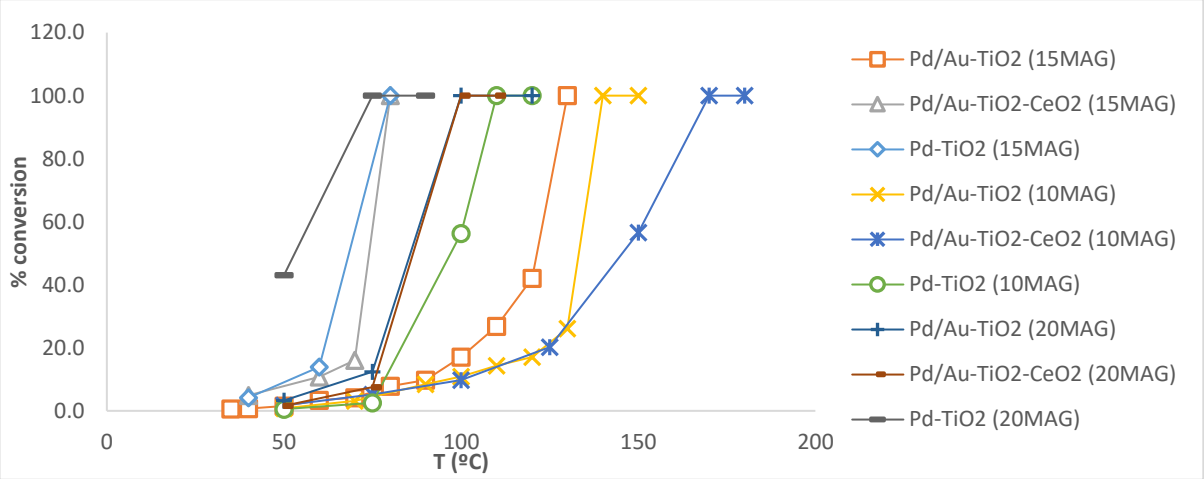


Figure 65 $TiO_2$ - Pd magnetron sputtered cats for the combustion of CO 10, 15 and 20 minute deposition rates

The chart below shows conversion of CO to less harmful $CO_2$ at temperatures related to 10, 15 and 20 minutes. The chart demonstrates a clear link between a pure $TiO_2$ support and just Pd loading as having the lowest T10% for all the samples, Pd-$TiO_2$ (15MAG) and Pd-$TiO_2$ (20MAG) respectively. It is clear from table 5 that these two samples were also the ones with the highest Pd wt% the reason for the extra Pd loading has been previously examined. Samples Pd/Au-$TiO_2$-$CeO_2$ (15MAG) has a light off or T10% conversion temperature of 57 °C and is also a sample with a higher Pd wt%. Interestingly though Pd/Au-$TiO_2$ (20MAG) with a Pd wt% of only 1.94% is the next best performing catalyst. In contrast to the WI prepared catalysts, all the single precious metal catalysts independent of deposition rate out-performed the materials containing $CeO_2$ and Au. Despite the widely reported enhancing effects of $CeO_2$ on noble metal materials.[161,162,163,164]

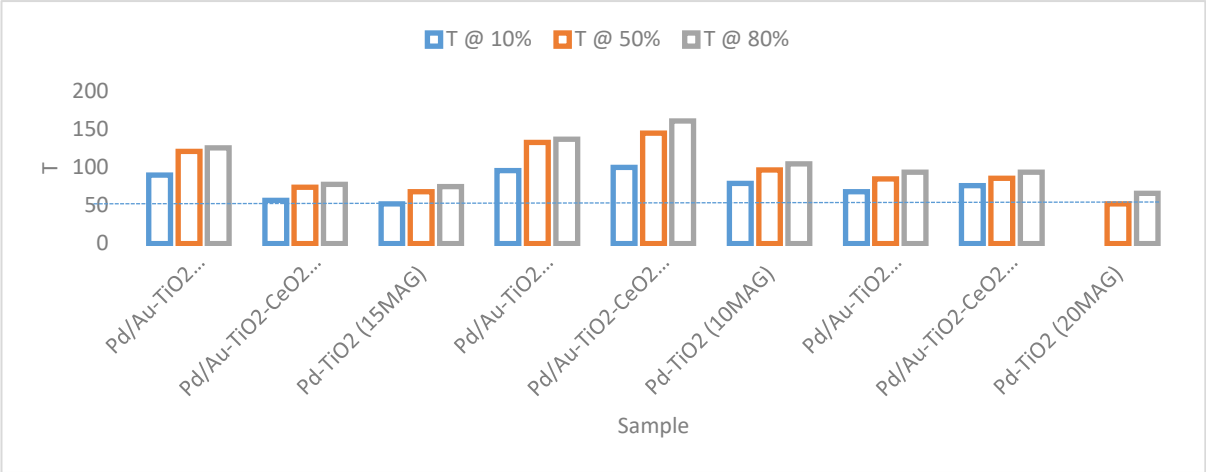


Figure 66 Temperature at which 10, 50 and 80% conversion is achieved for 10, 15 and 20 minute deposition rates

The activation energy plot below shows that the $E_a$ for the reaction of CO with oxygen is well within the range that has been well recorded in literature.[165]

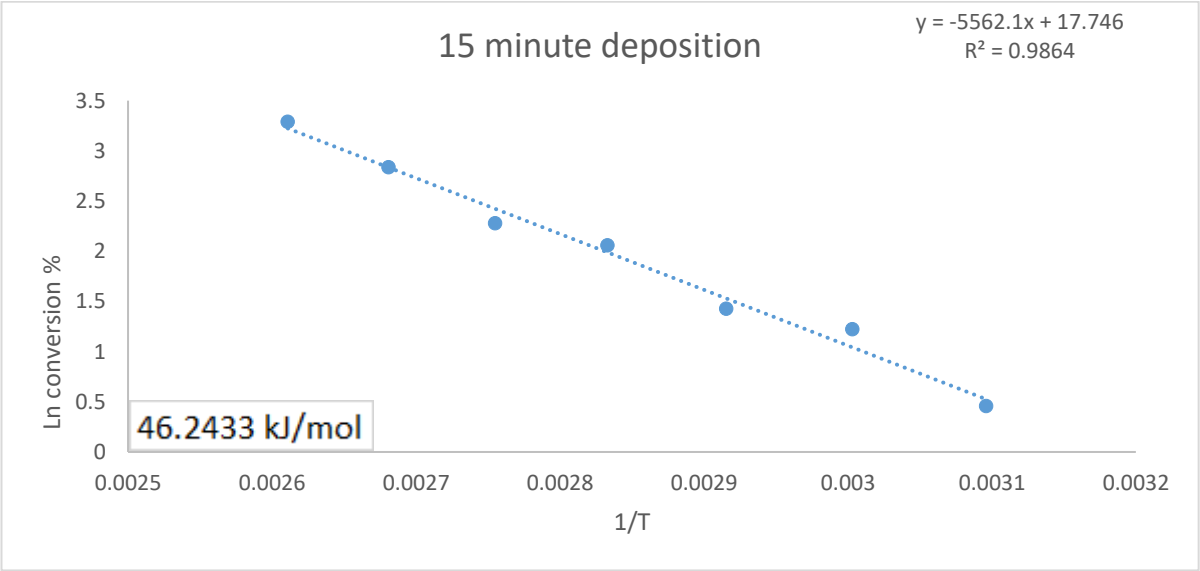


Figure 67 Activation Energy for $TiO_2$/Au-Pd magnetron sputtered catalyst, 15 minute deposition rate

### 7.4.3 Y-Zeolite

Figure 68 shows the conversion curves for the complete oxidation of CO over Y-Zeolite prepared catalytic materials. The best performing material was the zeolite that was coated in the laboratory with a Au salt in a traditional wet synthetic process described previously. It was then subject to a 15 minute deposition rate under a Pd target. All of the prepared catalysts reached 100% conversion between 195-225 °C, only 35 °C separating the most active from the least, thus a tight

group. None of the zeolite materials performed particularly well in comparison to the $TiO_2$ based materials, Pd loading was reduced in comparison to $TiO_2$, see table 5, however it was still higher than the best performing $TiO_2$ sample which had a Pd wt% of 1.94 compared to the best zeolite material which had a wt% of 5.26. It is well documented that the oxidation of CO on palladium catalysts is predominantly LH and ER.[166,167] The surface area of the zeolite support is significantly increased in comparison to both $Al_2O_3$ and $TiO_2$, this would suggest that the activity of the zeolite catalysts should be greater than other supports. However, as this is not observed, it would suggest that the oxide support plays a greater role than previously thought. As $CeO_2$ utilises a dual functional LH pathway, there is evidence to suggest that oxides react in a similar way.[168]

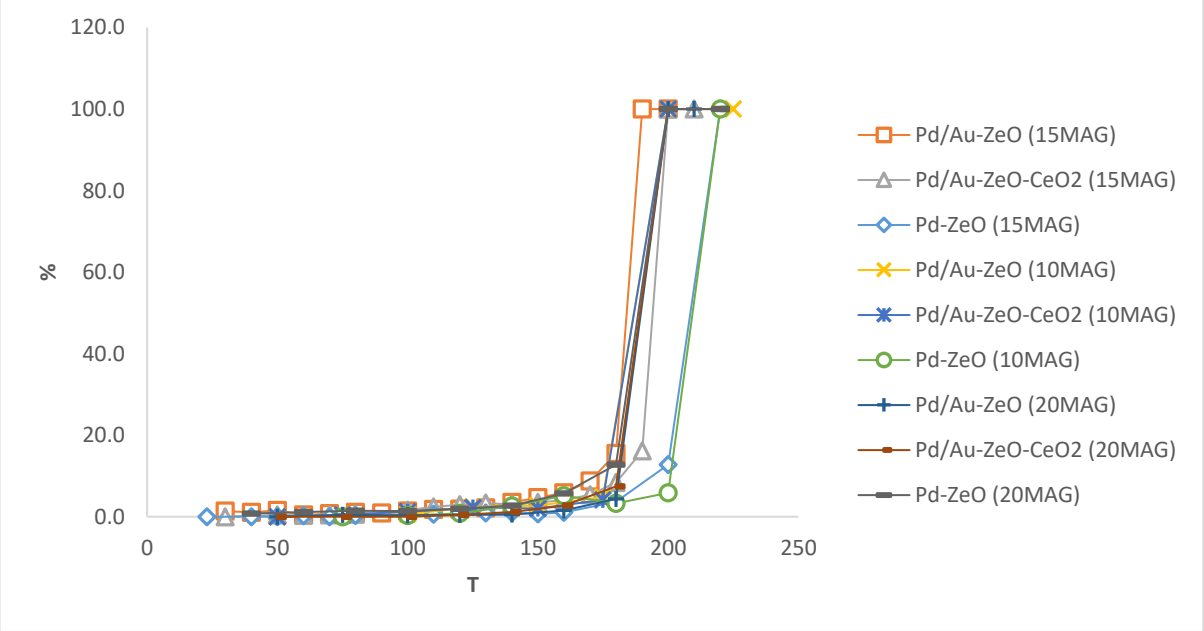


Figure 68 HY-ZeO – Pd magnetron sputtered catalyst light off curves for the combustion of CO 10, 15 and 20 deposition rates

The chart below shows the temperature at which 10, 50 and 80% conversions were achieved. The samples are very close in conversion rates and as the conversion data and T10 –T80% demonstrates, they behave in a similar way at lower temperatures. There is a 20 °C difference in temperature across all the T10% light off curves, but this pattern is repeated across the T50 and T80%. This might suggest that when used as a support zeolites do not manifest any promotional effects and in fact palladium and the LH single mechanistic pathway is prevalent.[169]

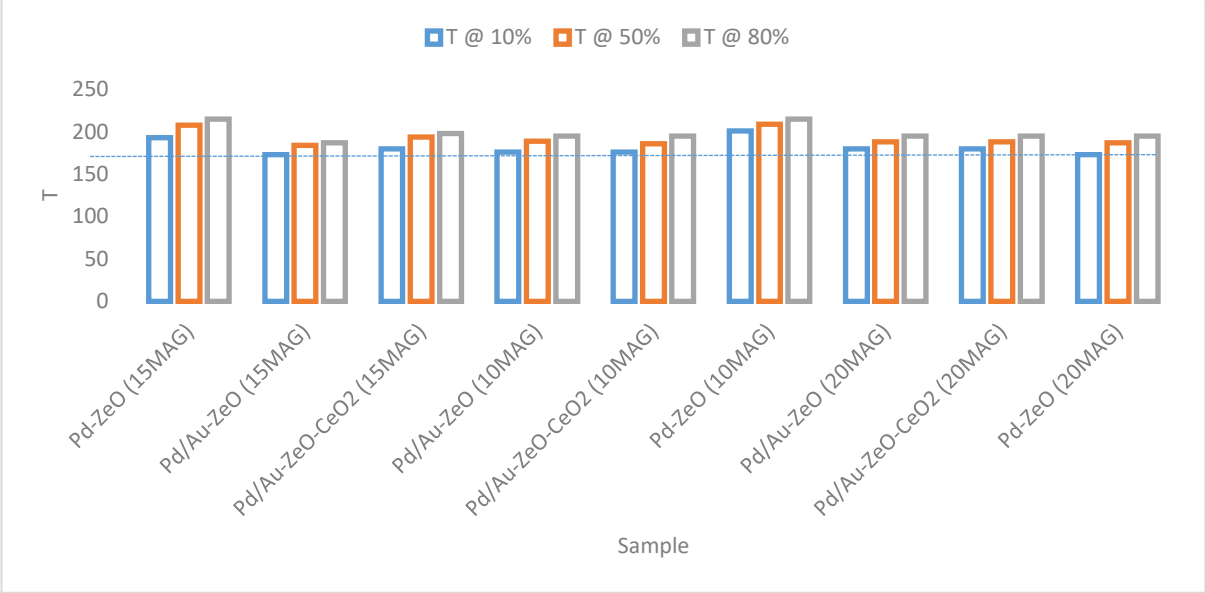


Figure 69 Temperature at which 10, 50 and 80% conversion is achieved for 10, 15 and 20 minute deposition rates

The activation energy plot below shows that the $E_a$ for the reaction of CO with oxygen is well within the range that has been well recorded in literature.[170]

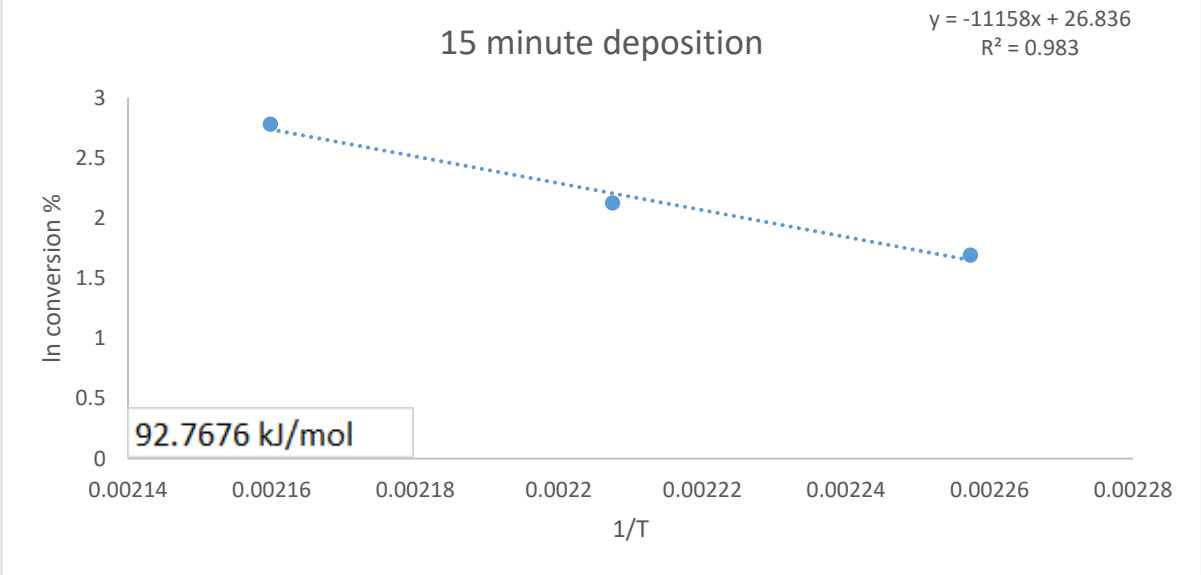


Figure 70 Activation Energy for HY-ZeO/$CeO_2$/Au-Pd magnetron sputtered catalyst, 15 minute deposition rate

### 7.4.4 $Al_2O_3$

Figure 71 shows the conversion curves for the complete oxidation of CO over $Al_2O_3$ prepared catalytic materials. The $Al_2O_3$ samples also demonstrate a tight group, this time with only 30 °C separating 100% conversion. The best performing catalysts; the materials Pd/Au-$Al_2O_3$ (15MAG), Pd/Au-$Al_2O_3$-$CeO_2$ (15MAG) and Pd/Au-$Al_2O_3$ (20MAG). These catalysts have similar Pd wt% in the range of 1.66 to 2.82. In a study by Katrin Zorn *et al* the reactivity of Pd and PdO on $Al_2O_3$ was

investigated and determined that the reductive properties of CO on Pd show that it is Pd and not it's oxide that are responsible for the combustion of CO.[171]Under the reaction conditions as previously described, it would hint that whilst oxygen is oxidising the catalyst CO reduces it under the flow of both gases, thus maintaining a predominantly metal core.

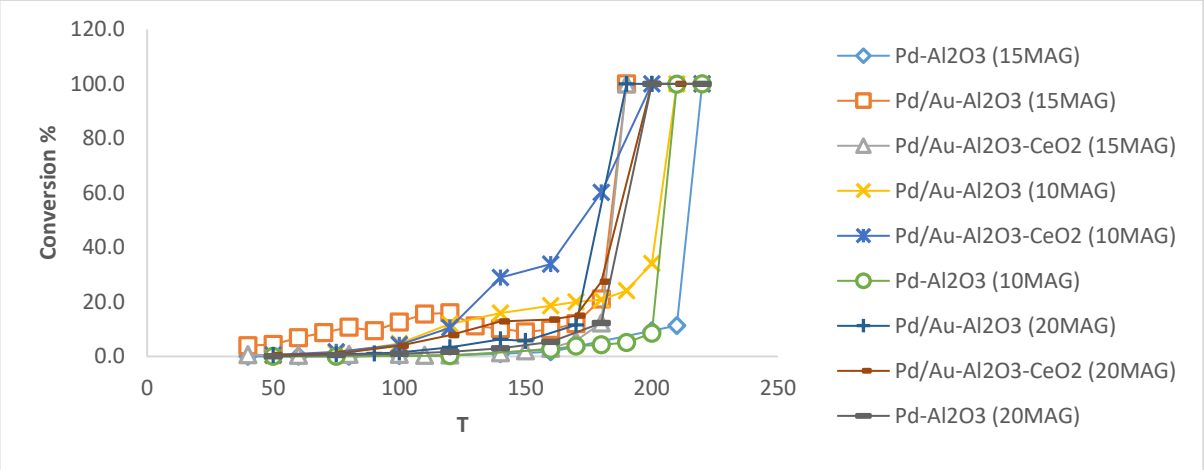


Figure 71 $Al_2O_3$ - Pd magnetron sputtered catalyst light off curves for the combustion of CO 10, 15 and 20 deposition rates

Figure 72 illustrates that it is in fact Pd/Au-$Al_2O_3$ (10MAG) and Pd/Au-$Al_2O_3$-$CeO_2$ (10MAG) respectively that reach T10% conversion at a lower temperature than the other catalytic materials by ~45 °C. This might suggest that at initial low temperatures the addition of gold nano-particles and $CeO_2$ are having a favourable effect on the reaction between CO and oxygen.[172] This early low temperature activity is not carried through when you look at the T50% and T80% conversion data. The lowest T10% demonstrated by the Pd/Au-$Al_2O_3$ has the third highest T50%. Unlike the zeolite catalysts which climb rapidly through T10 - T100% conversion, there is a shallow ascent for the three catalysts with the lowest T10%. These catalysts have incomparable Pd wt% with the 10 minute deposited materials having less than 1% and the 20 minute deposited catalyst having a Pd loading greater than 2%.

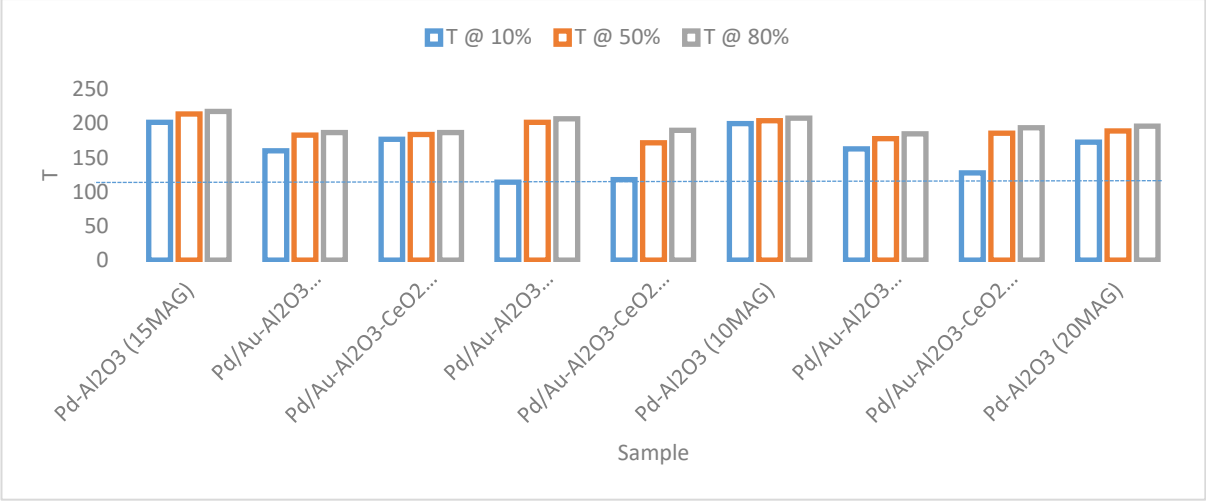


Figure 72 Temperature at which 10, 50 and 80% conversion is achieved for 10, 15 and 20 minute deposition rates

The activation energy plot below shows that the $E_a$ for the reaction of CO with oxygen is well within the range that has been well recorded in literature.[173]

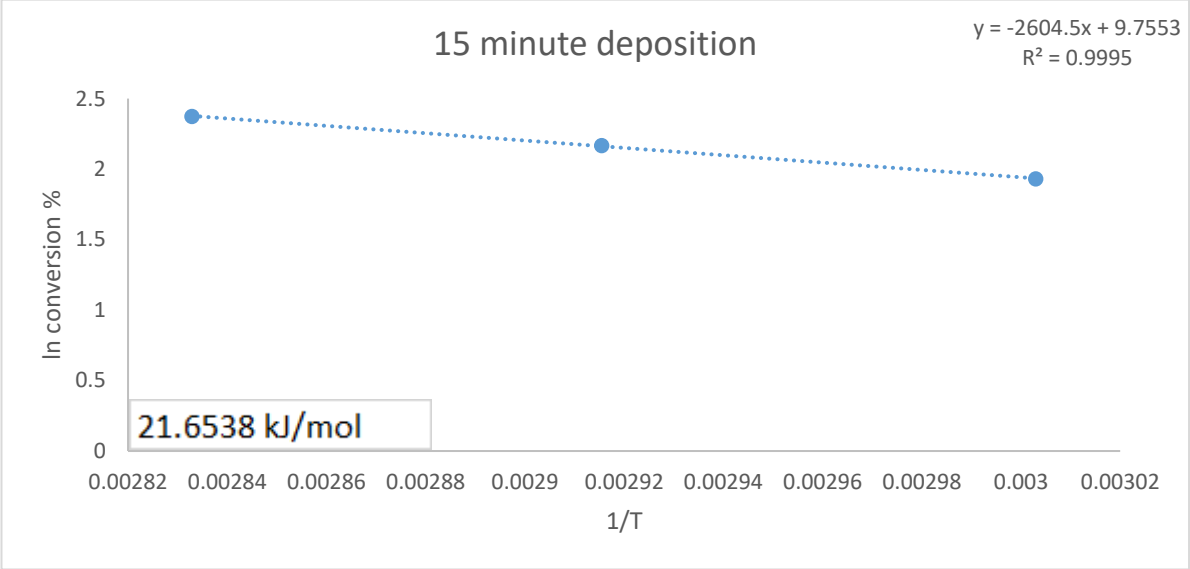


Figure 73 Activation Energy for $Al_2O_3$/Au-Pd magnetron sputtered catalyst, 15 minute deposition rate

### 7.4.5 $CH_4$ Oxidation over $TiO_2$ catalysts

Figure 74 shows a series of light off curves for the $TiO_2$ substrate magnetron sputtered with palladium catalysts that were under the target for 10, 15 and 20 minutes. In some instances, gold was added to the substrate supports prior to PVD as was $CeO_2$. Previously demonstrated was $TiO_2$ coated via magnetron was superior for the complete combustion of CO. The following data analyses the single support in its role in the complete combustion of $CH_4$. All catalysts reached

100% conversion to $CO_2$ before 550 °C the lowest being 380 °C with Pd/Au-$TiO_2$(15MAG). This has important implications for the designed use as dual-fuel diesel/natural gas automotive catalytic converter material. Lara S. Escandon *et al* reported that Pd wt% of 0.90 producing a conversion of ~70% at 525 °C.[174] In comparison the Pd wt% for the most active catalyst in figure 74 is 7.18, however the Pd/Au-$TiO_2$(10MAG) has a Pd wt% of 0.96 and reached 100% conversion at 475 °C. This is partly due to the increased dispersion achieved using the magnetron and the small particle size in some cases as low 2 nm that is a direct result from sputtering single atoms onto the substrate.[175]

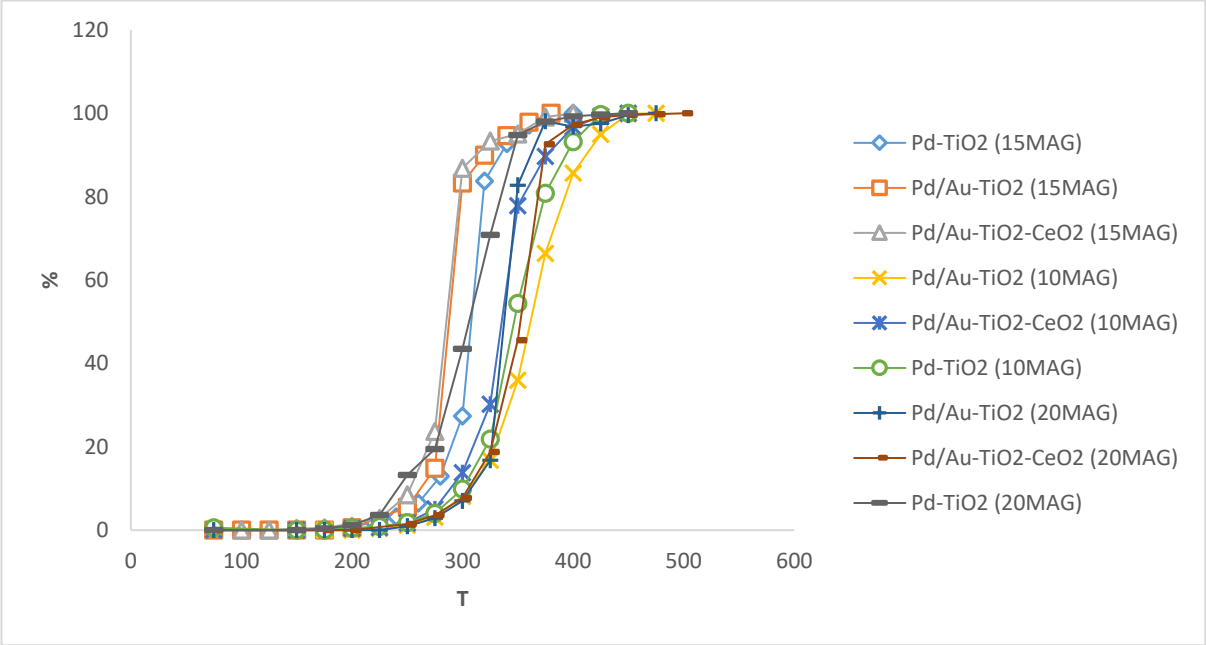


Figure 74 $TiO_2$ - Pd magnetron sputtered catalyst light off curves for the combustion of $CH_4$ 10, 15 and 20 deposition rates

Figure 75 highlights the temperatures at which 10, 50 and 80% conversion was achieved. $TiO_2$ proved to be an excellent support for the complete combustion of $CH_4$, as previously discussed the higher wt% of palladium deposited on to the support coupled with the high dispersion over the substrate enabled 80% conversion temperatures all below 400 °C.[176] In comparison to the other supports $TiO_2$ has the lowest T10%, but notably it has the steepest ascent from light off to 100% conversion. There is an obvious correlation between Pd loading and activity, especially when analysing the T10% for the different deposition rates. With the samples under the target for

10 minutes, the promoting effect of $CeO_2$ counter acts the reduced Pd loading.[177,178,179] This effect is prominent in the 15 minute samples too, yet not with the higher Pd loading seen on the 20 minute samples.[180,181]

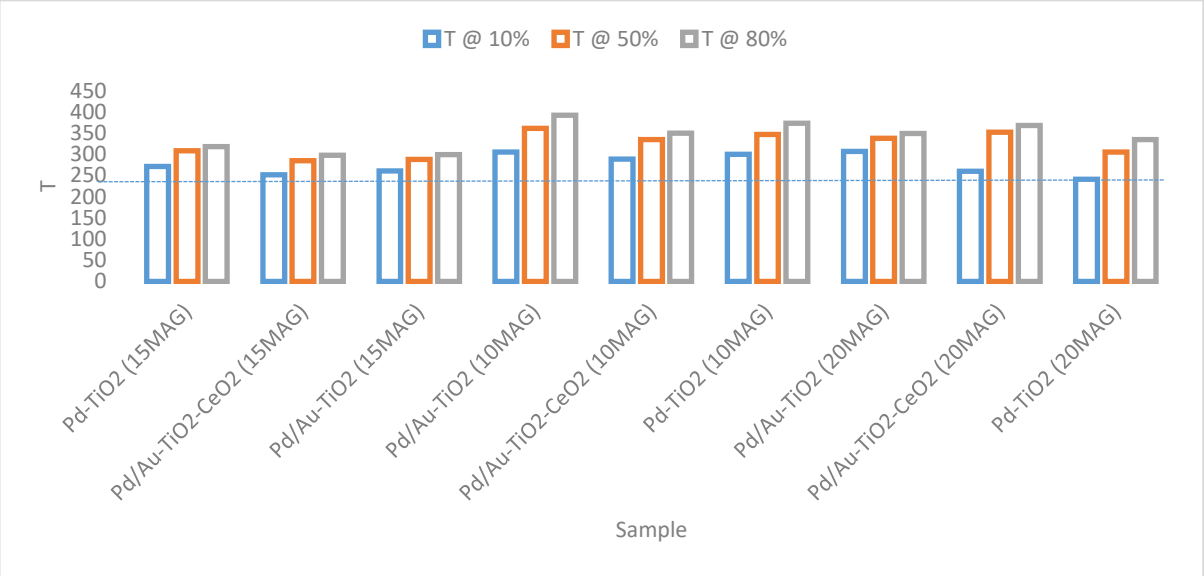


Figure 75 Temperature at which 10, 50 and 80% conversion is achieved for 10, 15 and 20 minute deposition rates

The activation energy plot below shows that the $E_a$ for the reaction of $CH_4$ with oxygen is well within the range that has been well recorded in literature.[182]

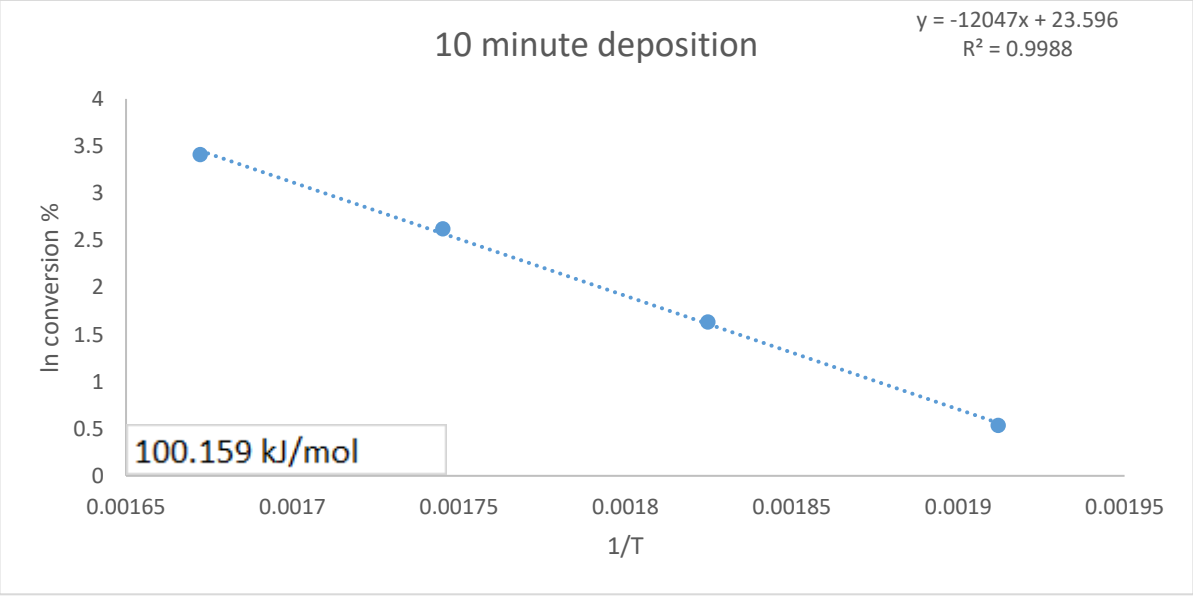


Figure 76 Activation Energy for $TiO_2/CeO_2$/Au-Pd magnetron sputtered catalyst, 10 minute deposition rate

Figure 77 illustrates the effectiveness of zeolite supports, notably 5 catalysts reached 100% conversion before or at 400 °C and all by 475 °C. In a nature publication A W Petrov *et al.*

demonstrated the effectiveness of Pd noble metal zeolite catalysts for the complete oxidation of $CH_4$. [183] Petrov et al reported conversion temperatures < 550 °C and similar to the temperatures reported herein. They also reported the stabilising effect of zeolite supported Pd nano-particles and the encapsulating properties of the highly porous material to improve longevity and prevent sintering. [184, 185,186] Figure 77 shows that even without the promoting effects of $CeO_2$ Pd-ZeO (15MAG) and (20MAG) were able to reach 100% conversion close to 300 °C, with the Pd-ZeO(20MAG) catalyst recording a 93% conversion at 300 °C similar to those recorded by Montes de Correa et al, but at an increased $CH_4$ flow rate as outlined previously.[187] It has been reported that the increased activity and stability of zeolite supports is due to the hydrophobicity.[188,189] Petrov et al also reported the difficulty in dispersing Pd effectively into the porous zeolite materials.[190] This is where the PVD has an edge on conventional wet chemistry, be it ion exchange (IE), wet impregnation (WI) or incipient wetness (IW). By sputtering single atoms onto a zeolite, effectively placing Pd into the pores and onto the immediate or outer surface.

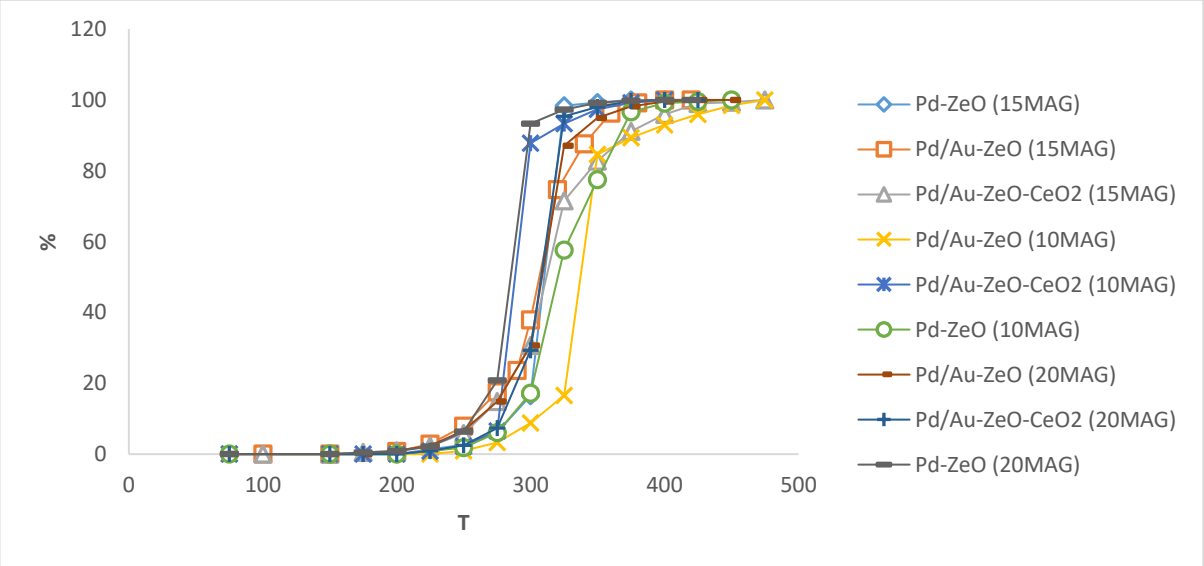


Figure 77 HY-ZeO - Pd magnetron sputtered catalyst light off curves for the combustion of $CH_4$ 10, 15 and 20 deposition rates

Figure 78 depicts the T10, 50 and 80%, as before there is a direct correlation with Pd wt% loading and light off temperatures for the materials coated *via* PVD. The promotive effect of $CeO_2$ with the reduced Pd loaded 10 minute samples is again prominent and the steepest ascent from T10%

to full conversion is also achieved by the catalyst with the lowest Pd wt% 1.0, Pd/Au-ZeO-$CeO_2$ (10MAG). In fact the results for the different catalysts dependant of deposition rate, with the exception Pd/Au-ZeO-$CeO_2$ (10MAG) are almost superimposable on each other. T80% are all below 360 °C across the range a 58 °C difference is reported T50% 62 °C difference and T10% 49 °C.

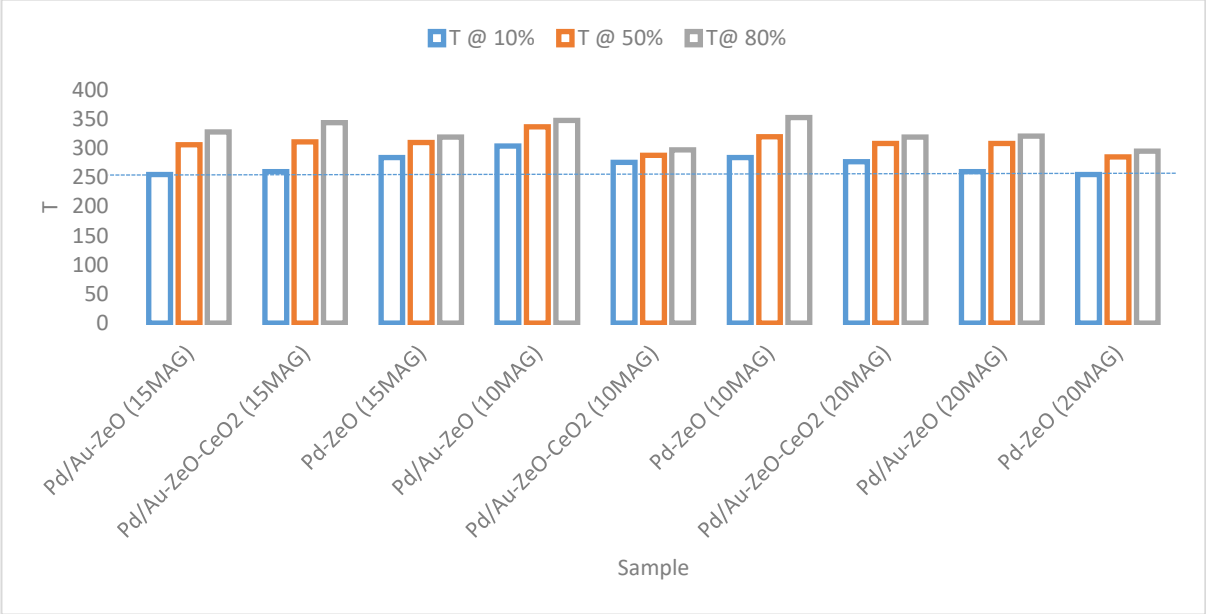


Figure 78 Temperature at which 10, 50 and 80% conversion is achieved for 10, 15 and 20 minute deposition rates

The activation energy plot below shows that the $E_a$ for the reaction of $CH_4$ with oxygen is well within the range that has been well recorded in literature. [191]

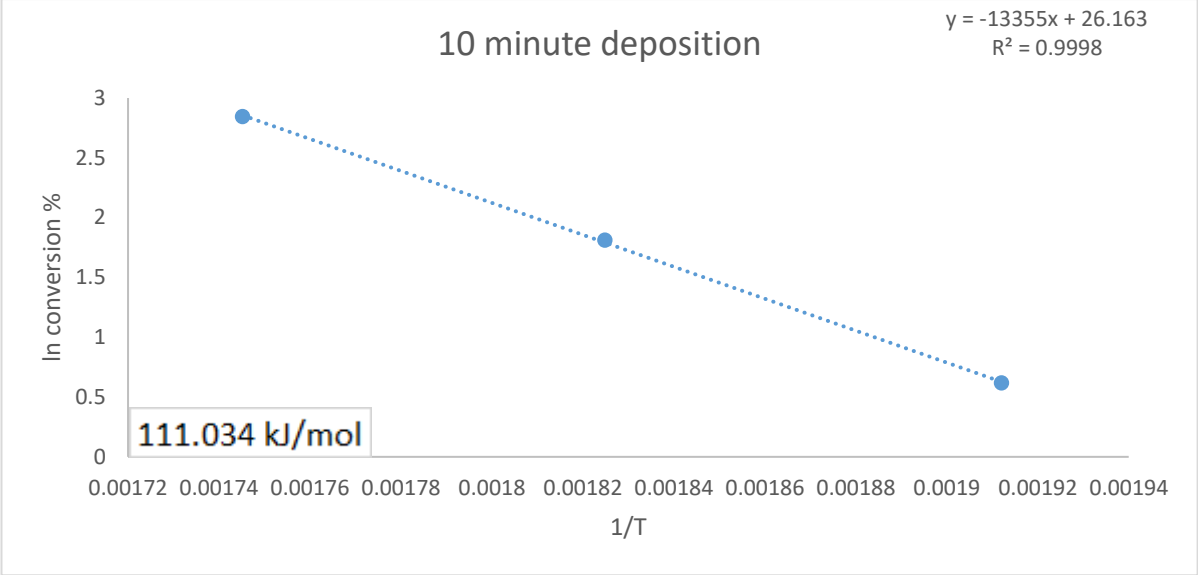


Figure 79 Activation Energy for HY-ZeO -Pd magnetron sputtered catalyst, 10 minute deposition rate

The following light off curves represent the $Al_2O_3$ prepared materials for the complete combustion of $CH_4$. As with the zeolite and $TiO_2$ samples 100% conversion is reached by 550 °C which is supported by research by L S Escandon et al.[192] Pd-$Al_2O_3$ is the standard catalytic material for the oxidation of automotive vehicular gases. By using a PVD method for coating the potential for impurities and reduced activity is removed. The time and expense of drying materials is removed and the cost of expensive metal salts and the time in person-hours to synthesise in the traditional method is reduced. The three catalysts that showed the best activity were Pd/Au-$Al_2O_3$ (15MAG), Pd/Au-$Al_2O_3$ (20MAG) and Pd/Au-$Al_2O_3$-$CeO_2$ (10MAG). All $Al_2O_3$ supports had surface areas in the range of 130 – 145 $m^2\ g^{-1}$.[193] The addition of $CeO_2$ as before demonstrates excellent OSC and redox cyclic properties to enhance the reduced Pd loading that is observed for all samples that were deposited for 10 minutes.[194] The 20 minute deposition catalysts which had Pd wt% loadings > 1.48 all reached > 98% conversion by 400 °C. There is evidence to suggest that gold and $Al_2O_3$ play a role in the complete combustion of $CH_4$, as the least active were not impregnated with gold and the most active were.[195,196]

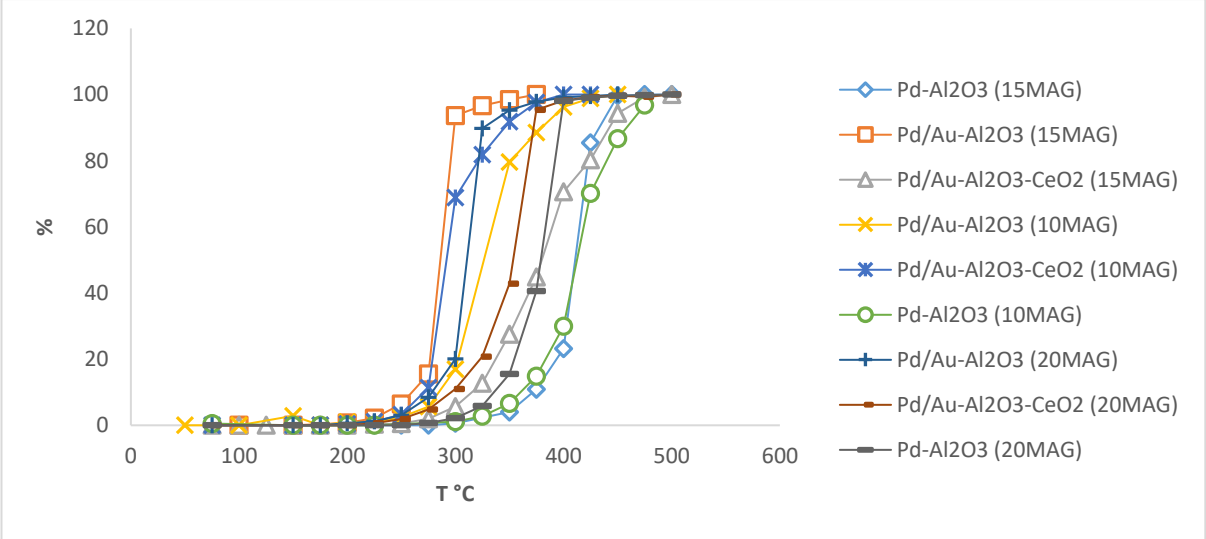


Figure 80 $Al_2O_3$- Pd magnetron sputtered catalyst light off curves for the combustion of $CH_4$ 10, 15 and 20 deposition rates

Figure 81 shows the T10, 50 and 80% conversion temperatures for the $Al_2O_3$ based catalysts. The $Al_2O_3$ based supports have the greatest range in comparison to the zeolite and $TiO_2$ materials. The greater difference in T10 – T80% is not due to surface area or Pd wt%, therefore might be due to interactions, or lack there-of between the reactive gases and the support. For the three different deposition rates, there is an observable pattern with the Pd-$Al_2O_3$ substrates, as they have the highest T10 and T50% conversion temperatures and with the exception of Pd/Au-$Al_2O_3$-$CeO_2$ (15MAG) the highest T80%. There is a difference of 100 °C in the T10% across the samples 126 °C across the T50% and 144 °C in the T80% materials, such a large range is not observed previously. L. S Escandon et al reported complete conversion of $CH_4$ to $CO_2$ > 400 °C.[197] Not only have several of these catalysts surpassed this, they have done so using a method of coating that has to date not been used for the purpose of catalytic vehicular exhaust gas abatement.

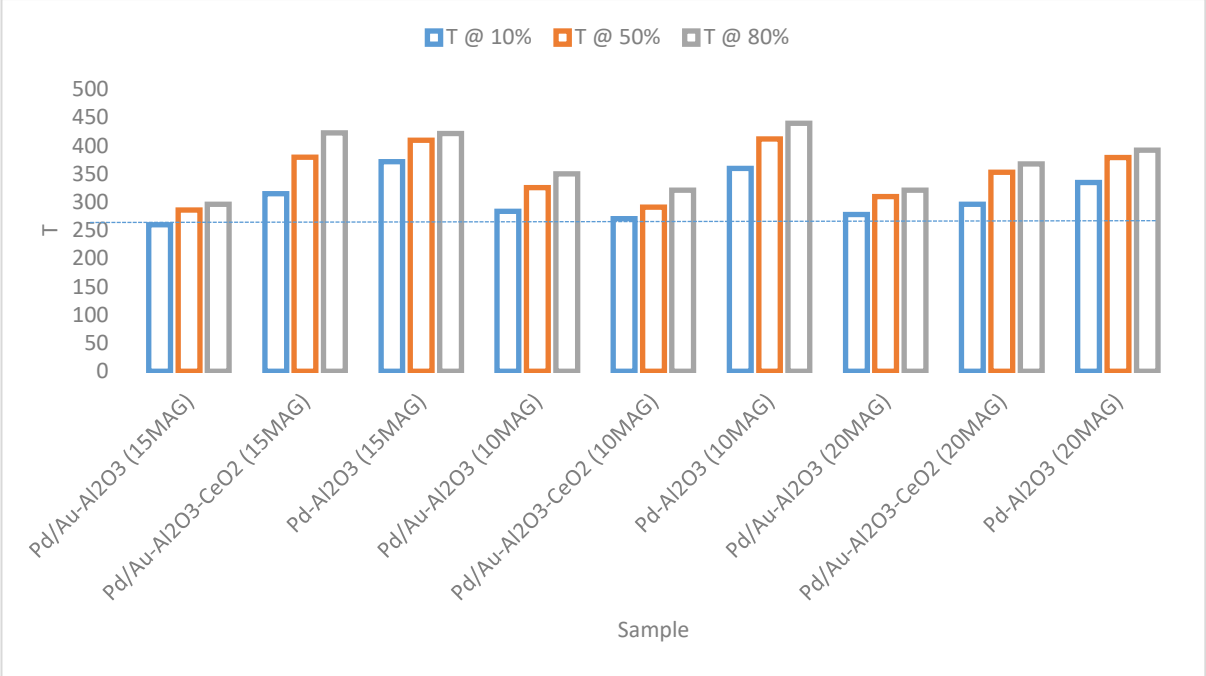


Figure 81 Temperature at which 10, 50 and 80% conversion is achieved for 10, 15 and 20 minute deposition rates

The activation energy plot below shows that the $E_a$ for the reaction of $CH_4$ with oxygen is well within the range that has been well recorded in literature. [198]

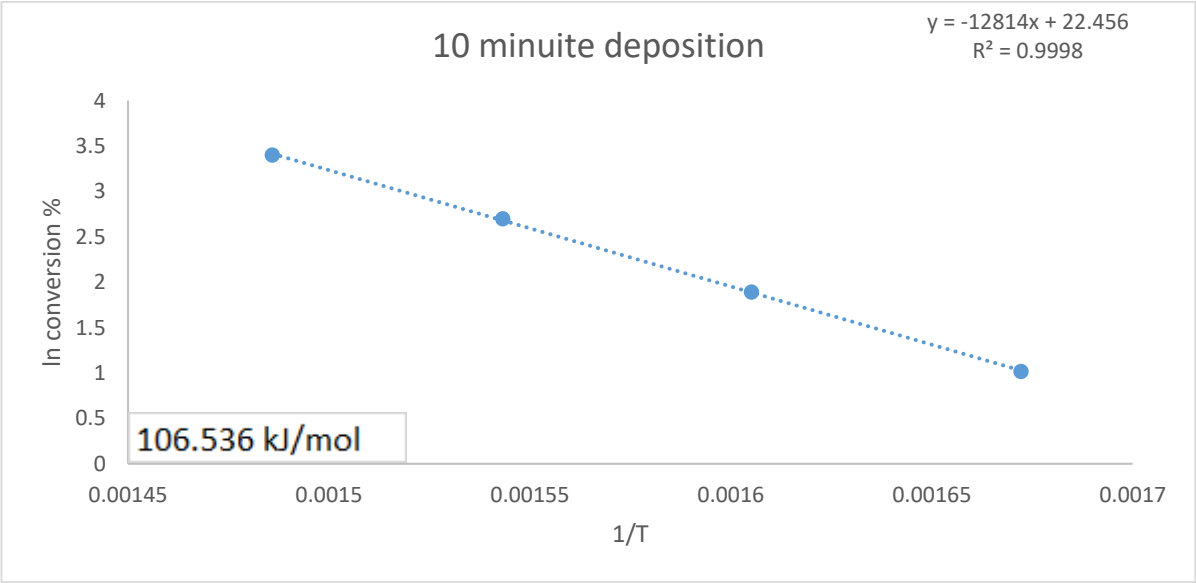


Figure 82 Activation Energy for $Al_2O_3$ -Pd magnetron sputtered catalyst, 10 minute deposition rate

### 7.4.6 PVD Conclusions

A series of catalytic materials were prepared using the PVD process of magnetron sputtering and then tested for the complete oxidation of CO and $CH_4$. Although thin film magnetron sputtering is well documented, using powders and for the purpose of vehicle exhaust

catalysis has not previously been studied. Activation energies for the PVD samples were similar to catalysts prepared *via* traditional methodologies such as; wet impregnation (WI) or ion exchange (IE). For the reaction of CO the $TiO_2$ group of materials performed the best and an increase in metal loading with a direct correlation to activity was observed, with wt% decreasing in the order of $TiO_2$ > zeolite > $Al_2O_3$. The promotive effects of $CeO_2$ are clearly seen, especially when the materials that were under the target for the least amount of time, therefore having the lowest Pd wt%. The two catalysts with the lowest recorded overall conversion of $CH_4$ to $CO_2$ were samples which were under the sputtering target for 15 minutes. Pd-ZeO (15MAG) and Pd/Au-$Al_2O_3$ (15MAG) both achieved 100% conversion at 375 °C. TEM confirmed well dispersed nanoparticles over the substrates. Thus, coupled with a unique way of creating catalytic materials that are free from impurities often associated with using wet chemical processes and do not require additional energy for drying a new synthesis approach to vehicular catalytic converters has potentially been discovered.

## 7.5 Geothermal Fluid prepared Zeolite

### 7.5.1 SEM

SEM data of the two silica sourced prepared samples indicates crystalline FAU-type typical octahedral morphology material as seen in Figure 83. No other crystalline materials impurities, phases or the presence of amorphous materials was observed. The particle size of the samples were agglomerated sub-micron sized.

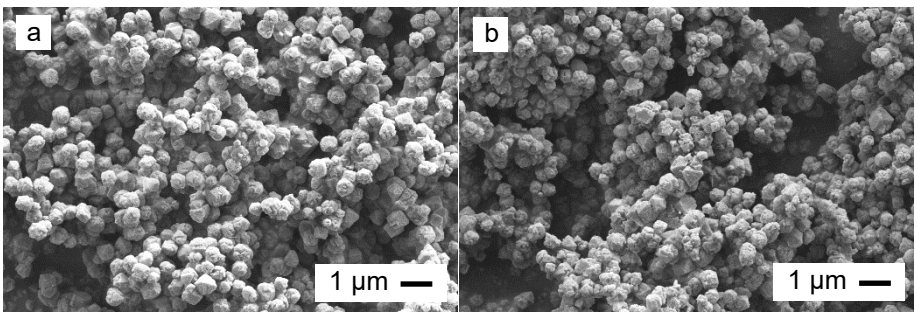


Figure 83 SEM images of FAU-type zeolites prepared with (a) Geo-12 and (b) Ludox.[199]

### 7.5.2 XRD Geothermal

Figure 84 shows confirmation of the FAU-type structure using XRD analysis. The diffractogram patterns are typical of FAU-type structures for both the Na-FAU (Ludox) and Na-FAU (Geo-12). The synthesis of the Ludox based zeolite is an established preparation for zeolites in their pure form; hence the similarity, in both diffraction pattern and peak intensities to the material prepared using Geo-12. A reduction is observed in FAU-type XRD intensities after the removal of $Na^+$ and the addition of Pd, which us supported by the reflections indicated in Figure 84. The results do however confirm that the Pd catalysts hold their typical FAU-type structure. The XRF analysis in Table 11 shows that the Si/Al ratios of the Ludox $Na^+$ forms were 1.94 and 1.96 for Geo-12 and after the addition of Pd this only changed the ratios by a small amount. As expected there was a $Na^+$ content reduction after the addition of Pd to both the as-made zeolites, especially after $NH_4Cl$ exchange; from 13.5 wt% to 4.40 wt% for Geo-12, and from 12.6 wt% to 4.06 wt% for Ludox. The catalysts can be represented as having a low Si/Al ratio. The textural features of the samples provided in Table 11 showed that the surface areas reduced marginally as a result of $NH_4Cl$ treatment (surface areas of H-FAU (Ludox) and H-FAU (Geo-12) were 587 and 561 $m^2\ g^{-1}$, respectively, surface area, only, determined for these two samples) and Pd introduction to Na-FAU samples. The reduction in micropore volume for the two Na-FAU-Pd samples and the reduction of intensity in the XRD peaks (not shown) may indicate amorphisation of the FAU-type material. The surface areas and micropore volumes of the Pd-loaded zeolites obtained from H-FAU samples were considerably lower, possibly due to the introduction of defects during the $NH_4Cl$ treatment and subsequent calcination. Thus rendering the zeolite structure susceptible to degradation during the Pd loading. The pore volumes of the samples synthesised using Ludox were higher, this could be due to their smaller particle sizes.[200]

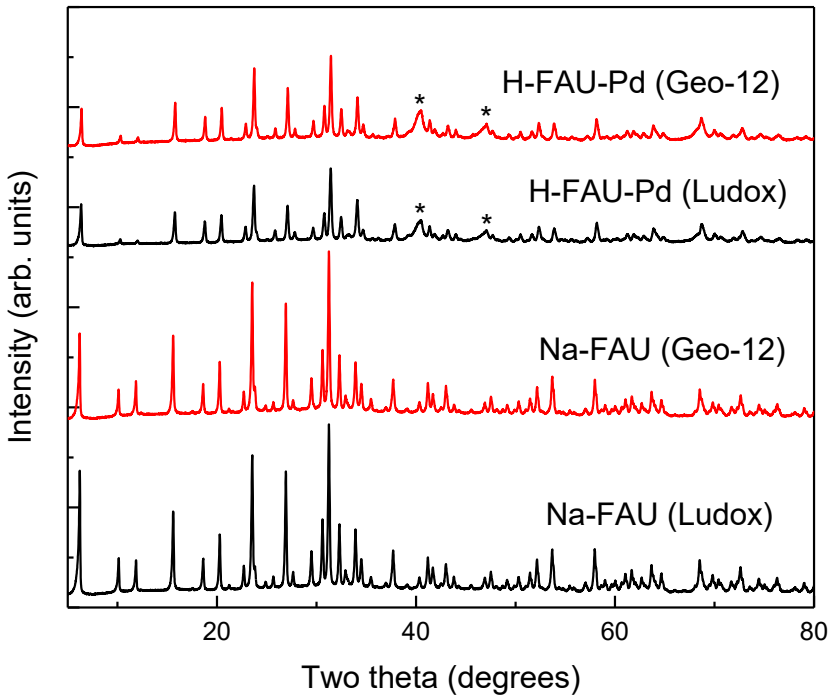


Figure 84: XRD patterns of FAU zeolites prepared with Ludox and Geo-12: as-made (Na-FAU) and after Pd impregnation of H-FAU samples (Pd-H-FAU): Pd peaks are indicated with an *.[201]

### 7.5.3 XRF and BET Data

**Table 11: Si/Al ratio, Na and Pd wt % as determined by XRF, and textural characteristics determined from nitrogen adsorption measurements at -196 °C: BET surface areas ($S_{BET}$), micropore volumes ($V_{\mu}$) and total pore volumes ($_{total}$).** [202]

| Sample | Si/Al | Na (wt%) | Pd (wt%) | $S_{BET}$ ($m^2\ g^{-1}$) | $V_{\mu}$ ($cm^3\ g^{-1}$) | $V_{total}$ ($cm^3\ g^{-1}$) |
|---|---|---|---|---|---|---|
| **Na-FAU (Geo-12)** | 1.96 | 13.5 | - | 529 | 0.23 | 0.61 |
| **Na-FAU (Ludox)** | 1.94 | 12.6 | - | 672 | 0.30 | 0.85 |
| **Na-FAU-Pd (Geo-12)** | 2.13 | 8.24 | 5.65 | 556 | 0.24 | 0.56 |
| **Na-FAU-Pd (Ludox)** | 2.05 | 7.75 | 6.21 | 612 | 0.24 | 0.84 |
| **H-FAU-Pd (Geo-12)** | 1.92 | 4.40 | 2.30 | 321 | 0.09 | 0.32 |
| **H-FAU-Pd (Ludox)** | 2.01 | 4.06 | 5.25 | 312 | 0.11 | 0.39 |
| **Na-FAU-Pd-MAG (Geo-12)** | 2.13 | 8.24 | 2.48 | 139 | - | - |
| **Na-FAU-Pd-MAG (Ludox)** | 2.05 | 7.75 | 1.31 | 660 | - | - |

Nitrogen adsorption desorption isotherms of the Na-FAU-Pd and Na-FAU-Pd-MAG zeolites are shown in figure 85. The isotherms are of Type I classification, which is confirmed with the XRD results. The retention of the shape of the isotherms, despite the substantial reduction in the micropore volumes for the latter samples, suggests the formation of a low surface area dense amorphous material in H-FAU-Pd samples. A hysteresis loop in all isotherms, however the isotherms do not plateau at high relative pressures which is typically observed with Type IV classification. Therefore the characteristics of the isotherms have been labelled Type IIb by Rouquerol *et al*. [203,204]

The shape of the hysteresis loop deviates from H1 in Na-FAU-Pd, this is typical of agglomerates of spheroidal particles of constant size, to H3 in H-FAU-Pd, which could mean the presence of amassed powders in the latter. [205, 206]

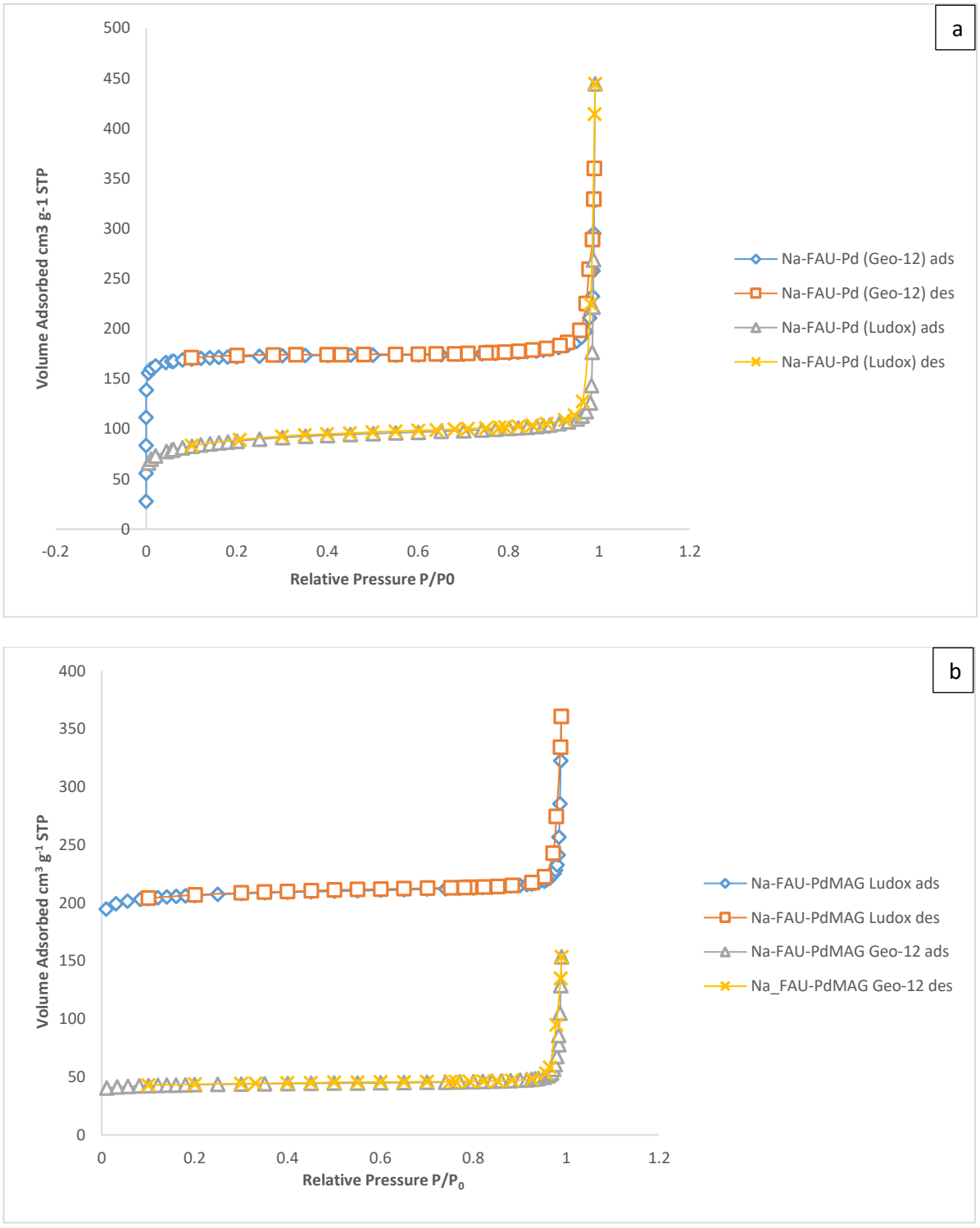


Figure 85 Nitrogen adsorption desorption isotherms of (a) Na-FAU-Pd and (b) Na-FAU-Pd-MAG zeolites prepared with Ludox and Geo-12. The isotherms of Na-FAU-Pd (Ludox) have been shifted by 100 along the y-axis for clarity.

### 7.5.4 Catalyst testing

The full oxidation of $CH_4$ and CO was used to determine the catalytic activity of the geothermal and available zeolites prepared for platinum group metals (PGM) catalyst supports and their use in dual-fuel engine exhaust emission abatement. All the Pd containing catalytic materials demonstrated activity, the results are interpreted as light-off curves in Figure 86 and 88 and as T10, 50, and 80% charts in figures 87 and 89. Generally, the $Na^+$ structures of the catalysts were more active than their $H^+$ cousins, the highest activity for full $CH_4$ oxidation was recorded by Na-FAU-Pd (Geo 12), which gave T10% and T50% values 226 °C and 237 °C, respectively. The closeness in results for Na-FAU-Pd (Geo 12) over Na-FAU-Pd (Ludox) (241 °C and 261 °C) endorses that the geothermal colloidal silica has similar assets to those of a regular reagent (Ludox) in the formulation of the zeolite. The H-FAU-Pd (Geo 12) and H-FAU-Pd (Ludox) catalysts had roughly similar activities for the combustion of $CH_4$ and CO, where T10% and T50% varied by no more than 5 °C from each other for $CH_4$ conversion.[207] For CO conversion the difference was slightly bigger, but by no more than 21 °C for the combustion of CO respectively. Importantly the PGM catalysts prepared using PVD method were the most active for the complete combustion of CO. This can be clearly observed in the T10% for Na-FAU-PdMAG (Geo-12) catalyst which has a value of 89 °C, which is 73 °C lower than the equivalent catalyst prepared in the traditional WI method.

Interestingly along with the higher activities of the $Na^+$ catalysts, there is also a more rapid ascent to light-off for these catalysts, as seen by the incline of the conversion slope with the increase in temperature. This can be quantified by inspecting the difference between T10 and T50% temperatures; the greater the increase in rate of conversion, the lesser the difference in temperature. The $Na^+$ catalytic materials had maximum T50-T10 values of 20 °C, versus 40 °C for the $H^+$ forms, and the lowest value overall, 11 °C, was recorded for the preparation using the geothermal source for $CH_4$. There is an important difference in the shape of the light-off curves: while the $Na^+$ catalysts approach 100% conversion almost immediately after light-off, the conversion reaches 67% for H-FAU-Pd (Geo 12) and 79% for H-FAU-Pd (Ludox) at 300 °C, after which

there is a relatively gradual conversion increase towards 100% for the $CH_4$ reaction. This is not observed in the CO reaction, as all catalysts, even those without Pd show a steep ascent after light-off. The reduction of activity for the catalysts in $H^+$ state are not only attributed to the absence of $Na^+$. Studies have revealed that any elevation in catalyst functionality due to $Na^+$ is significantly less than that observed here.[208,209]Thus, it is most probably the addition of Pd and the secondary calcination stage to form $H^+$ that is attributed to the fractional reduction in catalyst crystallinity and porosity which displays as a decline in catalytic activity (although these catalysts still retain partial activity). Thermodynamic data, calculated below 30% conversion, indicated activation energies in the range 55.4-90.3 kJ $mol^{-1}$. These comparable are similar to studies for $CH_4$ oxidation in a recent study of Pd-MOR catalysts, where the activation energies were calculated to be 75-84 kJ $mol^{-1}$.[210] Notably the catalyst with the lowest activation energy for $CH_4$ conversion to carbon dioxide is Na-FAU-PdMAG (Geo-12), yet this catalyst does not reach 100% conversion up to 550 °C. In fact the magnetron sputtered geothermal prepared zeolite is the worst performing of the Pd coated materials for the $CH_4$ conversion reaction. In contrast, however, the same catalyst is the best at full conversion of CO to $CO_2$ and has the lowest activation energy of 52.5 kJ $mol^{-1}$, thus giving more weight to the two reaction pathways differing, as previously mentioned.

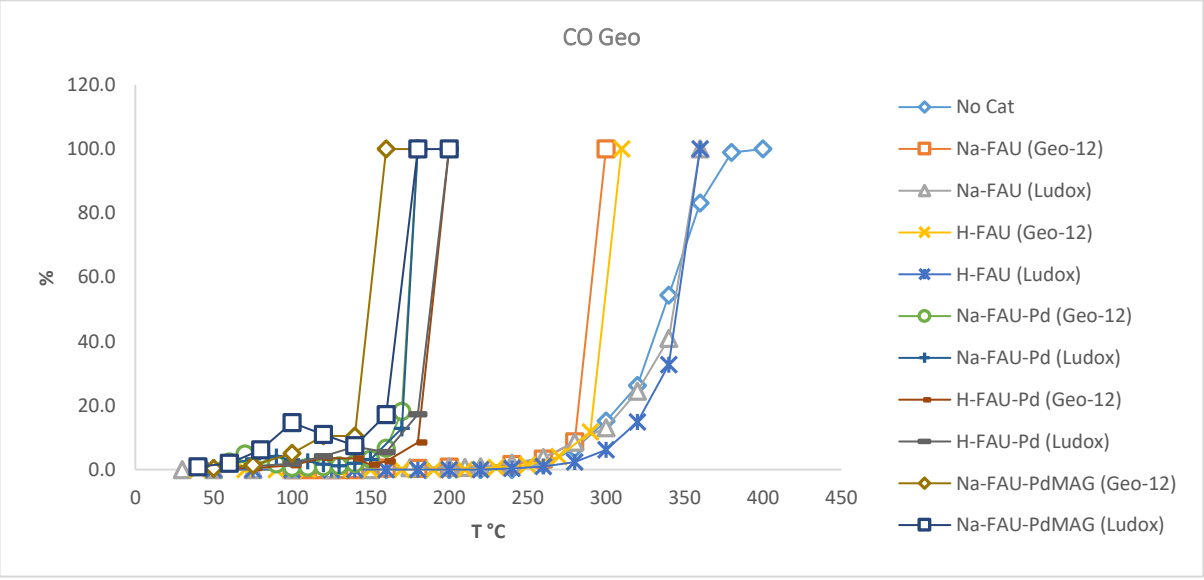


Figure 86 Light-off curves for the complete oxidation of CO with H-FAU Na-FAU and H-FAU-Pd (WI) Na-FAU-Pd (WI) and Na-FAU-Pd-MAG samples.

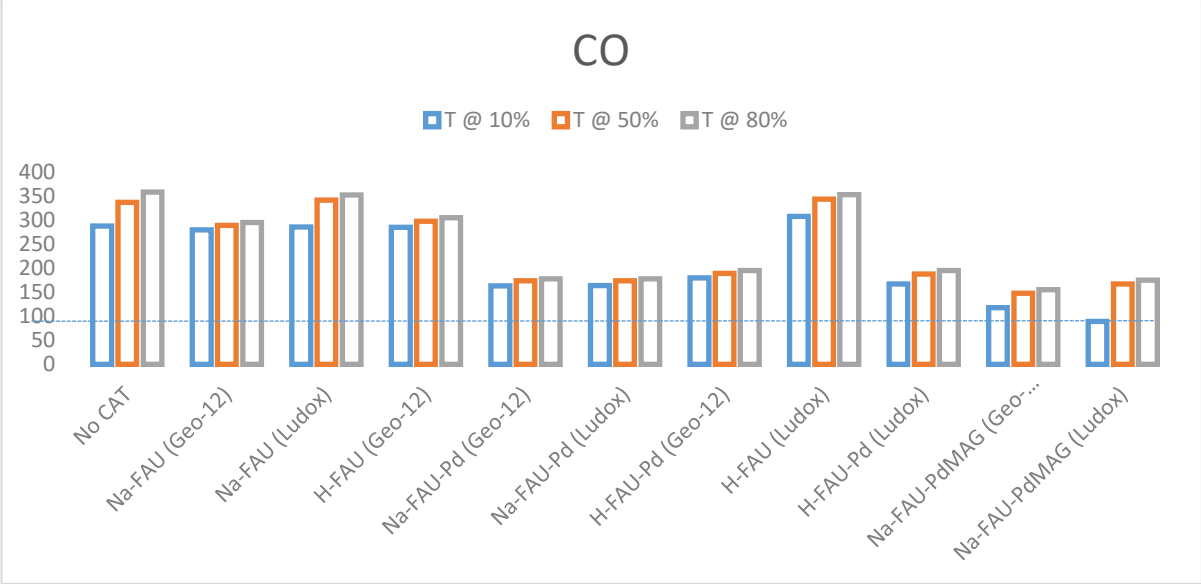


Figure 87 Temperature at which 10, 50 and 80% conversion

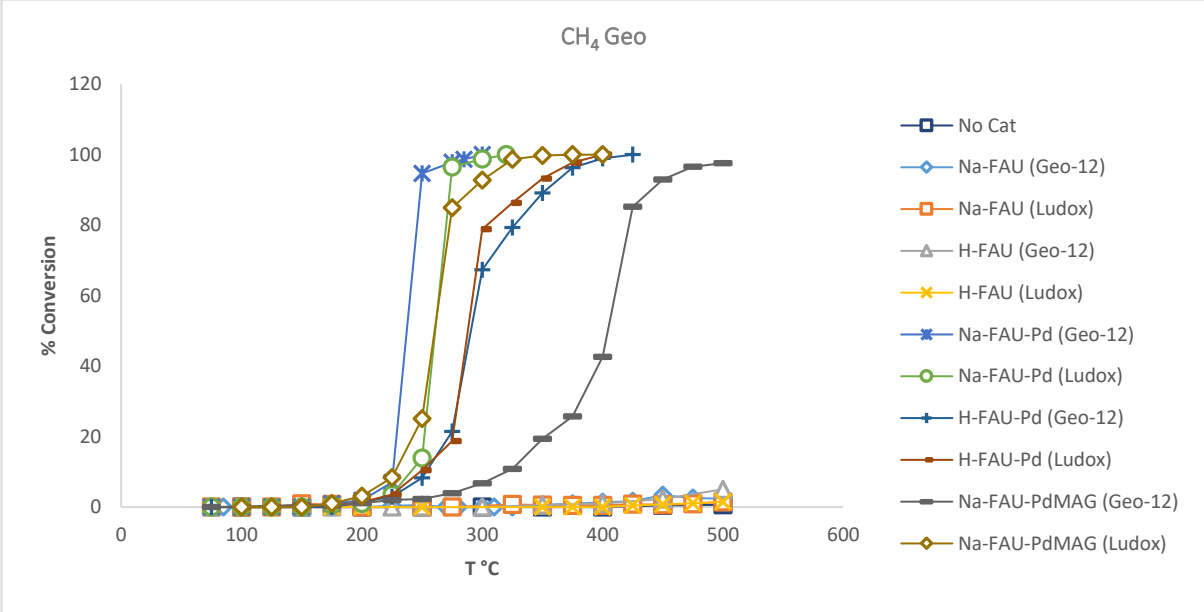


Figure 88 $CH_4$ conversion vs reaction temperature over fixed bed reactor.

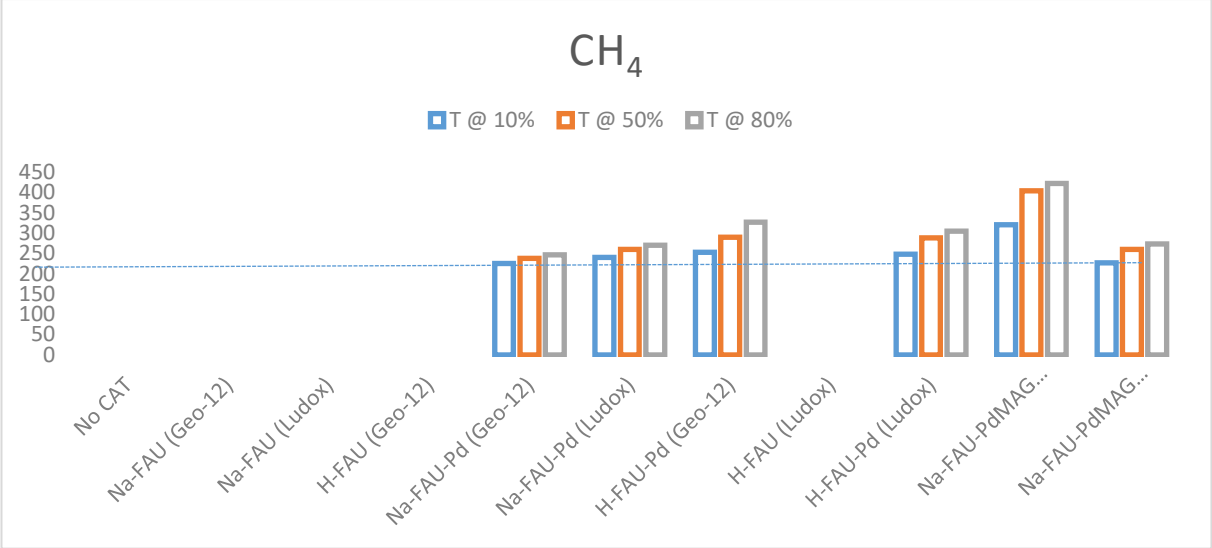


Figure 89 shows T10, 50 and 80% temperatures for the traditional silica and geothermal source silica prepared zeolites and subsequent coating with Pd via WI and PVD.

**Table 12: T10, T50% and thermodynamic data for $CH_4$ oxidation.**

| | T10% (°C) | T50% (°C) | T50-T10% (°C) | $E_a$ (kJ $mol^{-1}$) |
|---|---|---|---|---|
| **Na-FAU-Pd (Geo 12)** | 226 | 237 | 11 | 71.1 |
| **Na-FAU-Pd (Ludox)** | 241 | 261 | 20 | 82.6 |
| **H-FAU-Pd (Geo 12)** | 253 | 290 | 37 | 90.3 |
| **H-FAU-Pd (Ludox)** | 248 | 288 | 40 | 76.5 |
| **Na-FAU-PdMAG (Geo-12)** | 320 | 404 | 84 | 55.4 |
| **Na-FAU-PdMAG (Ludox)** | 227 | 260 | 33 | 86.2 |

### 7.5.5 Conclusions

Silica sol isolated from geothermal fluid extract was applied as a source of silica for the synthesis of low Si/Al zeolite Y. The comparison in the characteristics of the sample to one formulated with a conventional silica sol, Ludox, confirmed that this natural source of silica, can be effectively employed for the synthesis of zeolites with high purity. The zeolite Y synthesised from the two silica sources was subsequently loaded with Pd, both as-made Na-samples and after partial conversion to H-zeolites, the Na forms being coated *via* PVD and WI. Na-FAU-Pd samples showed slight decreases in surface areas and micropore volumes as a result of the Pd loading. The Na-FAU-PdMAG (Geo-12) especially, as this sample had a huge loss in surface area, this could be due to single atoms coating the substrate and filling the pores, thus reducing the accessible surface area. A significant reduction was observed for H-FAU-Pd samples, this was accredited to the extra synthesis steps involved in the synthesis of said samples. All the zeolites coated with Pd were catalytically active for the full oxidative decomposition of $CH_4$ and CO. The highest activities of which were reported for catalytic materials containing Na. In summary, the results show that a natural silica source, with almost unbounded supply, can be used as a reagent to prepare zeolite catalysts that are efficient in decreasing dual-fuel engine exhaust emissions. This report is principally interesting as it utilizes a readily available natural resource that can contribute to the decarbonisation of heavy goods transportation and a coating method that has not previously been used for this purpose.

## 7.6 Pd, Pt and Rh WI Catalysts

### 7.6.1 Table showing wt% for catalytic materials and surface areas

**Table 13 wt% and surface area results for a series of $TiO_2$ catalysts coated the Pd, Pt and Rh**

| Sample Name | Pd wt % | Pt wt% | Rh wt% | Ti wt% | Al wt% | Si wt% | Ce wt% | Zr wt% | Surface area $m^2\ g^{-1}$ |
|---|---|---|---|---|---|---|---|---|---|
| **TiO2** | 1.2 | 1.9 | 1.7 | 60.0 | x | x | x | x | 103.4 |
| **$Al_2O_3$** | 1.5 | 0.7 | 0.15 | x | 60.0 | x | x | x | 140.0 |
| **Hy-Zeo** | 1.4 | 2.4 | 1.2 | x | 3.3 | 46.5 | x | x | 103.0 |
| **$TiO_2$/Hy-ZeO** | 1.3 | 1.7 | 1.3 | 32.5 | 24.9 | 21.8 | x | x | 316.5 |
| **$TiO_2/Al_2O_3$** | 0.4 | 0.5 | 0.5 | 25.8 | 27.3 | x | x | x | 120.6 |
| **$TiO_2/ZrO_2$** | 1.0 | 0.6 | 0.4 | 25.0 | x | x | x | 19.0 | 116.4 |

| | | | | | | | | | |
|---|---|---|---|---|---|---|---|---|---|
| **$TiO_2/ZrO_2/CeO_2$** | 1.2 | 0.6 | 0.8 | 21.0 | x | x | 1.0 | 20.0 | 68.0 |
| **$TiO_2/Al_2O_3/CeO_2$** | 0.9 | 0.8 | 1 | 27.6 | 25.3 | x | 1.3 | x | 117.1 |
| **$TiO_2$/HY-ZeO/$CeO_2$** | 1.0 | 1.6 | 1.3 | 27.4 | 2.0 | 21.3 | 2.2 | x | 378.7 |

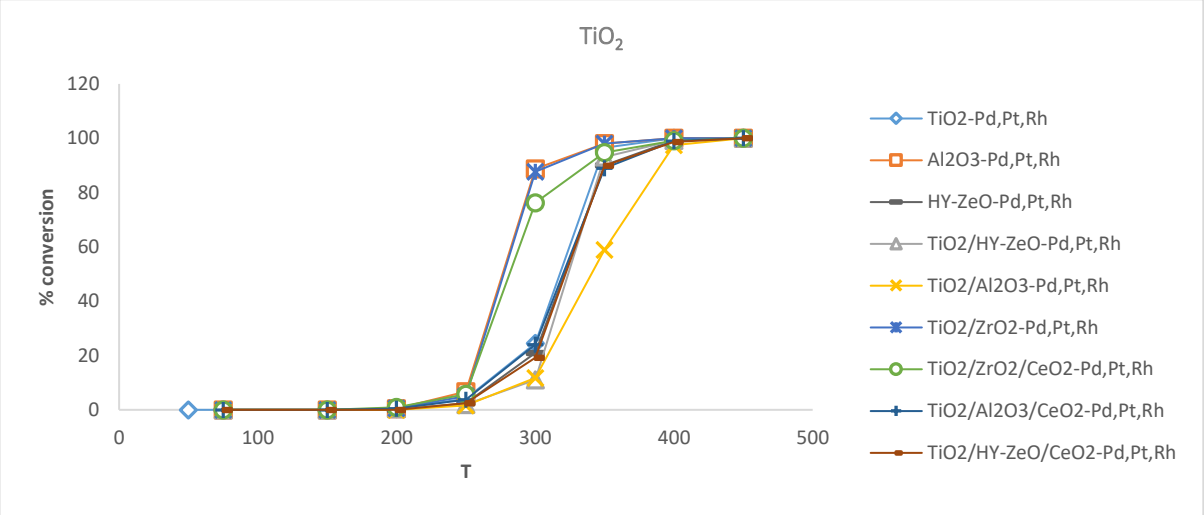


Figure 90 Light off curves for $TiO_2$ based catalysts loaded with Pd, Pt and Rh for the complete combustion of $CH_4$

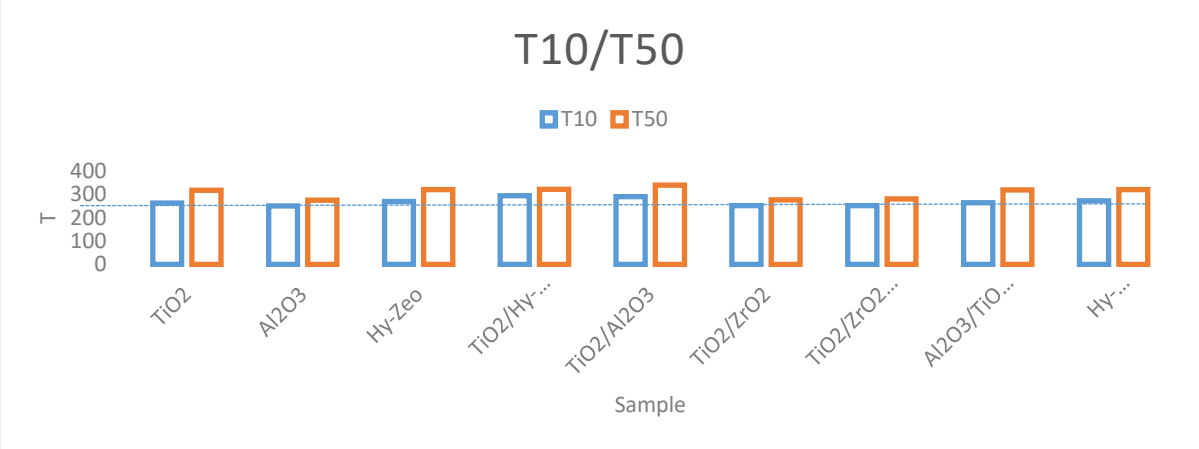


Figure 91 T10% and T50% temperatures for the $TiO_2$ based Pd, Pt and Rh coated catalysts

Figure 90 shows a series of light-off curves for the complete oxidation of $CH_4$ with a series of $TiO_2$ based catalytic materials. $TiO_2$ was coupled with stability enhancing $Al_2O_3$ and surface area increasing zeolite Y and promotive redox cyclic $CeO_2$ and zirconia in order to determine which combination would give the lowest temperature for full conversion to $CO_2$. All materials, including the single supports zeolite Y and $Al_2O_3$, which were added for contrast reached full conversion below 550 °C and several less than or at 400 °C. This supports findings here [211] for the use of $TiO_2$

as a supportive material with PGM loading. PGM loadings range from 0.4 – 2.4 wt% (table 13) across the group and were all prepared in the same way, as mentioned in the experimental section. Rh was incorporated into the catalysts with a view to reduce nitrogenous oxides in real world application.[212] All materials had T10% within 44 °C of each other and T50% within 64 °C figure 91. As observed previously, light-off curves started to ascend rapidly as the approached 300 °C, with the exception of $TiO_2/Al_2O_3$-Pd,Pt,Rh catalyst, notably this catalyst also had the lowest wt% for all the PGM coated onto it. Not much separates the full conversion temperatures for the series as all the materials are within 3% of 100% conversion by the time the furnace was reading 400 °C.

# 8. Conclusion

Substrate materials HAp, zeolite, $Al_2O_3$, $TiO_2$ and promoters such as zirconia and $CeO_2$ were coated with precious and PGM's in a number of different ways to determine their effectiveness as dual-fuel vehicular catalytic materials. Utilising known methods and improving on them using laboratory instruments, such as an ultra-sonic bath improved dispersion of materials across the range of supportive substrates. CO complete oxidation was achieved at room temperature with a number of different catalysts and $CH_4$ full combustion was achieved below 300 °C with conventional WI methods and the use of the PVD technique magnetron sputtering. Zeolites prepared from a natural geothermal source for the first time by Doyle et al and then coated *via* the two mentioned processes. The results obtained were promising for both the oxidative reactions, particularly for $CH_4$ conversion where > 95% was achieved at extremely low temperatures and without the need for complex core shell chemistry. $TiO_2$ proved to be an important addition for magnetron sputtering materials due to its conductive properties allowing high wt% depositions at relatively quick run times. The combination of Au and Pd demonstrated higher activity towards the production of $CO_2$ for both reactive gases. The materials coated with Pd, Pt and Rh all showed a reduction in activity compared to the low temperature conversion materials and the magnetron and geothermal catalysts, however, rhodium is a necessary addition

if the reduction of nitrogenous oxides is to be achieved. TEM analysis confirmed the exceptional distribution of precious metals over the supports used and showed nanoparticles as small as 2 nm. BET nitrogen adsorption data demonstrated a wide range of surface areas across the different supports, zeolites coming out on top with surface areas in excess of 500 $m^2 g^{-1}$, occasionally lower due to the loading effect of the precious metals. The addition of $CeO_2$ for materials with a lower wt% of precious metal played an important role in maintaining low overall temperature conversion. Several highly successful catalytic materials have been synthesised and tested on a purpose built catalyst testing rig and show great promise for reducing the harmful potent greenhouse gases CO and $CH_4$.

## 9. Future Work

The potential to further study PVD techniques for the production of vehicle catalytic materials is extensive. The different ratios of supports contained within is one project of interest as is the movement of powders whilst under vacuum. It would be interesting to test different target materials, including an alloy of Pd, Pt and Rh.

### References


[1] Bryant, L. (1976). The Development of the Diesel Engine. *Technology and Culture, 17*(3), 432-446. doi:10.2307/3103523

[2] Nuvolari, A., Verspagen, B. & von Tunzelmann, N. The early diffusion of the steam engine in Britain, 1700–1800: a reappraisal. *Cliometrica* **5,** 291–321 (2011). https://doi.org/10.1007/s11698-011-0063-6

[3] Transportation Engineering, ISSN: 2666-691X, Vol: 1, Page: 100005, Publication Year2020

[4] Heywood, J.B., 1988. "Internal Combustion Engine Fundamentals", McGraw-Hill, New York

[5] J. F. Moon, Rudolph Diesel and the Diesel Engine, Priory Press, Wisconsin 1974

[6] L. Wei and P. Geng, *Fuel Processing Technology*, 2016, **142**, 264-278.

[7] L. Wei and P. Geng, *Fuel Processing Technology*, 2016, **142**, 264-278.

[8] C. A. Power, *Dual fuel systems*, http://www.cleanairpower.com/howitworks.html.

[9] M. E. J. Stettler, W. J. B. Midgley, J. J. Swanson, D. Cebon and A. M. Boies, *Environmental Science and Technology*, 2016, **50**, 2018-2026.

[10] A. Simchi, E. Tamjid, F. Pishbin and A. R. Boccaccini, *Nanomedicine: Nanotechnology, Biology, and Medicine*, 2011, **7**, 22-39.

[11] IPCC (2007) IPCC fourth assessment report: Climate change 2007, intergovernmental panel on climate change, Cambridge University Press, Cambridge

[12] Kirk R. Smith, Manish A. Desai, Jamesine V. Rogers, and Richard A. Houghton PNAS July 30, 2013 110 (31) E2865-E2874; https://doi.org/10.1073/pnas.1308004110

[13] P. Howard, *The G-volution Optimiser Dual-Fuel Technology*, https://www.g-volution.co.uk/site/g-volution-optimiser, 2017.
[14] P. Howard, *The G-volution Optimiser Dual-Fuel Technology*, https://www.g-volution.co.uk/site/g-volution-optimiser, 2017.
[15] P. Howard, *The G-volution Optimiser Dual-Fuel Technology*, https://www.g-volution.co.uk/site/g-volution-optimiser, 2017.
[16] P. Howard, *The G-volution Optimiser Dual-Fuel Technology*, https://www.g-volution.co.uk/site/g-volution-optimiser, 2017.
[17] P. Howard, *The G-volution Optimiser Dual-Fuel Technology*, https://www.g-volution.co.uk/site/g-volution-optimiser, 2017.
[18] P. Howard, *The G-volution Optimiser Dual-Fuel Technology*, https://www.g-volution.co.uk/site/g-volution-optimiser, 2017.
[19] P. Howard, *The G-volution Optimiser Dual-Fuel Technology*, https://www.g-volution.co.uk/site/g-volution-optimiser, 2017.
[20] U. Government, *National Institute of Standards and Technology*.
[21] OPEC, *OPEC share of world crude reserves*, https://www.opec.org/opec_web/en/data_graphs/330.htm.
[22] OPEC, *OPEC share of world crude reserves*, https://www.opec.org/opec_web/en/data_graphs/330.htm.
[23] OPEC, *OPEC share of world crude reserves*, https://www.opec.org/opec_web/en/data_graphs/330.htm.
[24] BP, *Statistical Review, Natural gas*, https://www.bp.com/en/global/corporate/energy-economics/statistical-review-of-world-energy/natural-gas.html.
[25] S. Faramawy, T. Zaki and A. A. E. Sakr, *Journal of Natural Gas Science and Engineering*, 2016, **34**, 34-54.
[26] J. G. Speight, in *Natural Gas*, ed. J. G. Speight, Gulf Publishing Company, Editon edn., 2007, pp. 161-192.
[27] C. M. Robert, in *Developments in Marine Geology*, ed. C. M. Robert, Elsevier, Editon edn., 2008, vol. 3, pp. 415-450.
[28] P. B. P. T. P. D. H. Welte, *Petroleum Formation and Occurrence*, 2 edn., Springer, Berlin, Heidelberg, 1984.
[29] P. B. P. T. P. D. H. Welte, *Petroleum Formation and Occurrence*, 2 edn., Springer, Berlin, Heidelberg, 1984.
[30] T. Gold, *Annual review of energy. Vol. 10*, 1985, 53-77.
[31] J. G. Speight, in *Natural Gas*, ed. J. G. Speight, Gulf Publishing Company, Editon edn., 2007, pp. 161-192.
[32] K. Zengler, H. H. Richnow, R. Rosselló-Mora, W. Michaelis and F. Widdel, *Nature*, 1999, **401**, 266-269.
[33] L. Brennan and P. Owende, *Renewable and Sustainable Energy Reviews*, 2010, **14**, 557-577.
[34] B. Sherwood Lollar, T. D. Westgate, J. A. Ward, G. F. Slater and G. Lacrampe-Couloume, *Nature*, 2002, 416, 522-524.
[35] X. Wang and M. Economides, in *Advanced Natural Gas Engineering*, eds. X. Wang and M. Economides, Gulf Publishing Company, Editon edn., 2009, pp. 35-58.
[36] X. Wang and M. Economides, in *Advanced Natural Gas Engineering*, eds. X. Wang and M. Economides, Gulf Publishing Company, Editon edn., 2009, pp. 1-34.
[37] X. Wang and M. Economides, in *Advanced Natural Gas Engineering*, eds. X. Wang and M. Economides, Gulf Publishing Company, Editon edn., 2009, pp. 59-113.
[38] X. Wang and M. Economides, in *Advanced Natural Gas Engineering*, eds. X. Wang and M. Economides, Gulf Publishing Company, Editon edn., 2009, pp. 115-169.
[39] X. Wang and M. Economides, in *Advanced Natural Gas Engineering*, eds. X. Wang and M. Economides, Gulf Publishing Company, Editon edn., 2009, pp. 59-113.
[40] X. Wang and M. Economides, in *Advanced Natural Gas Engineering*, eds. X. Wang and M. Economides, Gulf Publishing Company, Editon edn., 2009, pp. 115-169.
[41] S. K. Malyan, A. Bhatia, A. Kumar, D. K. Gupta, R. Singh, S. S. Kumar, R. Tomer, O. Kumar and N. Jain, *Science of The Total Environment*, 2016, **572**, 874-896.
[42] BP, *BP Statistical Review of World Energy*.
[43] Q. Wang, X. Chen, A. N. Jha and H. Rogers, *Renewable and Sustainable Energy Reviews*, 2014, **30**, 1-28.
[44] T. Kwan and M. Jordan, *Chemical Physics Letters*, 2018, **708**, 216-221.
[45] H. Song, X. Meng, Z.-j. Wang, H. Liu and J. Ye, *Joule*, 2019, **3**, 1606-1636.
[46] R. S. Mulliken, *The Journal of Chemical Physics*, 1933, **1**, 492-503.
[47] Czech P. T. (2006) Molecular Orbital Theory. Encyclopedia of Inorganic Chemistry (eds R.B. King, R.H. Crabtree, C.M. Lukehart, D.A. Atwood and R.A. Scott). Doi:10.1002/0470862106.ia144

[48] Rose JJ, Wang L, Xu Q, et al. Carbon Monoxide Poisoning: Pathogenesis, Management, and Future Directions of Therapy [published correction appears in Am J Respir Crit Care Med. 2017 Aug 1;196 (3):398-399]. *Am J Respir Crit Care Med*. 2017;195(5):596-606. doi:10.1164/rccm.201606-1275CI

[49] Kao L.W, Nanagas K.A: Carbon Monoxide Poisoning. Med Clin North Am. 2005 Nov;89(6):1161-94. Doi:10.1016/j.mcna.2005.06.007 [PubMed:16227059]

[50] M. E. J. Stettler, W. J. B. Midgley, J. J. Swanson, D. Cebon and A. M. Boies, *Environmental Science and Technology*, 2016, **50**, 2018-2026.

[51] J. D. Wang, J. K. Liu, Y. Lu, D. J. Hong and X. H. Yang, *Materials Research Bulletin*, 2014, **55**, 190-195.

[52] E. J. Peterson, A. T. DeLaRiva, S. Lin, R. S. Johnson, H. Guo, J. T. Miller, J. H. Kwak, C. H. F. Peden, B. Kiefer, L. F. Allard, F. H. Ribeiro and A. K. Datye, *Nature Communications*, 2014, **5**.

[53] I. c. o. c. transportation, *Vehicle Standards*.

[54] Mizutani, T., Kaneda, A., Ichikawa, S., Miyairi, Y. et al., "Filtration Behavior of Diesel Particulate Filters (2)," SAE Technical Paper 2007-01-0923, 2007, https://doi.org/10.4271/2007-01-0923.

[55] p. org, *5,000 'Dieselgate' deaths in Europe per year:study*, file:///E:/SEM%20request%20sheet/2017-09-dieselgate-deaths-europe-year.pdf, Accessed 18/09/17, 2017.

[56] K. C. Taylor, in *Studies in Surface Science and Catalysis*, eds. A. Crucq and A. Frennet, Elsevier, Editon edn., 1987, vol. 30, pp. 97-116.

[57] P. L. Silveston, *Catalysis Today*, 1995, **25**, 175-195.

[58] M. McCarthy in*The Independent*, Independent Print Limited, London, Editon edn, 2010, vol. 02JUL10, p. 1

[59] C. Taylor, Automobile Catalytic Converters, Editor(s): A. Crucq, A. Frennet, Studies in Surface Science and Catalysis, Elsevier, Volume 30, 1987, Pages 97-116.

[60] E. J. Peterson, A. T. DeLaRiva, S. Lin, R. S. Johnson, H. Guo, J. T. Miller, J. H. Kwak, C. H. F. Peden, B. Kiefer, L. F. Allard, F. H. Ribeiro and A. K. Datye, *Nature Communications*, 2014, **5**.

[61] A. f. e. c. b. catalyst, *Emission control technology*.

[62] A. f. e. c. b. catalyst, *Emission control technology*.

[63] A. f. e. c. b. catalyst, *Emission control technology*.

[64] Flanigen, Edith. (1980). Molecular Sieve Zeolite Technology: The First Twenty-Five Years. Pure and Applied Chemistry - PURE APPL CHEM. 52. 2191-2211. 10.1351/pac198052092191.

[65] Flanigen, Edith. (1980). Molecular Sieve Zeolite Technology: The First Twenty-Five Years. Pure and Applied Chemistry - PURE APPL CHEM. 52. 2191-2211. 10.1351/pac198052092191.

[66] Flanigen, Edith. (1980). Molecular Sieve Zeolite Technology: The First Twenty-Five Years. Pure and Applied Chemistry - PURE APPL CHEM. 52. 2191-2211. 10.1351/pac198052092191.

[67] A. Corma, F. Rey, S. Valencia, J. L. Jordá and J. Rius, *Nature Materials*, 2003, **2**, 493-497.

[68] X. Xu, Y. Bao, C. Song, W. Yang, J. Liu and L. Lin, *Microporous and Mesoporous Materials*, 2004, **75**, 173-181.

[69] X. Xu, Y. Bao, C. Song, W. Yang, J. Liu and L. Lin, *Microporous and Mesoporous Materials*, 2004, **75**, 173-181.

[70] JOUR Lutz, Wolfgang Shutilov, Roman A. Pore Structure of USY Zeolites in Dependence on Steaming Condition Zeitschrift für anorganische und allgemeine Chemie Z. anorg. allg. Chem.vl.640,3-4, https://doi.org/10.1002/zaac.201300403

[71] A. H. Janssen, A. J. Koster and K. P. de Jong, *Angewandte Chemie International Edition*, 2001, **40**, 1102-1104.

[72] Journal Article,Adams, John Allan Stewart, Richardson, K. A. Thorium, uranium and zirconium concentrations in bauxite.Economic Geology.Economic Geology,1960, DO 10.2113/gsecongeo.55.8.1653

[73] Journal Article,Adams, John Allan Stewart, Richardson, K. A. Thorium, uranium and zirconium concentrations in bauxite.Economic Geology.Economic Geology,1960, DO 10.2113/gsecongeo.55.8.1653

[74] Journal Article,Adams, John Allan Stewart, Richardson, K. A. Thorium, uranium and zirconium concentrations in bauxite.Economic Geology.Economic Geology,1960, DO 10.2113/gsecongeo.55.8.1653

[75] X. Krokidis, P. Raybaud, A.-E. Gobichon, B. Rebours, P. Euzen and H. Toulhoat, *The Journal of Physical Chemistry B*, 2001, **105**, 5121-5130.

[76] Alumina trihydrate market value forecast to reach US$500 billion by 2023, Additives for Polymers, Volume 2018, Issue 7, 2018, Page 11,

[77] S. F. o. ResearchGate, *Corrosion and Corrosion Protection Studies of Carbon Steel alloy in Seawater using; Zirconia, Silicon Carbide and Alumina Nanoparticles*

[78] Chi Him A. Tsang,Kai Li,Yuxuan Zeng,Wei Zhao,Tao Zhang,Yujie Zhan,Ruijie Xie,Dennis Y.C. Leung,Haibao Huang, (titanium oxide based photocatalytic)Environment International,Elsevier, April 2019

[79] Chi Him A. Tsang,Kai Li,Yuxuan Zeng,Wei Zhao,Tao Zhang,Yujie Zhan,Ruijie Xie,Dennis Y.C. Leung,Haibao Huang, (titanium oxide based photocatalytic)Environment International,Elsevier, April 2019

[80] Akira Fujishima,Tata N. Rao,Donald A. Tryk, Titanium dioxide photocatalysis, Journal of Photochemistry and Photobiology C: Photochemistry Reviews, Elsevier, 29 June 2000

[81] A. Mazare, M. Dilea, D. Ionita, I. Titorencu, V. Trusca and E. Vasile, *Bioelectrochemistry*, 2012, **87**, 124-131.

[82] A. Costescu, I. Pasuk, F. Ungureanu, A. Dinischiotu, M. Costache, F. Huneau, S. Galaup, P. le Coustumer and D. Predoi, *Digest Journal of Nanomaterials and Biostructures*, 2010, **5**, 989-1000.

[83] A. L. Giraldo-Betancur, D. G. Espinosa-Arbelaez, A. d. Real-López, B. M. Millan-Malo, E. M. Rivera-Muñoz, E. Gutierrez-Cortez, P. Pineda-Gomez, S. Jimenez-Sandoval and M. E. Rodriguez-García, *Current Applied Physics*, 2013, **13**, 1383-1390.

[84] A. L. Giraldo-Betancur, D. G. Espinosa-Arbelaez, A. d. Real-López, B. M. Millan-Malo, E. M. Rivera-Muñoz, E. Gutierrez-Cortez, P. Pineda-Gomez, S. Jimenez-Sandoval and M. E. Rodriguez-García, *Current Applied Physics*, 2013, **13**, 1383-1390.

[85] P. Ducheyne, S. Radin and L. King, *Journal of Biomedical Materials Research*, 1993, **27**, 25-34.

[86] S. V. Dorozhkin, *Biomaterials*, 2010, **31**, 1465-1485.

[87] K. Zhao, B. Qiao, J. Wang, Y. Zhang and T. Zhang, *Chemical Communications*, 2011, **47**, 1779-1781.

[88] H. Tounsi, S. Djemal, C. Petitto and G. Delahay, *Applied Catalysis B: Environmental*, 2011, **107**, 158-163.

[89] S. Sugiyama, E. Nitta, K. Abe, H. Hayashi and J. B. Moffat, *Catalysis Letters*, 1998, **55**, 189-196.

[90] B. Rêgo De Vasconcelos, L. Zhao, P. Sharrock, A. Nzihou and D. Pham Minh, *Applied Surface Science*, 2016, **390**, 141-156.

[91] R. Marques, L. Mazri, S. Da Costa, F. Delacroix, G. Djéga-Mariadassou and P. Da Costa, *Catalysis Today*, 2008, **137**, 179-184.

[92] Q. Liu, J. P. Matinlinna, Z. Chen, C. Ning, G. Ni, H. Pan and B. W. Darvell, *Ceramics International*, 2015, **41**, 6149-6157.

[93] E. M. Rivera-Munoz, R. Huirache-Acuna, R. Velázquez, G. Alonso-Núnez and S. Eguía-Eguía, *Journal of Nanoscience and Nanotechnology*, 2011, **11**, 5592-5598.

[94] E. M. Rivera-Muñoz, R. Velázquez and J. L. Cabrera-Torres, in *Materials Science Forum*, Editon edn., 2010, vol. 638-642, pp. 681-686.

[95] S. Sugiyama, T. Minami, T. Higaki, H. Hayashi and J. B. Moffat, *Industrial and Engineering Chemistry Research*, 1997, **36**, 328-334.

[96] S. Sugiyama, T. Minami, T. Moriga, H. Hayashi and J. B. Moffat, *Journal of Solid State Chemistry*, 1998, **135**, 86-95.

[97] S. F. o. ResearchGate, *Removal of volatile organic compounds using pulsed dielectric barrier discharge plasma combined to catalysts* https://www.researchgate.net/figure/Principe-schematique-des-processus-de-recombinaison-de-type-Eley-Rideal-et_fig9_281047060 [accessed 23 Sep, 2019].

[98] Atkins, *Elements of physical chemistry*, 5 edn., Oxford Press, London, 2009.

[99] J. M. T. W. J. Thomas, *Principles and Practice of Heterogeneous catalysis*, VCH, New York/Germany, 1996.

[100] G. Bräuer, B. Szyszka, M. Vergöhl and R. Bandorf, *Vacuum*, 2010, **84**, 1354-1359.

[101] P. J. Kelly and R. D. Arnell, *Vacuum*, 2000, **56**, 159-172.

[102] R. J. Hill, R. Cormia and P. McLeod, 1977, **2**, 1583-1586.

[103] W. D. Sproul, P. J. Rudnik, M. E. Graham and S. L. Rohde, *Surface and Coatings Technology*, 1990, **43-44**, 270-278.

[104] P. J. Kelly and R. D. Arnell, *Vacuum*, 2000, **56**, 159-172.

[105] D. R. Gibson, I. Brinkley, G. W. Hall, E. M. Waddell and J. M. Walls, Proceedings of SPIE - The International Society for Optical Engineering, 2006.

[106] P. J. Kelly and R. D. Arnell, *Vacuum*, 2000, **56**, 159-172.

[107] P. J. Kelly and R. D. Arnell, *Vacuum*, 2000, **56**, 159-172.

[108] Ameh, E.S. A review of basic crystallography and x-ray diffraction applications. *Int J Adv Manuf Technol* **105,** 3289–3302 (2019). https://doi.org/10.1007/s00170-019-04508-1

[109] Ameh, E.S. A review of basic crystallography and x-ray diffraction applications. *Int J Adv Manuf Technol* **105,** 3289–3302 (2019). https://doi.org/10.1007/s00170-019-04508-1

[110] Humphreys, Colin. (2013). The significance of Bragg's law in electron diffraction and microscopy, and Bragg's second law. Acta crystallographica. Section A, Foundations of crystallography. 69. 45-50. 10.1107/S0108767312047587.

[111] D. Dollimore, P. Spooner, A. Turner, The bet method of analysis of gas adsorption data and its relevance to the calculation of surface areas, Surface Technology, Volume 4, Issue 2, 1976, Pages 121-160,

[112] Bag, Surajit. (2015). A Short Review on Structural Equation Modeling: Applications and Future Research Directions. Journal of Supply Chain Management Systems. 4. 64-69. 10.21863/jscms/2015.4.3.014.

[113] Rukari, Tushar & Babita, Alhat. (2013). Review Article TRANSMISSION ELECTRON MICROSCOPY-AN OVERVIEW. 1. 1-7.

[114] Toledo Torres, Mario & Bubnovich, Valeri & SAVELIEV, ALEXEI & Kennedy, Lawrence. (2006). Comparative study of lean and rich filtration combustion of methane/air, ethane/air, and propane/air mixtures. Int. Conf. Heat Transfer, Thermal Engineering, and Environment, WSEAS.

[115] J. Kamieniak, A. M. Doyle, P. J. Kelly and C. E. Banks, *Ceramics International*, 2016.

[116] Z. Boukha, J. L. Ayastuy, J. R. González-Velasco and M. A. Gutiérrez-Ortiz, *Applied Catalysis B: Environmental*, 2017, **201**, 189-201.

[117] A.-C. Lee, R.-H. Lin, C.-Y. Yang, M.-H. Lin and W.-Y. Wang, *Materials Chemistry and Physics*, 2008, **109**, 275-280.

[118] A. Costescu, I. Pasuk, F. Ungureanu, A. Dinischiotu, M. Costache, F. Huneau, S. Galaup, P. le Coustumer and D. Predoi, *Digest Journal of Nanomaterials and Biostructures*, 2010, **5**, 989-1000.

[119] S. Joschek, B. Nies, R. Krotz and A. Göpferich, *Biomaterials*, 2000, **21**, 1645-1658.

[120] M. Cargnello, J. J. Delgado Jaén, J. C. Hernández Garrido, K. Bakhmutsky, T. Montini, J. J. Calvino Gamez, R. J. Gorte and P. Fornasiero, Nanoscale Science and Engineering Forum 2013 - Core Programming Area at the 2013 AIChE Annual Meeting: Global Challenges for Engineering a Sustainable Future, 2014.

[121] P. Gélin and M. Primet, *Applied Catalysis B: Environmental*, 2002, **39**, 1-37.

[122] S. Colussi, A. Trovarelli, C. Cristiani, L. Lietti and G. Groppi, *Catalysis Today*, 2012, **180**, 124-130.

[123] A. M. Doyle, R. Postolache, D. Shaw, R. Rothon and L. Tosheva, *Microporous and Mesoporous Materials*, 2019, **285**, 56-60.

[124] A. W. Petrov, D. Ferri, F. Krumeich, M. Nachtegaal, J. A. van Bokhoven and O. Kröcher, *Nature Communications*, 2018, **9**, 2545.

[125] A. W. Petrov, D. Ferri, F. Krumeich, M. Nachtegaal, J. A. van Bokhoven and O. Kröcher, *Nature Communications*, 2018, **9**, 2545.

[126] R. Gholami, M. Alyani and K. J. Smith, *Catalysts*, 2015, **5**, 561-594.

[127] G. C. Bond, *Gold Bulletin*, 1972, **5**, 11-13.

[128] P. A. Sermon, G. C. Bond and P. B. Wells, *Journal of the Chemical Society, Faraday Transactions 1: Physical Chemistry in Condensed Phases*, 1979, **75**, 385-394.

[129] M. Haruta, N. Yamada, T. Kobayashi and S. Iijima, *Journal of Catalysis*, 1989, **115**, 301-309.

[130] M. Haruta, *Catalysis Today*, 1997, **36**, 153-166.

[131] H. C. Yao and Y. F. Y. Yao, *Journal of Catalysis*, 1984, **86**, 254-265.

[132] P. Li, X. Chen, Y. Li and J. W. Schwank, *Catalysis Today*, 2019, **327**, 90-115.

[133] P. Li, X. Chen, Y. Li and J. W. Schwank, *Catalysis Today*, 2019, **327**, 90-115.

[134] G. Spezzati, A. D. Benavidez, A. T. DeLaRiva, Y. Su, J. P. Hofmann, S. Asahina, E. J. Olivier, J. H. Neethling, J. T. Miller, A. K. Datye and E. J. M. Hensen, *Applied Catalysis B: Environmental*, 2019, **243**, 36-46.

[135] M. Haruta, *Catalysis Today*, 1997, **36**, 153-166.

[136] *Studies in Surface Science and Catalysis*, eds. J. A. Moulijn, P. W. N. M. van Leeuwen and R. A. van Santen, Elsevier, Editon edn., 1993, vol. 79, pp. 309-333.

[137] H. Li, Q. Zhu, Y. Li, M. Gong, Y. Chen, J. Wang and Y. Chen, *Journal of Rare Earths*, 2010, **28**, 79-83.

[138] R. Bacani, T. S. Martins, M. C. A. Fantini and D. G. Lamas, *Journal of Alloys and Compounds*, 2016, **671**, 396-402.

[139] M. Li, S. Zhang, L. Lv, M. Wang, W. Zhang and B. Pan, *Chemical Engineering Journal*, 2013, **229**, 118-125.

[140] M. Haruta, *Catalysis Today*, 1997, **36**, 153-166.

[141] M. Monai, T. Montini, R. J. Gorte and P. Fornasiero, *European Journal of Inorganic Chemistry*, 2018, **2018**, 2884-2893.

[142] M. Cargnello, J. J. D. Jaén, J. C. H. Garrido, K. Bakhmutsky, T. Montini, J. J. C. Gámez, R. J. Gorte and P. Fornasiero, *Science*, 2012, **337**, 713-717.

[143] S. C. Su, J. N. Carstens and A. T. Bell, *Journal of Catalysis*, 1998, **176**, 125-135.

[144] S. C. Su, J. N. Carstens and A. T. Bell, *Journal of Catalysis*, 1998, **176**, 125-135.

[145] W. R. Schwartz and L. D. Pfefferle, *The Journal of Physical Chemistry C*, 2012, **116**, 8571-8578.

[146] H. Yoshida, R. Kakei, A. Fujiwara, Y. Uchida and M. Machida, *The Journal of Physical Chemistry C*, 2018, **122**, 28173-28181.

[147] J. A. Lupescu, J. W. Schwank, G. B. Fisher, J. Hangas, S. L. Peczonczyk and W. A. Paxton, *Applied Catalysis B: Environmental*, 2018, **223**, 76-90.

[148] M. Lyubovsky and L. Pfefferle, *Applied Catalysis A: General*, 1998, **173**, 107-119.

[149] N. M. Kinnunen, J. T. Hirvi, K. Kallinen, T. Maunula, M. Keenan and M. Suvanto, *Applied Catalysis B: Environmental*, 2017, **207**, 114-119.

[150] J. M. T. W. J. Thomas, *Principles and Practice of Heterogeneous catalysis*, VCH, New York/Germany, 1996.

[151] *Handbook of Heterogeneous Catalysis*, Editon edn.

[152] C. Please, P. Hagan and D. Schwendeman, *Light-off Behavior of Catalytic Converters*, 1994.

[153] F. F. Tao, J.-j. Shan, L. Nguyen, Z. Wang, S. Zhang, L. Zhang, Z. Wu, W. Huang, S. Zeng and P. Hu, *Nature Communications*, 2015, **6**, 7798.

[154] Electronic Supplementary Material (ESI) for Catalysis Science & Technology. This journal is © The Royal Society of Chemistry 2018

[155] S. Marinel, D. H. Choi, R. Heuguet, D. Agrawal and M. Lanagan, *Broadband Dielectric Characterization of TiO2 Ceramics Sintered Through Microwave and Conventional Processes*, 2013.

[156] S. Marinel, D. H. Choi, R. Heuguet, D. Agrawal and M. Lanagan, *Broadband Dielectric Characterization of TiO2 Ceramics Sintered Through Microwave and Conventional Processes*, 2013.

[157] S. Chao and F. Dogan, *International Journal of Applied Ceramic Technology*, 2011, **8**, 1363-1373.

[158] in *Electromagnetics Explained*, ed. R. Schmitt, Newnes, Burlington, Editon edn., 2002, pp. 25-49.

[159] H. Zhu, Z. Qin, W. Shan, W. Shen and J. Wang, *Catalysis Today*, 2007, **126**, 382-386.

[160] H. Zhu, Z. Qin, W. Shan, W. Shen and J. Wang, *Journal of Catalysis*, 2005, **233**, 41-50.

[161] C. Serre, F. Garin, G. Belot and G. Maire, *Journal of Catalysis*, 1993, **141**, 9-20.

[162] G. S. Zafiris and R. J. Gorte, *Journal of Catalysis*, 1993, **139**, 561-567.

[163] S. H. Oh and C. C. Eickel, *Journal of Catalysis*, 1988, **112**, 543-555.

[164] T. Bunluesin, H. Cordatos and R. J. Gorte, *Journal of Catalysis*, 1995, **157**, 222-226.

[165] E. M. Slavinskaya, R. V. Gulyaev, A. V. Zadesenets, O. A. Stonkus, V. I. Zaikovskii, Y. V. Shubin, S. V. Korenev and A. I. Boronin, *Applied Catalysis B: Environmental*, 2015, **166-167**, 91-103.

[166] P. Begum and R. C. Deka, *ChemistrySelect*, 2017, **2**, 8847-8855.

[167] Z. Duan and G. Henkelman, *ACS Catalysis*, 2014, **4**, 3435-3443.

[168] H. Zhu, Z. Qin, W. Shan, W. Shen and J. Wang, *Journal of Catalysis*, 2005, **233**, 41-50.

[169] J. M. T. W. J. Thomas, *Principles and Practice of Heterogeneous catalysis*, VCH, New York/Germany, 1996.

[170] E. M. Slavinskaya, R. V. Gulyaev, A. V. Zadesenets, O. A. Stonkus, V. I. Zaikovskii, Y. V. Shubin, S. V. Korenev and A. I. Boronin, *Applied Catalysis B: Environmental*, 2015, **166-167**, 91-103.

[171] K. Zorn, S. Giorgio, E. Halwax, C. R. Henry, H. Grönbeck and G. Rupprechter, *The Journal of Physical Chemistry C*, 2011, **115**, 1103-1111.

[172] M. Haruta, *Catalysis Today*, 1997, **36**, 153-166.

[173] E. M. Slavinskaya, R. V. Gulyaev, A. V. Zadesenets, O. A. Stonkus, V. I. Zaikovskii, Y. V. Shubin, S. V. Korenev and A. I. Boronin, *Applied Catalysis B: Environmental*, 2015, **166-167**, 91-103.

[174] L. S. Escandón, S. Ordóñez, A. Vega and F. V. Díez, *Chemosphere*, 2005, **58**, 9-17.

[175] A. Yu. Stakheev, A. M. Batkin, N. S. Teleguina, G. Bragina, V. I. Zaikovsky, I. Prosvirin, A. K. Khudorozhkov and V. Bukhtiyarov, *Particle Size Effect on CH4 Oxidation Over Noble Metals: Comparison of Pt and Pd Catalysts*, 2013.

[176] D. Decarolis, I. Lezcano-Gonzalez, D. Gianolio and A. M. Beale, *Topics in Catalysis*, 2018, **61**, 162-174.

[177] H. C. Yao and Y. F. Y. Yao, *Journal of Catalysis*, 1984, **86**, 254-265.

[178] P. Li, X. Chen, Y. Li and J. W. Schwank, *Catalysis Today*, 2019, **327**, 90-115.

[179] H. Li, Q. Zhu, Y. Li, M. Gong, Y. Chen, J. Wang and Y. Chen, *Journal of Rare Earths*, 2010, **28**, 79-83.

[180] A. Yu. Stakheev, A. M. Batkin, N. S. Teleguina, G. Bragina, V. I. Zaikovsky, I. Prosvirin, A. K. Khudorozhkov and V. Bukhtiyarov, *Particle Size Effect on CH4 Oxidation Over Noble Metals: Comparison of Pt and Pd Catalysts*, 2013.

[181] D. Decarolis, I. Lezcano-Gonzalez, D. Gianolio and A. M. Beale, *Topics in Catalysis*, 2018, **61**, 162-174.

[182] A. W. Petrov, D. Ferri, F. Krumeich, M. Nachtegaal, J. A. van Bokhoven and O. Kröcher, *Nature Communications*, 2018, **9**, 2545.

[183] A. W. Petrov, D. Ferri, F. Krumeich, M. Nachtegaal, J. A. van Bokhoven and O. Kröcher, *Nature Communications*, 2018, **9**, 2545.

[184] A. W. Petrov, D. Ferri, F. Krumeich, M. Nachtegaal, J. A. van Bokhoven and O. Kröcher, *Nature Communications*, 2018, **9**, 2545.

[185] R. Gholami, M. Alyani and K. J. Smith, *Catalysts*, 2015, **5**, 561-594.

[186] P. Gelin and M. Primet, *Complete Oxidation of Methane at Low Temperature Over Noble Metal Based Catalysts: A Review*, 2002.

[187] C. M. de Correa and H. Ai´da Luz Villa, *Applied Catalysis B: Environmental*, 1996, **10**, 313-323.

[188] H. Maeda, Y. Kinoshita, K. R. Reddy, K. Muto, S. Komai, N. Katada and M. Niwa, *Applied Catalysis A: General*, 1997, **163**, 59-69.

[189] K. Okumura, E. Shinohara and M. Niwa, *Catalysis Today*, 2006, **117**, 577-583.

[190] A. W. Petrov, D. Ferri, F. Krumeich, M. Nachtegaal, J. A. van Bokhoven and O. Kröcher, *Nature Communications*, 2018, **9**, 2545.

[191] A. W. Petrov, D. Ferri, F. Krumeich, M. Nachtegaal, J. A. van Bokhoven and O. Kröcher, *Nature Communications*, 2018, **9**, 2545.

[192] L. S. Escandón, S. Ordóñez, A. Vega and F. V. Díez, *Chemosphere*, 2005, **58**, 9-17.

[193] D. Roth, P. Gelin, E. Tena and M. Primet, *Topics in Catalysis*, 2001, **16**, 77-82.

[194] S. Colussi, A. Trovarelli, C. Cristiani, L. Lietti and G. Groppi, *Catalysis Today*, 2012, **180**, 124-130.

[195] D. J. Mowbray, A. Migani, G. Walther, D. M. Cardamone and A. Rubio, *The Journal of Physical Chemistry Letters*, 2013, **4**, 3006-3012.

[196] D. E. De Vos and B. F. Sels, *Angewandte Chemie International Edition*, 2005, **44**, 30-32.

[197] L. S. Escandón, S. Ordóñez, A. Vega and F. V. Díez, *Chemosphere*, 2005, **58**, 9-17.

[198] A. W. Petrov, D. Ferri, F. Krumeich, M. Nachtegaal, J. A. van Bokhoven and O. Kröcher, *Nature Communications*, 2018, **9**, 2545.

[199] A. M. Doyle, R. Postolache, D. Shaw, R. Rothon and L. Tosheva, *Microporous and Mesoporous Materials*, 2019, **285**, 56-60.

[200] A. M. Doyle, R. Postolache, D. Shaw, R. Rothon and L. Tosheva, *Microporous and Mesoporous Materials*, 2019, **285**, 56-60.

[201] A. M. Doyle, R. Postolache, D. Shaw, R. Rothon and L. Tosheva, *Microporous and Mesoporous Materials*, 2019, **285**, 56-60.

[202] A. M. Doyle, R. Postolache, D. Shaw, R. Rothon and L. Tosheva, *Microporous and Mesoporous Materials*, 2019, **285**, 56-60.

[203] A. M. Doyle, R. Postolache, D. Shaw, R. Rothon and L. Tosheva, *Microporous and Mesoporous Materials*, 2019, **285**, 56-60.

[204] J. R. F. Rouquerol, Kenneth Sing,, *Adsorption by Powders and Porous Solids. Principles, Methodology and Applications*, 1st edn., Academic Press, London, 1999.

[205] A. M. Doyle, R. Postolache, D. Shaw, R. Rothon and L. Tosheva, *Microporous and Mesoporous Materials*, 2019, **285**, 56-60.

[206] K. S. W. Sing, D. H. Everett, R. A. W. Haul, L. Moscou, R. A. Pierotti, J. Rouquérol and T. Siemieniewska, Editon edn.

[207] A. M. Doyle, R. Postolache, D. Shaw, R. Rothon and L. Tosheva, *Microporous and Mesoporous Materials*, 2019, **285**, 56-60.

[208] X. Auvray, A. Lindholm, M. Milh and L. Olsson, *Catalysis Today*, 2018, **299**, 212-218.

[209] Y. Xie, M. E. Galvez, A. Matynia and P. Da Costa, *Clean Technologies and Environmental Policy*, 2018, **20**, 715-725.

[210] A. W. Petrov, D. Ferri, F. Krumeich, M. Nachtegaal, J. A. van Bokhoven and O. Kröcher, *Nature Communications*, 2018, **9**, 2545.

[211] L. S. Escandón, S. Ordóñez, A. Vega and F. V. Díez, *Chemosphere*, 2005, **58**, 9-17.

[212] R. Burch, J. P. Breen and F. C. Meunier, *Applied Catalysis B: Environmental*, 2002, **39**, 283-303.